THE $0^+_1 \rightarrow 0^+_g$ MONOPOLE TRANSITION IN ^{112}Cd

BY

ERICH GOTTFRIED ROHWER

submitted to the Faculty of Science in partial fulfilment of the requirements for the degree of MSc in the Department of Physics the at University of Zululand.

Date Submitted : 1 December 1985

ABSTRACT

Internal conversion is a nuclear electromagnetic deexcitation process by which an electron is emitted from an atomic electron shell. This process competes with the emission of gamma-rays from the nucleus. Recently a mini-orange electron spectrometer, for the recording of internal electron spectra, was designed and built at the University of Zululand. The spectrometer has proven to be a very effective apparatus for the detection of internal conversion electrons.

The work presented in this dissertation essentially consists of three main parts. Firstly a theoretical study of electromagnetic deexcitation processes, with special emphasis on internal conversion, is presented. In this dissertation the main field of interest is internal conversion monopole transitions, for which gamma-radiation is strictly prohibited. The monopole matrix element is defined and its relevance to nuclear structure is emphasized. Secondly, a brief description of the mini-orange spectrometer used in this work is presented, together with a discussion on the transmission characteristics of the apparatus. The method used to determine the transmission curve for a specific configuration, is described in detail, and some experimental results of transmission curves are given. Thirdly, the details of the experimental arrangement and conditions for the recording of the ^{112}Cd internal conversion spectrum are given, as well as the obtained results. The $0^+_1 \rightarrow 0^+_g$ monopole transition in ^{112}Cd was detected. The recorded spectrum, was analyzed and the results were used to calculate the nuclear structure parameters $\rho(E0)$ and $X(E0/E2)$. The obtained results compare well

with similar results presented in the literature. The results were also compared to some theoretical predictions of these parameters, and it has become evident that none of these nuclear model predictions are in satisfactory agreement with the experimental values. This stresses the significance of experiments of this kind in gaining more information on the structure of the nucleus.

Interne omsettingselektrone is 'n elektromagnetiese verval-proses van die kern, waarby 'n elektron uit die elektronskil van die atoom uitgestraal word. Die proses kompeteer met die uitstraling van gamma-strale. Onlangs is 'n mini-orange elektronspektrometer, vir die waarneming van interne omsettingselektrone, by die Universiteit van Zoeloeland ontwerp en gebou. Dit het geblyk dat die spektrometer 'n effektiewe apparaat vir die waarneming van interne omsettingselektrone is.

Die werk wat in hierdie verhandeling voorgelê word kan in drie hoofdele ingedeel word. Eerstens word 'n teoretiese studie van elektromagnetiese verval, met spesifieke verwysings na omsettingselektrone, gegee. In die verhandeling word hoofsaaklik klem gelê op monopoolomsettingselektrone, aangesien monopooloorgange streng verbode is vir gamma-uitstraling. Die monopoolmatrikselement word gedefinieer en die verband met kernstruktuur word uitgewys. Tweedens word 'n kort beskrywing van die mini-orange spektrometer wat in die eksperiment gebruik is, gegee, en die transmissie karakteristieke word bespreek. Die metode wat gebruik is om die transmissiekurwes te bepaal, word uitvoerig beskryf, en 'n paar eksperimentele resultate van sulke transmissiekurwes word gegee. Derdens word die eksperimentele opstelling en kondisies vir die waarneming van die ^{112}Cd omsettingselektronspektrum beskryf, en die resultate van die eksperiment word voorgelê. Die $0^+_1 \rightarrow 0^+_g$ monopole oorgang in ^{112}Cd is waargeneem. Die spektrum is geanaliseer en die resultate is gebruik om die kernstruktuurparameters $\rho(E0)$ en $X(E0/E2)$ te bereken.

Die resultate vergelyk gunstig met dié van ander soortge-

lyke resulate in die literatuur. Die resultate is ook vergelyk met teoretiese voorspellings en dit het duidelik geblyk dat geen een van dié kernmodelle die eksperimentele waarde kan verklaar nie. Dit is dus duidelik dat eksperimente soorgelyk aan die bogenoemde een, belangrik is om verdere inligting oor die kernstruktuur te bekom.

ACKNOWLEDGEMENTS

It is with a feeling of sincere gratitude that I acknowledge the financial assistance which I received from the Research Committee of the University of Zululand during the course of this work. I would also like to use this opportunity to express my gratitude to Prof J F P Sellschop of the Schonland Research Centre at the University of the Witwatersrand for making the facilities at the Research Centre available for some of the experiments, and the scientific and technical staff for their assistance. I am indebted to my colleagues in the Physics Department at the University of Zululand, in particular Prof B Spoelstra, for their constant support and encouragement.

E G Rohwer
1985

CHAPTER 1

INTRODUCTION

The phenomena of internal conversion was discovered by Hahn and Meitner in 1924. The well defined peak of monoenergetic electrons made internal conversion electron energy measurement the most accurate method of determining gamma-ray energies before solid state detectors came into use. The binding energies of the electrons had been well known from X-ray work. When it was realized that internal conversion was not an internal photo-electric effect, measurements of the ratio of conversion electrons to gamma-rays was introduced. The availability of nuclear reactors and sophisticated accelerators after World War II made such conversion coefficient measurements possible and it has ever since been one of the most effective means of assigning spin and parity to nuclear states.

This thesis is intended to provide a brief review of the internal conversion process with emphasis on experimental aspects of internal conversion spectroscopy i.e. transition probabilities, competing electromagnetic transitions, angular distributions of gamma radiation and conversion electrons. It is further the intention to stress the importance of determining E0 transition probabilities for the probing of nuclear models. The ^{112}Cd even-even nucleus was investigated for possible E0 transitions. A strong E0 transition from the 0_1^+ state to the 0_g^+ state was observed and the result is discussed with reference to some nuclear models.

A description of some aspects of the apparatus used, a Mini-orange spectrometer, is given, together with some other experimental details.

CHAPTER 2

ELECTROMAGNETIC TRANSITIONS IN NUCLEI

2.0 Electromagnetic transitions

Since nuclei that are in an excited state where the excitation energy is insufficient for nuclear particle emission, can undergo electromagnetic transitions, energy and transition probability measurements can be used to gain information about the structure of the nucleus. Gamma-radiation, the emission of a single photon from the nucleus, the most common electromagnetic transition, is discussed in this chapter.

2.1 Theory of electromagnetic radiation transition probabilities

Detailed theory on this topic has been presented by several authors (Mos 67, Ald 75). Here follows a brief review.

The total transition probability $T(j_i \to j_j)$ for photon emission between two nuclear states with angular momenta j_i and j_f can be writen as the sum of all the allowed multipole transitions between j_i and j_f which are compatible with the selection rules. (Bla 79, Mos 68, Ald 75, Mor 76).
The total transition probability can be written as

$$T(j_i \to j_f) = \frac{8\pi}{(2j_i+1)\hbar} \sum_{L,\Pi} \frac{(L+1)(\omega/c)^{2L+1}}{L[(2L+1)!!]^2} \left| \langle j_f \| M\Pi,L) \| j_i \rangle \right|^2 \qquad \ldots 2.1.1$$

where the symbols are defined as follows:

L is the angular momentum of electromagnetic radiation carried away by photon in $\hbar$ units,

Π = E for electric multipoles
Π = M for magnetic multipoles
and $\hbar\omega$ is the energy of the electromagnetic radiation, $M(\Pi,L)$ magnetic and electric multipole operators, and $\langle j_f \| M(\Pi,L) \| j_i \rangle$ are thus the so called multipole operator matrix elements which contain information of the structure of the nucleus. Classically these nuclear structure properties would be ascribed to nuclear charge and current distributions.

It is sometimes convenient to write total transition probabilities in terms of absolute transition amplitudes $\gamma(\Pi,L,j_i \to j_f)$ (Ald 75) so that:

$$T(j_i \to j_f) = \sum_{L,\Pi} |\gamma(\Pi,L,j_i \to j_f)|^2 \qquad 2.1.2$$

where $\gamma(\Pi,L,j_i \to j_f) =$

$$i^{L+\Lambda(\Pi)} \left[\frac{8\pi\,(L+1)\,(\omega/c)^{2L+1}}{(2j_i+1)\hbar L\,[(2L+1)!!]^2}\right]^{\frac{1}{2}} \langle j_f \| M(\Pi,L) \| j_i \rangle$$

where $\Lambda(E) = 0$
$\Lambda(M) = 1$ ref. (Kra 75, Kra 77)

The total transition probability is thus separable into the transition probabilities $T(\Pi,L,j_i \to j_f)$ of pure multipole transitions characterized by Π,L.

This also leads to the definition of multipole mixing ratios (Ald 75, Mor 76)

$$\delta(\Pi',L+1;\Pi,L) = \frac{\gamma(\Pi',L+1,\ j_i \to j_f)}{\gamma(\Pi,L,j_i \to j_f)}$$

...2.1.3a

Depending on the convention used δ can be positive or negative. In this work the convention is used as is set out in eq 2.1.2. (Kra 75, Kra 77). It is the same convention as is used by Krane and Steffen (Kra 75, Kra 75, Kra 77). In the event of two mixed multipoles Π,L and $L+1,\Pi',L+1$ eg. M1,E2 mixed multipole transition (see table 2) the mixing ratio δ would given by:

$$\delta = \frac{\gamma(\Pi',L+1)}{\gamma(\Pi,L)} = \frac{\gamma(E2)}{\gamma(M1)} \qquad \ldots 2.1.3b$$

This parameter δ will always be a real number of necessity, considering the definition of $\gamma(\Pi,L)$ (See eq. 2.1.2).

Very often the quantity $\delta^2 = \frac{\gamma^2(\Pi',L+1)}{\gamma^2(\Pi,L)}$ ...2.1.3c
is used in experimental work as for example in the determination of angular distributions of gamma-rays and determination of conversion coefficients. (See section 2.4).

From the definition of $\gamma(\Pi,L)$ it is clear that

$$\delta^2 = \frac{T(\Pi',L+1,j_i \rightarrow j_f)}{T(\Pi,L,j_i \rightarrow j_f)}$$

where $T(\Pi,L,j_i \rightarrow j_f)$ is the total transition probability of only the specific multipole (Π,L), over 4π.

Hence $\delta^2 = \frac{I(\Pi',L+1)}{I(\Pi,L)}$ ...2.1.3e
where $I(\Pi,L)$ is the intensity of the multipole radiation (Π,L) over 4π. (Ald 75, Mor 76).

When considering nuclear deexcitation, it is often convenient to separate the energy dependent and the nuclear structure part of the expression of the transition probability.

This is achieved by introducing the reduced transition probability (Mos 68, Ald 75)

$$B(\Pi,L,j_i \to j_f) = \frac{\left| \langle j_f \| M(\Pi,L) \| j_i \rangle \right|^2}{2j_i + 1} \quad \ldots 2.1.4$$

which contains the nuclear structure part, so that

$$T(j_i \to j_f) = \sum_{L,\Pi} \frac{8\pi\,(L+1)\,(\omega/c)^{2L+1}}{\hbar\, L\,[(2L+1)!!]^2}\, B(\Pi,L,\, j_i \to j_f) \quad \ldots 2.1.5$$

It is obvious that $B(\Pi,L,\, j_i \to j_f)$ is model dependent and independent of the energy of the transition and is hence a convenient quantity to determine experimentally and to test the nuclear structure model in question.

TABLE 1

Electric transitions $B(EL)$ in $e^2 fm^{2L}$	Magnetic transitions $B(ML)$ in $\mu_N fm^{2L-2}$
$T(E1) = 1{,}59 \times 10^{15}\ E\ ^3B(E1)$	$T(M1) = 1{,}76 \times 10^{13}\ E\ ^3B(M1)$
$T(E2) = 1{,}22 \times 10^{9}\ E\ ^5B(E2)$	$T(M2) = 1{,}35 \times 10^{7}\ E\ ^5B(M2)$
$T(E3) = 5{,}67 \times 10^{2}\ E\ ^7B(E3)$	$T(M3) = 6{,}28 \times 10^{0}\ E\ ^7B(M3)$
$T(E4) = 1{,}69 \times 10^{-4}\ E\ ^9B(E4)$	$T(M4) = 1{,}87 \times 10^{-6}\ E\ ^9B(M4)$

TABLE 1 Transition probabilities (in units s^{-1}) of electromagnetic multipole transitions in nuclei. Energy E in MeV.

From the energy dependent part it is clear that the transition probability increases with increase in transition energy $\hbar\omega$ for a particular multipole transition. This is also reflected in Table 1. (Mor 76, Ald 75).

.2 Selection rules

The summation in eq. 2.1.1 is done over the allowed values of (Π,L) for a transition between an initial state with angular momentum j_i and parity Π_i and a final state with angular momentum j_f and parity Π_f.
The possible values are determinend by the following selection rules:

a) Angular momentum.
$|j_i - j_f| \leq L \leq j_i + j_f$
(and $m = m_i - m_f$)

b) Parity: Since electromagnetic multipole operators $M(\Pi,L)$ have well defined parity Π, matrix elements $\langle j_f \| M(\Pi,L) \| j_i \rangle$ are only non vanishing if

$$\Pi_i \Pi_f = (-1)^{L + \Lambda(\sigma)}$$

Hence for magnetic multipole transitions
$\Pi_i \Pi_f = (-1)^{L+1}$
and for electric multipole transitions
$\Pi_i \Pi_f = (-1)^{L}$

Single photon emission of order $L = 0$ is prohibited since the angular momentum carried away by a photon must be $> 1\ \hbar$. (Mor 76)

In general it can be seen that an electromagnetic transition between two nuclear states $j_i \Pi_i$ and $j_f \Pi_f$ will be a mixture of several allowed multipole transitions. The domination of one particular multipole radiation depends on the transition probabilities of the competing multipole transitions. (See eq. 2.1.3).

Three transitions need special mention:

1. If j_i or $j_f = 0$ then only one multipole transition will be possible and will be characterized by angular momentum $L = j_i$ or $L = j_f$ whichever is non-zero.

2. When $j_i = j_f = 0$ only E0 or M0 transitions would be possible but are both rigorously prohibited for single photon radiation as mentioned earlier.

3. If $j_i = j_f = \frac{1}{2}$ only dipole (L=1) radiation is allowed, E1 or M1, depending on the parities of the states, Π_i and Π_f. (Wil 60).

2.3 Transition probabilities and reduced transition probabilities

A. Nuclear structure and emmission of gamma-radiation

In the preceding paragraphs it was shown that transition probabilities can be separated into two components. (See eq. 2.1.5)

$$T(\Pi,L,j_i \to j_f) = \frac{8\pi\,(L+1)(\omega/c)^{2L+1}}{\hbar\, L[(2L+1)!!]^2}\, B(\Pi,L,j_i \to j_f)$$

Transition probabilities can be determined experimentally by several methods such as lifetime measurements, angular correlation and Coulomb excitation experiments. If the

multipolarity (Π,L) of the transition as well as the energy $\hbar\omega$ of the transition is known, the reduced transition probability can be determined. Reduced matrix elements $\langle j_f \| M(\Pi,L) \| j_i \rangle$ can be calculated by using the nuclear wave function based on a particular nuclear model. In this way, by comparing experimental and theoretical $B(\Pi,L,j_i \to j_f)$ values, the validity of assumptions made in the specific nuclear model can be tested. A detailed description of various nuclear models and the theoretical $B(\Pi,L,j_i \to j_f)$ values, can be found in articles by Alder and Steffen (Ald 75) and Kumar. (Kum 75).

There are two extreme models:

1. The single particle approximation, in which only one nucleon is assumed to be excited as in the shell model,

2. the collective approximation in which it is assumed that several nucleons together contribute to the radiation, as in the vibrational model.

The nuclear shell model in which one proton moves in an average potential can be used to obtain an indication of the order of magnitudes of $B(\Pi,L,j_i \to j_f)$ and $T(\Pi,L,j_i \to j_f)$ and their dependance on parameters such as A, the number of nucleons in the nucleus, and the multipolarity (Π,L) of the transitions.

B. Weisskopf single particle estimate

The Weisskopf single particle estimate is such a shell model prediction of reduced transition probabilities $B(\Pi,L,j_i \rightarrow j_f)$. Detailed descriptions thereof are numerous. (Bla 79, Mor 76, Mos 68, Ald 75). The Weisskopf estimate F, (or Weisskopf unit Wu) is often used to characterize such reduced transition probabilities in terms of the number of Weisskopf units, (Bla 79, Mor 76) where

$$F = \frac{B(\Pi,L)}{B(\Pi,L)_W} , \qquad ...2.3.1$$

where $B(\Pi,L)$ is the actual reduced transition probability and $B(\Pi,L)_W$ is the Weisskopf single particle estimate. For electric multipole radiation the estimate is given by (Bla 79,Ald 75)

$$B(EL)_W = \frac{9\ e^2 R^{2L}}{4\pi(L+3)^2}$$

with R the radius of the nucleus. It is customary to use $R = r_o A^{1/3}$ with $r_o = 1,2$ [fm], and to express $B(EL)_W$ in units of $e^2 [fm]^{2L}$.
In these units

$$B(EL)_W = \frac{(1,2)^{2L}(3/L+3)^2 A^{2L/3}}{4\pi} \qquad ...2.3.2$$

Estimates for magnetic multipole radiation can be obtained in a similar way. In this case the units are customarily $\mu_N^2 [fm]^{2L-2}$ and in these units

$$B(ML)_W = \frac{10(1,2)^{2L-2}\ (3/L+2)^2\ A^{(2L-2)/3}}{\pi} \qquad ...2.3.3$$

Using these estimates, and with the use of table 1, values for T_W can be obtained. In figure 1 the dependence of T_W on A for electric- and magnetic-multipole transitions is illustrated.

FIGURE 1

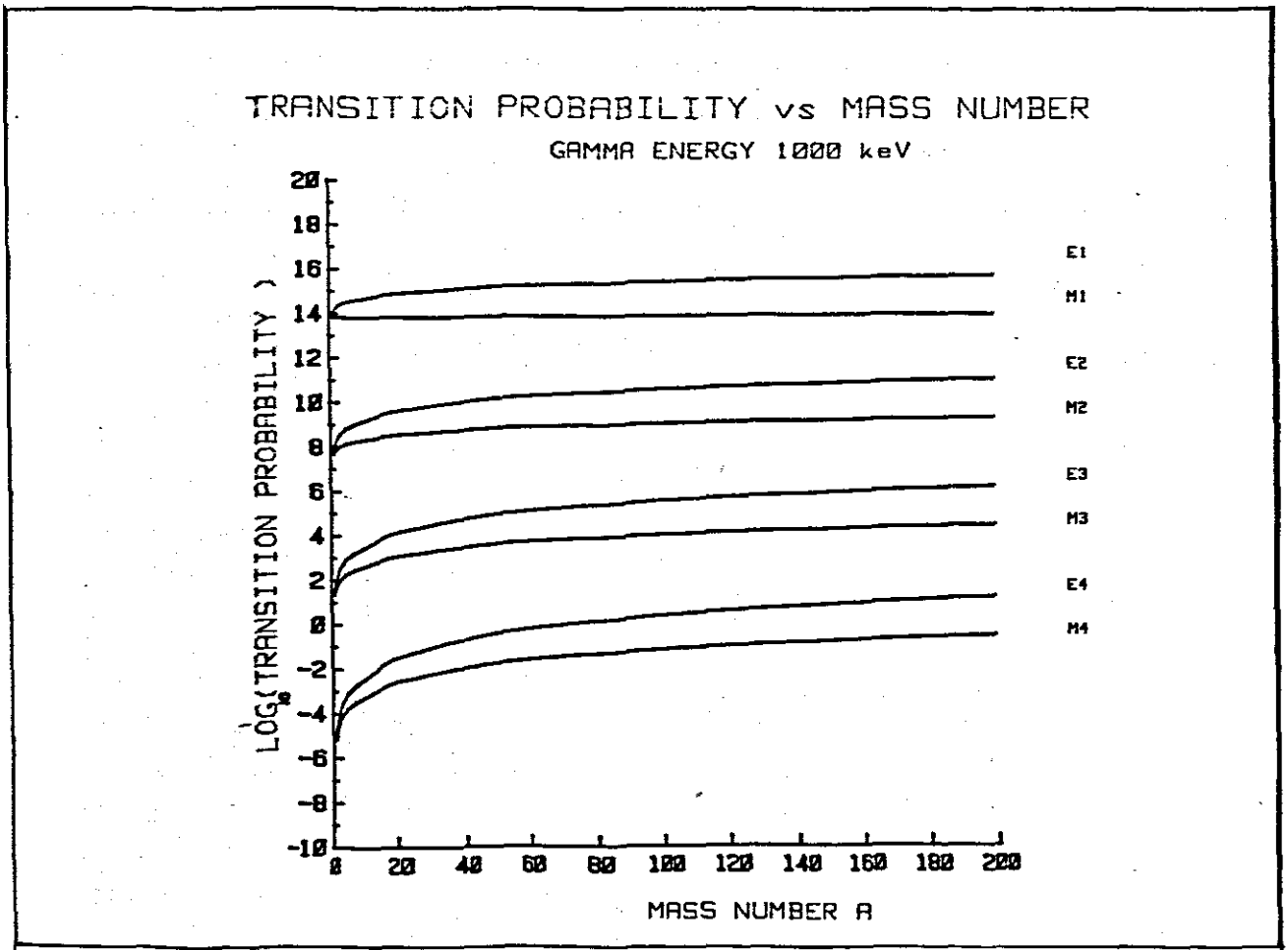

FIGURE 1: Gamma-decay transition probability T_W in s^{-1} as a function of A, the mass number, for various multipolarities, for transition energy 1 000 keV. The graphs were drawn using $T_W = \frac{8\pi(L+1)(\omega/c)^{2L+1}}{\hbar L[(2L+1)!!]^2} B_W$ with B_W as given by eqs. 2.3.2 and 2.3.3.

Using the single particle estimate for electric multipole transition, and discarding constants, the transition probability $T(\Pi,L,j_i \to j_f)_W$ becomes

$$T(\Pi,L,j_i \to j_f)_W \sim \frac{\omega^{2L+1}(L+1)\,R^{2L}}{[(2L+1)!!]^2 L\,(L+3)^2} \qquad \ldots 2.3.4$$

In a particular nucleus, even for 2 MeV transitions in large nuclei $\omega R << 1$, so that the transition probability decreases drastically with higher multipole order L for a transition with energy $\hbar\omega$. Hence in a transition where several multipole transitions are allowed only the first two lowest order multipoles are taken into account in the summation in eq. 2.1.1. Figure 2 illustrates this fact.

FIGURE 2

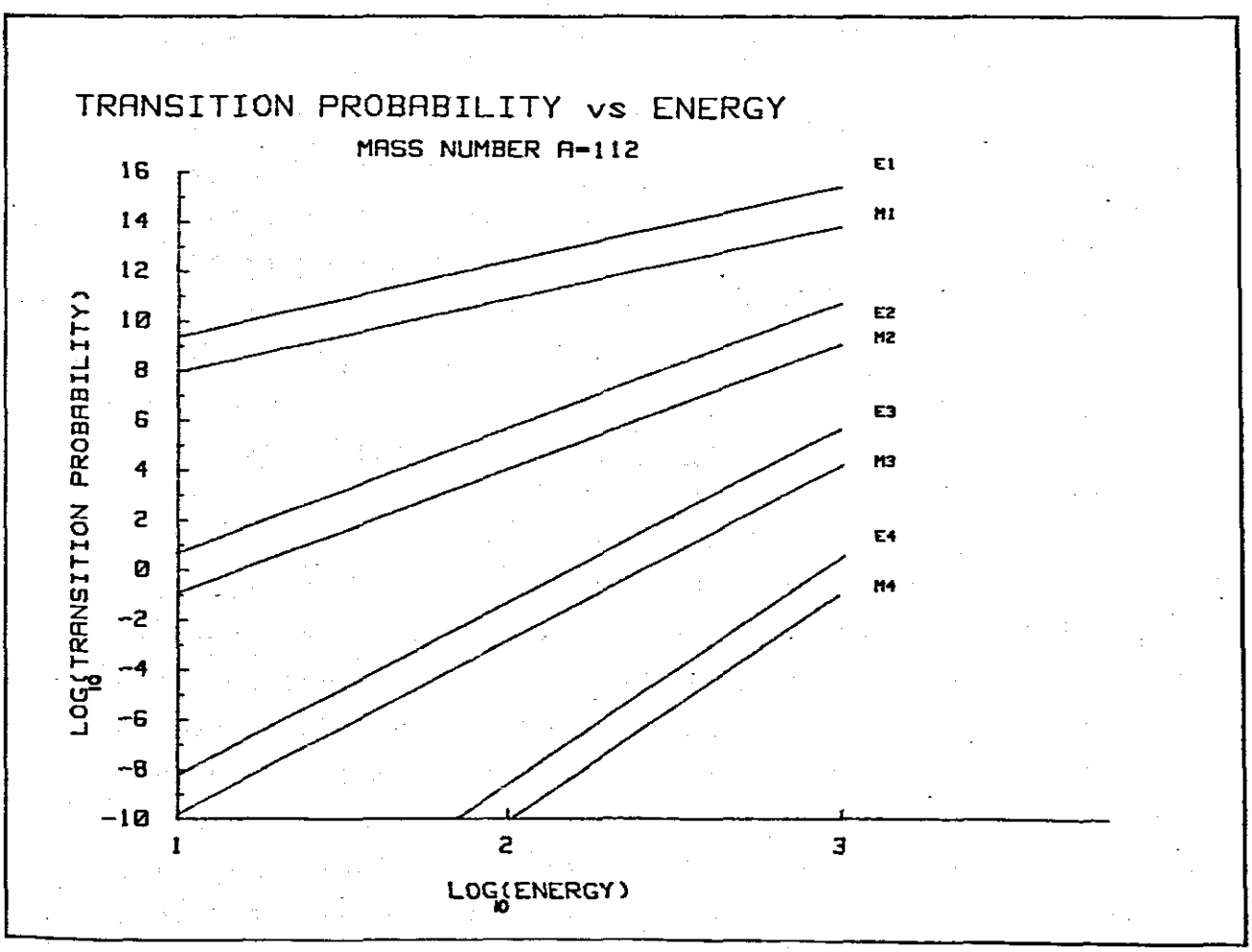

FIGURE 2: Gamma-decay transition propability T_W in s^{-1} as a function of gamma-ray energy E in keV for various multipolarities. A = 112. The graphs were drawn using $T_W = \frac{8\pi(L+1)(w/c)^{2L+1}}{\hbar L[(2L+1)!!]^2} B_W$ with B_W as given by eqs. 2.3.2 and 2.3.3.

TABLE 2

Parity change $\Delta\pi$	Change in angular momentum $\lvert j_i - j_f \rvert$				
	0 or 1	2	3	4	5
no	M1(E2)	E2(M3)	M3(E4)	E4(M5)	M5(E6)
yes	E1(M2)	M2(E3)	E3(M4)	M4(E5)	E5(M6)

TABLE 2: Possible multipolarities for gamma-radiation (Mos 68).

Table 2 lists mulipolarities to be expected for a gamma-transition between two states of specified angular momenta and parities. The lowest two orders are given; the second is in parenthesis to denote that it is usually insignificant. It has been assumed that the condition $\lvert j_i - j_f \rvert \leq L$ is satisfied.

2.4 Angular distribution of gamma-rays

It is well known that electromagnetic radiation from orientated (aligned) nuclei show angular dependence. In an in-beam experiment, the accelerated particle imparts angular momentum to the target nucleus. The angular momentum of such a nucleus is aligned in a plane perpendicular to the beam direction. This results in anisotropic emission of electromagnetic radiation. The angular distribution ($W(\theta)$) of electromagnetic radiations can be presented as an expansion in terms of Legendre polynomials, $P_k(\cos\theta)$. (Yam 67, Mor 76, Fau 83, Ste 75, Ham 75, Gro 68.)

$$W(\theta) = \sum_{k=0}^{\infty} a_k P_k(\cos\theta), \qquad \ldots 2.4.1$$

with k even, and a_k are constants, and θ is the angle with beam direction.
Some lower order Legendre polynomials are:

$$P_0(\cos\theta) = 1$$
$$P_2(\cos\theta) = 1/4\ (1 + 3\cos 2\theta)$$
$$P_4(\cos\theta) = 1/64\ (9 + 20\cos 2\theta + 35\cos 4\theta)$$
$$P_6(\cos\theta) = 1/512\ (50 + 105\cos 2\theta + 126\cos 4\theta + 231\cos 6\theta)$$

The intensity distribution $W(\theta)$ is axially symetrical around the beam-direction, and magnetic and electric multipole radiations of the same order have the same distribution.
The k = 0 term clearly is only a constant contribution of intensity due to isotropic radiation, and since one is only interested in angular distribution coefficients, it is convenient to normalize and choose $a_0 = 1$, and then

$$W(\theta) = 1 + \sum_{k=0}^{\infty} A_k P_k(\cos\theta) \qquad k \text{ even} \qquad \ldots 2.4.2$$

The coeficients A_k are normilized in order to have
$\int_0^{4\pi} W(\theta)\, d\Omega = 4\pi$. (Gro 68.)

The factors A_k are represented by

$$A_k = B_k F_k(L, L', j_i, j_f) \qquad \ldots 2.4.3$$

Where F_k are the angular distribution coefficients, depending on the initial and final spin states j_i and j_f, on the multipole radiations emmitted L and L'. These values can be obtained from tables. (See table 4.) (Yam 67, Hag 68). The coefficients B_k are the statistical tensors for complete alignment which only depend on the angular momentum of the initial state j_i and the values can be found in tables. (Yam 67)

TABLE 3

j_i	B_2	B_4	B_6
0	0	0.	0
1	-1.41421	0.	0.
2	-1.19523	1.60357	0.
3	-1.15470	1.27920	-1.74078
4	-1.13961	1.20687	-1.34830
5	-1.13228	1.17670	-1.25245
6	-1.12815	1.16888	-1.20977
7	-1.12560	1.15147	-1.18678
8	-1.12390	1.14531	-1.17175
9	-1.12272	1.14112	-1.16206
10	-1.12187	1.13811	-1.15524
11	-1.12122	1.13588	-1.15025
12	-1.12073	1.13418	-1.14648
13	-1.12034	1.13285	-1.14356
14	-1.12004	1.13178	-1.14125
15	-1.11979	1.13053	-1.13830
16	-1.11958	1.13022	-1.13786
17	-1.11941	1.12988	-1.13660
18	-1.11926	1.12818	-1.13554
19	-1.11914	1.12873	-1.13465
20	-1.11903	1.12537	-1.13388

TABLE 3: Statistical Tensors for Complete Alignment $B_k(j_i)$. The Table of B_k values was taken from ref. (Yam 67.)

From this table it is clear that $B_k(j_i)$ does not differ drastically for different j_i. It should be noted that $B_k(0)=0$, which is obvious since an angular momentum vector of magnitude 0h can not be aligned.

This implies that all radiations from $j_i = 0$ will be emmitted isotropically. For this reason no values of F_k for $j_i = 0$ are given in Table 4.

If one is only considering dipole and quadrupole radiation, the expansion ends with the P_2-term or the P_4-term respectively since no Legendre polynomials of order larger than 2L appear. This is because the coefficients A_k vanish for values $k > 2L$ since F_k's are zero. (See Table 4).

When alignment is incomplete, as is the case in most experimental situations, it is necessary to introduce attenuation coefficients α_2 and α_4 to be able to make sensible interpretation of experimental angular distributions. (Mat 74) If an experiment yields results A_2' and A_4' these results should be equated to $\alpha_2 A_2$ and $\alpha_4 A_4$ respectively

Hence $A_2' = \alpha_2 A_2$; $A_4' = \alpha_4 A_4$.

Partial alignment is due to a Gaussian distribution of all the allowed m-states characterized by the half-width σ of the assumed Gaussian distribution. It is therefore obvious that the α_k's will depend on σ and j_i, the initial state spin, and tables of such attenuation coefficients α_k as a function of σ/j_i were presented by Der Mateosian et al (Mat 74) Since σ is not known, one can only assume to have found a possible description of the excited state of the nucleus if the experimental values of α_2 and α_4 can be found associated with the same σ/j_i value. [From the Tables in ref. (Mat 74)].

In the case of mixed multipole radiation the coefficients A_k contain coefficients $F_k(L,L',j_i,j_f)$ of pure multipolarities $F_k(L,L,j_i,j_f)$ and $F_k(L',L',j_i,j_f)$ as well as an interference term $F_k(L,L',j_i,j_f)$ and the mixing parameter δ, where $L = |j_i - j_f|$ the lowest allowed multipole transition, and $L' = L+1$.

TABLE 4

j_i	j_f	L	L'	F_2	F_4
1	0	1	1	.70711	0.
1	1	1	1	-.35355	0.
1	1	1	2	-1.06066	0.
1	1	2	2	-.35355	0.
1	2	1	1	.07071	0.
1	2	1	2	.47434	0.
1	2	2	2	.35355	0.
1	3	2	2	-.10102	0.
1	3	2	3	.37796	0.
1	3	3	3	.53055	0.
1	4	3	3	-.17678	0.
2	0	2	2	-.59761	-1.06904
2	1	1	1	.41833	0.
2	1	1	2	-.93541	0.
2	1	2	2	-.29891	.71270
2	2	1	1	-.41833	0.
2	2	1	2	-.61237	0.
2	2	2	2	.12806	-.30544
2	3	1	1	.11952	0.
2	3	1	2	.65465	0.
2	3	2	2	.34149	.07636
2	4	2	2	-.17075	-.00848
2	4	2	3	.50508	-.06274
2	4	3	3	.44821	-.02970
2	5	3	3	-.29881	.00405
3	0	3	3	-.86603	.21320
3	1	2	2	-.49487	-.44671
3	1	2	3	-.46291	1.04464
3	1	2	3	-.64557	.03553
3	2	1	1	.34641	0.
3	2	1	2	-.94868	0.
3	2	2	2	-.12372	.67006
3	3	1	1	-.43301	0.
3	3	1	2	-.43301	0.
3	3	2	2	.22682	-.44671

TABLE 4: Angular distribution coefficients $F_k(L,L',j_i,j_f)$ for j_i and j_f integer spins. The table was taken from ref. (Yam 67).

In this case the factor $A_k(\delta)$ is given by:

$$A_k(\delta) = B_k \frac{1}{1+\delta^2} [F_k(L,L',j_i,j_f) + 2\delta F_k(L,L',j_i,j_f,)$$

$$\delta^2 F_k(L',L',j_i,j_f)] \qquad ...2.4.4$$

Refs. (Yam 67, Fau 83, Ham 75)
Obviously this general formula reduces to eq. 2.4.3 if δ = 0, where δ is given by eq. 2.1.3 and δ^2 measures the ratio of the intensities of the multipolarities involved.

Example: $j_i = 2$, $j_f = 1$
$L = 1$
$L' = 2$

$$A_2 = B_2 \frac{1}{1+\delta^2} [F_2(1,1,2,1) + 2\delta F_2(1,2,2,1) + \delta^2 F_2(2,2,2,1)]$$

It should be noted that δ will be negative for a M2/E1 mixture and positive for a E2/M1 mixture. (See definition of δ in eq. 2.1.3)

The coefficients F_k have the following properties:

i) $F_o(L,L',j_i,j_f,) = \delta_{LL'}$ (kronecker delta)

ii) $F_k(L,L',j_i,j_f) = F_k(L',L,j_i,j_f)$

iii) $F_k(L,L',j_1,j_2) \neq F_k(L,L',j_2,j_1)$

ref. (Ste 75)

Property (i) implies that A_o is independent of δ:

$$A_0 = \frac{1}{1+\delta^2}\,[F_0(L,L,j_i,j_f) + 2\delta F_0(L,L',j_i,j_f) + \delta^2 F_0(L',L',j_i,j_f)$$

$$= \frac{1}{1+\delta^2}\,[1 + 2\delta.0 + {}^2\delta\,.1]$$

$$= 1$$

Once again in the case of multipole mixing, experimental values A_k' will be obtained, which now depend on δ and σ/j_i which are both unknown. Many combinations of σ and δ values would correspond to the obtained A_2' and A_4'. However there would only be one set of σ and δ values which simultaneously satisfy the condition for A_2' and A_4'. These values would then be accepted as the proper set of σ and δ values. A very detailed account of this problem is given by Der Mateosian et al (Mat 74) together with convenient tables.

Additional attenuation factors q_k have to be introduced to take into account the fact that, in actual measurement, the detector subtends a solid angle. (Fau 83, Fee 79). Faust (Fau 83) gives these attenuation factors as:

$$q_2 = \tfrac{1}{2}\cos\alpha_0(1+\cos\alpha_0)$$

$$q_4 = 1/8\,\cos\alpha_0(1+\cos\alpha_0)\,(7\cos^2\alpha_0 - 3)$$

where $2\alpha_0$ is the angle of acceptance of the detector sytem.

Hence in an experimental arrangement $W(\theta)$ would be given by:

$$W(\theta) = \sum_{k=0}^{\infty} A_k' q_k P_k(\cos\theta) \qquad k \text{ even}$$

$$= \sum_{k=0}^{\infty} \alpha_k A_k q_k P_k(\cos\theta) \qquad k \text{ even}$$

...2.4.5

Figures 3, 4 and 5 are included to assist in visualizing the angular distribution effect for various cases. The graphs were plotted by calculating $W(\theta)$ as set out in eq. 2.4.2 and using the relevant values of F_k and B_k from tables 3 and 4.

FIGURE 3

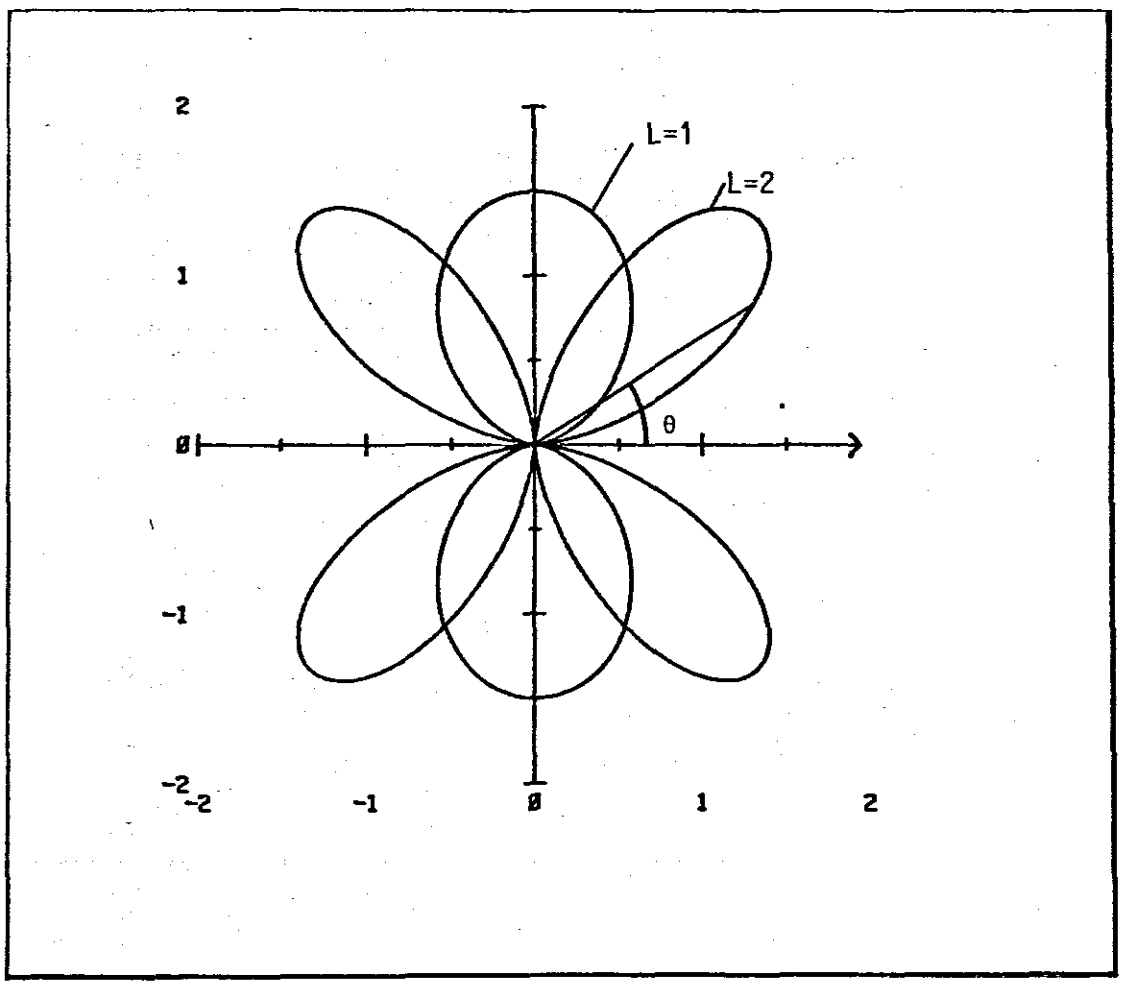

FIGURE 3: The angular distribution $W(\theta)$ for gamma-rays as a function of θ, the angle with the beam-direction for pure L = 1 and L = 2 radiations, assuming complete alignment. (Also see ref. (Gro 68)).

FIGURE 4

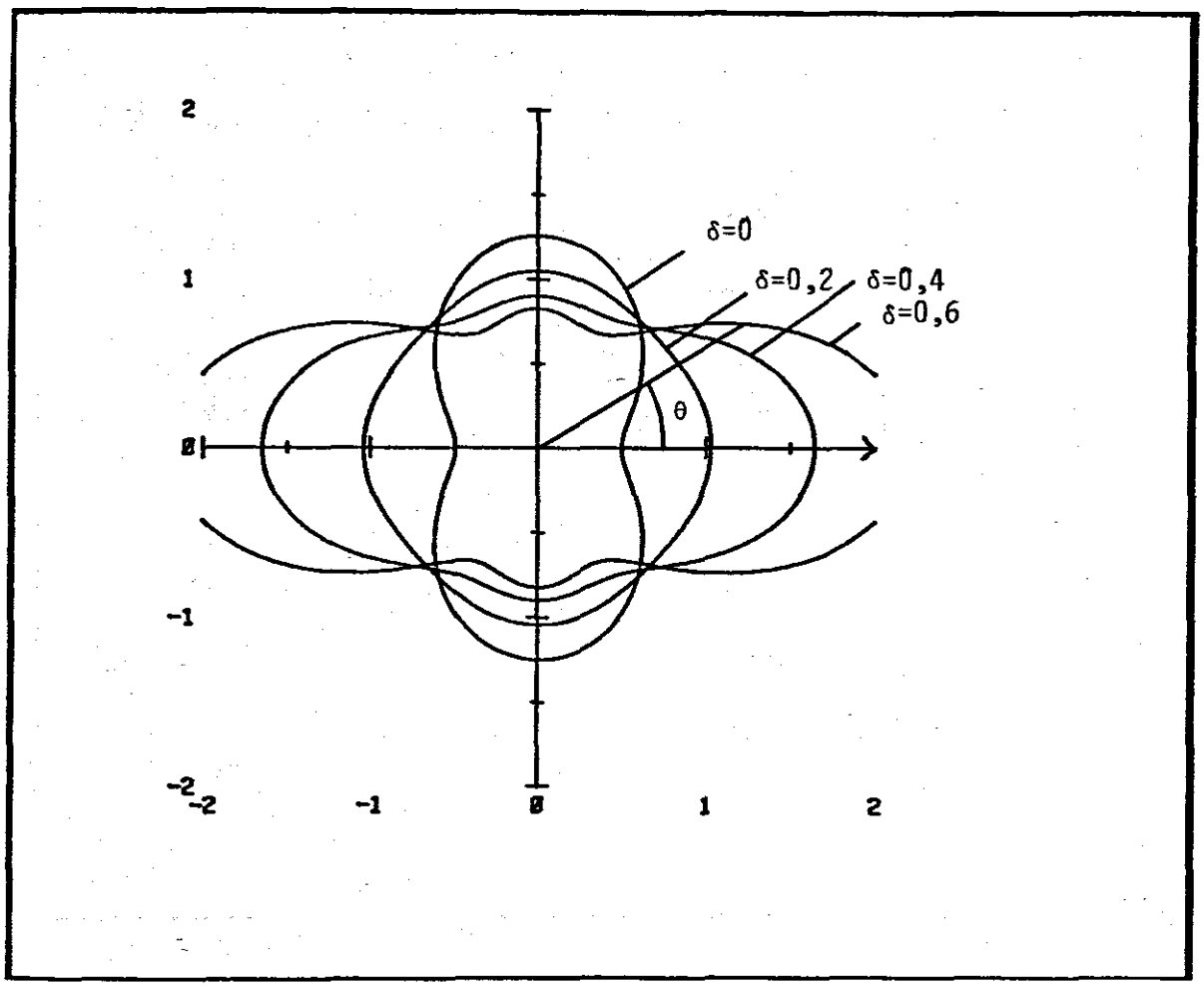

FIGURE 4: The angular distribution W(θ) for gamma-rays as a function of θ, the angle with the beam-direction for mixed M1, E2 multipole radiations for different values of δ, assuming complete alignment.
Also see ref. (Gro 68).

FIGURE 5

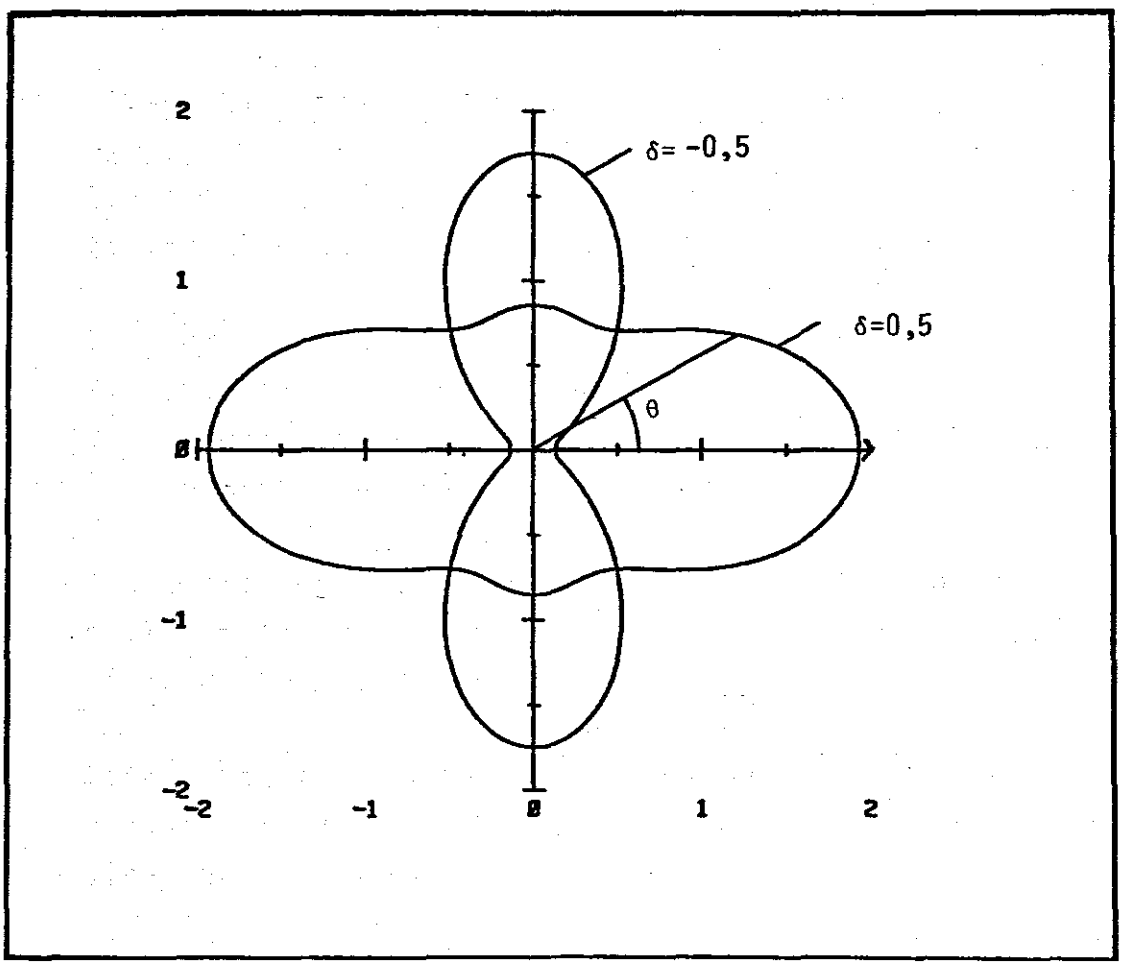

FIGURE 5: The angular distribution $W(\theta)$ for gamma-rays as a function of θ, the angle with the beam-direction for M1/E2 mixture with $\delta = +0,5$ and for E1/M2 mixture with $\delta = -0,5$. Complete alignment is assumed. Also see ref. (Gro 68).

CHAPTER 3

ALTERNATIVE ELECTROMAGNETIC DEEXCITATION PROCESSES

3.0 Alternative electromagnetic deexcitation processes

Apart from single photon emmission there are also other competing electromagnetic transition processes:

1. Emmission of two or more photons simultaneously,
2. Internal conversion
3. Internal pair production when $\hbar\omega > 2mc^2$
4. Internal conversion plus photon.

Transition probabilities for processes 1) and 4) are very small compared to single photon transition probabilities and will not be dealt with here. (Bor 63).

Pair production and electron conversion can in some cases compete favourably with γ-radiation and therefore needs considering.

3.1 Internal conversion

A. General

Internal conversion is the electromagnetic deexcitation process of nuclei by which an atomic electron is emitted, in competition to gamma-radiation. These monoenergetic electrons have energy $T = \hbar\omega - B$ where $\hbar\omega$ is the transition energy of nuclear deexcitation (neglecting the nuclear recoil energy) and B is the binding energy of the atomic electron. Transitions are defined as magnetic and electric as in the case of gamma-transitions.

The internal conversion process is an electromagnetic interaction between the nucleus and an atomic electron. The existence of E0 internal conversion electrons proves that it is not an internal photoelectric effect. The internal conversion process is thus independent of the gamma-transition probability and angular distribution.

Internal conversion is also of particular interest since E0 transitions, totally prohibited in gamma-deexcitation, are possible. The E0 transitions compete favourably with E2 and M1 gamma-radiation in cases where $j_i = j_f \neq 0$, and for a $0^+ \rightarrow 0^+$ transition, E0 internal conversion is the dominating method of electromagnetic deexcitation. Internal pair production is also possible if energy $\hbar\omega > 2mc^2$. The nuclear matrix element, $\rho(E0)$ which is obtained from such an E0 transition probability, yields valuable information about the nuclear structure.

B. Internal conversion coefficient

Considering energy transitions below 1 000 keV, and hence neglecting internal pair formation and other second order processes, the total electromagnetic transition probability, $T(j_i \rightarrow j_f)$ is given by:

$$T(j_i \rightarrow j_f) = T_\gamma(j_i \rightarrow j_f) + T_{int}(j_i \rightarrow j_f) \qquad \ldots 3.1.1$$

with

T_γ = gamma-transition probability

T_{int} = internal conversion electron transition probability

The total internal conversion coefficient is the defined as:

$$\alpha = \frac{T_{int}(j_i \to j_f)}{T_\gamma(j_i \to j_f)} \qquad \ldots 3.1.2$$

hence $T(j_i \to j_f) = (1+\alpha)T_\gamma(j_i \to j_f)$

Very often it is convenient to define conversion coefficients for each shell or subshell eg.

$$\alpha_K = \frac{T_K(j_i \to j_f)}{T_\gamma(j_i \to j_f)} \qquad \text{for K subshell}$$

The total conversion coefficients is then the sum of all the partial conversion coefficients.

$$\alpha = \alpha_K + \alpha_{LI} + \alpha_{LII} + \alpha_{LIII} + \ldots\ldots$$

It should be noted that it is meaningless to define a coefficient for monopole transitions since there are no monopole radiation of gamma-rays.

Several methods are used to determine conversion coefficients, but will not be discussed here. (See eg. ref. Ham 75, Ham 66, Egi 70). It should be mentioned that with the experimental arrangement used in this work, (Chapter 4) the NPG method (Normalized Peak-to-Gamma) would probably be the most convenient to use.

C. Estimate of conversion coefficients

Consider a point nucleus, with no screening or penetration effects, assuming that it is a low energy transition so that

$R << \lambda_e \sim \lambda_\gamma < R_n$, where

R is the nuclear radius
R_n is the radius of the n-th shell electron orbit
λ $= c/\omega$ for photon
λ_e $= 1/k = \hbar/p$ where p is momentum of electron

It was shown in Chapter 2, eq's. 2.1.4 and 2.1.5 that in such an approximation the gamma transition probability $T_\gamma(EL, j_i \to j_f)$ of one specific pure electric multipole of order L is given by:

$$T(EL, j_i \to j_f) = \frac{8\pi(L+1)(\omega/c)^{2L+1}}{\hbar L[(2L+1)!!]^2} \quad \frac{|\langle j_f \| M(EL) \| j_i \rangle|^2}{2j_i+1}$$

For internal conversion the transition probability is given by:

$$T_{int}(EL, j_i \to j_f) = \frac{2\pi}{\hbar} |\langle f \| H_{int} \| i \rangle|^2 \rho(E) \qquad ...3.1.3$$

ref. (Ham 75)

where $\rho(E)$ is the final electron state energy density given by $\rho(E) = V\frac{m\hbar k}{2(2\pi\hbar)^3} d\Omega$, with V the normalizing volume and $k = p/\hbar$,

$|i\rangle$ and $|f\rangle$ are the initial and final electron states respectively and

H_{int} is the internal conversion Hamiltonian. In this approximation H_{int} is essentially a coulomb interaction between the nucleus and the electron in the atomic shell. The initial electron state is then given by $|i\rangle = |j_i\rangle \phi_n(r)$ where $|j_i\rangle$ is the initial nuclear state and $\phi_n(r)$ is the wave funtion of the electron in the n-th shell, and the final electron state $|f\rangle$ is given by $|j_f\rangle e^{ikr}$ where e^{ikr} is the wave function of the free electron and $|j_f\rangle$ is the final nuclear state.

It can be shown (Bla 79, Pau 75) that the internal conversion probability for n-th shell electron T_n is given by:

$$T_n(EL, j_i \to j_f) = \frac{64\pi m e^2 k^{2L-3} \left| \langle j_f \| M(EL) \| j_i \rangle \right|^2}{\hbar^3 a^3 [(2L+1)!!]^2 2j_i + 1}$$

where a is the radius of the n-th shell electron and $a = a_0 n/Z$, ($a_0 \hbar^2/me^2$, Bohr radius.) Since there are two electrons per subshell the above transition probability is multiplied by two.

$$\text{Hence } \alpha_n = \frac{T_n(EL, j_i \to j_f)}{T_\gamma(EL, j_i \to j_f)}$$

$$= \frac{16Lk^{2L-3}me^2}{(L+1)(\omega/c)^{2L+1}\hbar^2 a^3} \qquad \ldots 3.1.4$$

The energy of the electron emitted is

$$\frac{\hbar^2 k^2}{2m} = E - B_n$$

where $E = \hbar\omega$ the transition energy, and B_n = binding energy of the electron in the n-th shell. For transitions under consideration, i.e. the higher energy transitions such that $\lambda_\gamma < a$; the binding energy $B_n \ll E$ and hence

$$\frac{\hbar^2 k^2}{2m} \simeq \hbar\omega \quad \text{and} \quad k^2 \simeq \frac{2m\omega}{\hbar}$$

Substitution of these values into eq. 3.1.4 and using

$a = a_o n/Z$ and $a_o = \hbar^2/me^2$,

$$\alpha_n = (Z/n)^3(e^2/m\hbar)^4(L/L+1)(2mc^2/\hbar\omega)^{L+5/2} \quad ...3.1.5$$

Similarly the conversion coefficient β_n for a specific magnetic multipole of order L, is given by

$$\beta_n = (Z/n)^3(e^2/m\hbar)^4(2mc^2/\hbar\omega)^{L+3/2} \quad ...3.1.6$$

(Pau 75, Bla 79)

D General considerations

i) Electric and magnetic multipole transitions

In general the magnetic multipole conversion coefficient β_n is larger than for the corresponding electric multipole conversion coefficient α_n for the same energy since

$\alpha_n/\beta_n = (\hbar\omega/mc^2)(L/L+1) < 1$ at low energies. ×

Clearly for transitions where $\hbar\omega >> 2mc$ the situation can be reversed.

ii) Energy of transitions

For both magnetic and electric transitions the conversion coefficients depend on the energy of the transition.

$$\alpha_n \propto \omega^{-(L+5/2)}$$

$$\beta_n \propto \omega^{-(L+3/2)}$$

This implies that measurement of conversion electrons at low energies is very useful, since the transition probability of gamma-rays is very low at these energies. A typical value of α_K for an E3 transition, Z = 48 at 110 keV, is α_K = 4,99. (Rös 78). One should however also keep in mind that the conversion electron transition probability T_n, generally increases with energy as the gamma-transition probability increases, since the transition probability is given by:
$T_n(EL, j_i \to j_f) = \alpha_n T(EL, j_i \to j_f)$, and

$$T_n(EL, j_i \to j_f) \propto \omega^{L-3/2}.$$

Thus, except for El transitions T_n increases with energy, also for monopole transitions which will be discussed in section 3.2. Similarly $T_n(ML, j_i \to j_f) \propto \omega^{L-\frac{1}{2}}$, so that the argument also holds for magnetic transitions.

iii) Multipolarity of transition

For electric multipole transition the conversion coefficient $\alpha \propto (L/L+1)(2mc^2/\hbar\omega)^{L+5/2}$ so that for transition energy $\hbar\omega < 2mc^2$, the coefficient α increases with multipolarity L.

The same argument holds for β, the magnetic multipole coefficient since $\beta \propto (2mc^2/\hbar\omega)^{L+3/2}$. However, since the gamma-transition probability T_γ drastically decreases with multipolarity L, (see eq. 2.3.4) conversion electron transition probability also decreases. In an experiment where conversion electrons are detected, only the lowest multipole orders allowed in the specific transition are considered, as is the case with gamma-transitions. The dependence of conversion coefficients on multipolarity makes measurement of conversion coefficients a very useful means of determining spin and parity of excited nuclear states. (Ham 75, Jham 66).

FIGURE 6

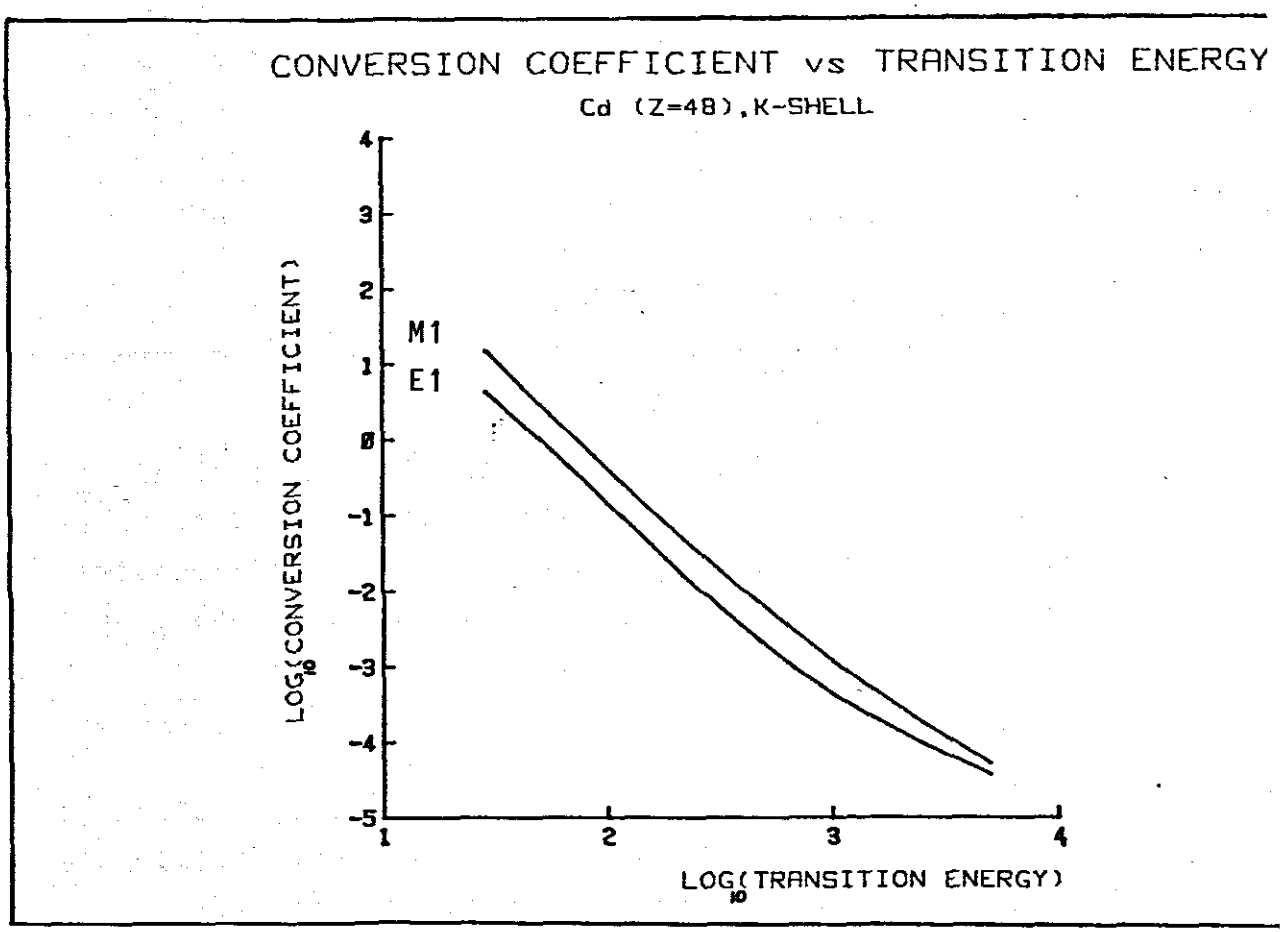

FIGURE 6 Graph of E1 and M1 K-shell conversion coefficients vs transition energy in keV. The graph was obtained by interpolating values from tabled values (Rös 75).

FIGURE 7

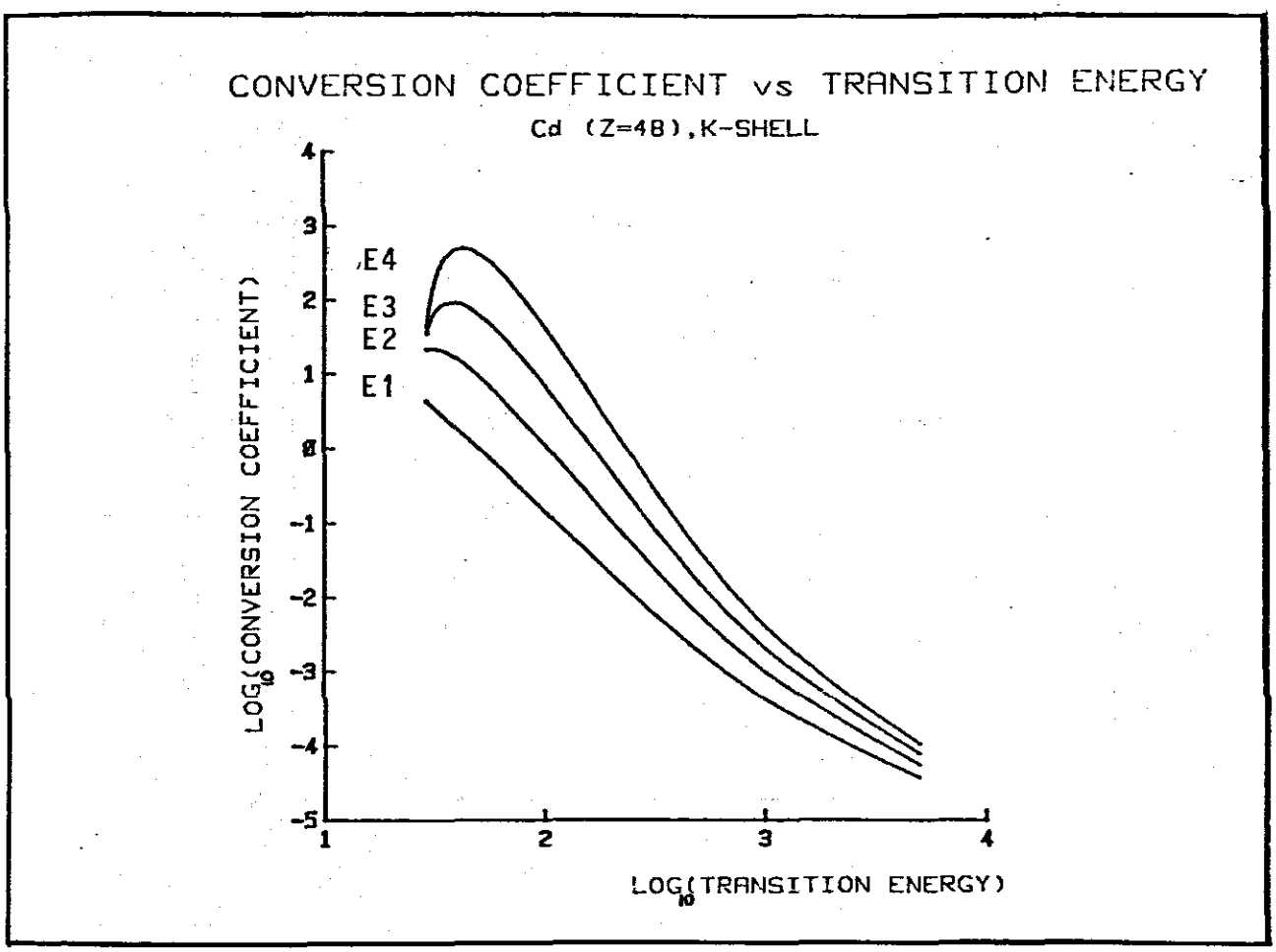

FIGURE 7: Graph of K-shell conversion coefficient for E(L) transitions vs transition energy in keV for Z=48. The graphs were obtained by interpolating tabled values (Rös 78). Note the anomalities at threshold energies for higher multipole order transitions.

iv) Atomic number

In the eqs. 3.1.5 and 3.1.6 it was indicated that the conversion coefficients increase with Z^3 where Z is the atomic number. Internal conversion measurements as a method of studying nuclear states, become relatively more useful, compared to gamma radiation measurements, for nuclei of higher atomic numbers.

FIGURE 8

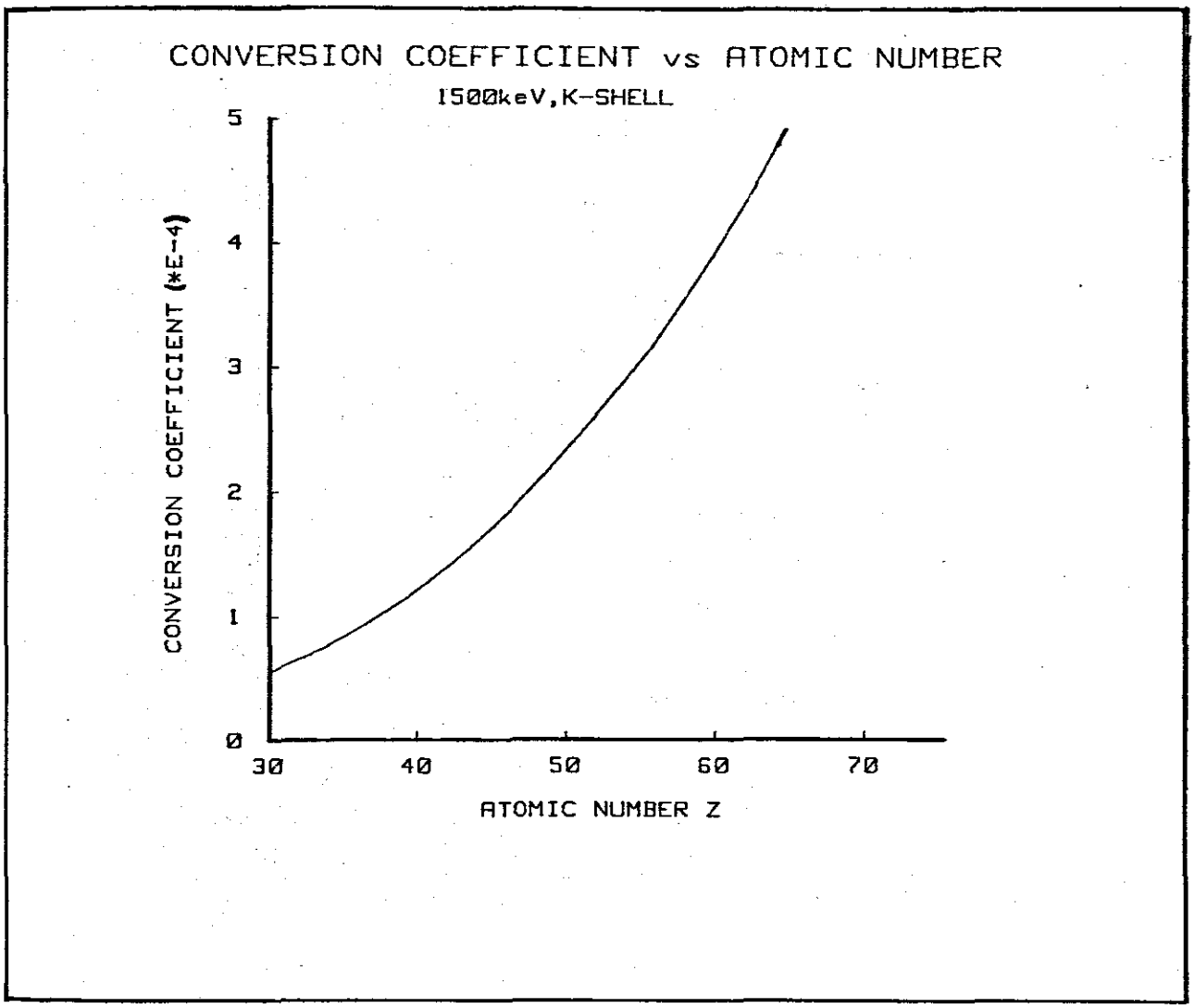

FIGURE 8: Graph of E1 K-shell conversion coefficient vs Z for 1500 keV transitions. The graphs were obtained by interpolating tabled values (Rös 78).

v) Atomic shell

In the point nucleus approximation of conversion coefficients, it becomes apparent that the coefficients strongly depend on the atomic shell or subshell from which the electron is emitted. Theoretically $\alpha_K > \alpha_L > \alpha_M$ and $\beta_K > \beta_L > \beta_M$, but the exact dependence proves to be different from $1/n^3$, as is predicted in this approximation, but nevertheless gives a qualitative indication of the dependence of these coefficients on the wave function of the bound electron.

FIGURE 9

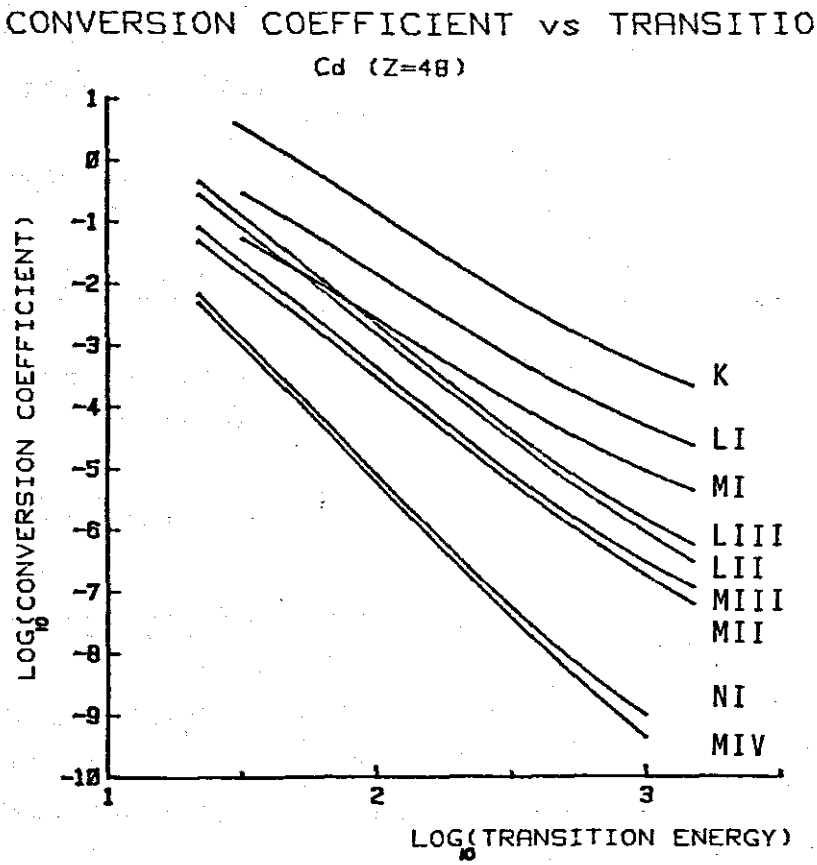

FIGURE 9 Graph of E1 conversion coefficient vs energy in keV for various subshells. Z=48. The graphs were obtained by interpolating tabled values. (Rös 78).

It is often convenient to investigate the ratio of internal conversion coefficients of various shells, or subshells. These ratios can be used for spin and parity assignments, especially for heavy elements (high Z) and low energy. The method is effective only for L > 1. Detailed descriptions of such experiments are given elsewhere. (Ham 75).

vi) Selection Rules

For internal conversion the same selection rules apply as for gamma radiation. There is however the additional possibility of L = 0 transitions between states of equal spin. This matter is discussed in section 3.2.

vii)Other factors

a) Screening

Although atomic screening was not included in this discussion, it is neccessary to take it into account, especially for L, M, N shells, where the effect of screening becomes significant.

b) Nuclear Structure

In the point nucleus approximation given here, the internal conversion coefficients are independent of nuclear structure. With the finite size of the nucleus taken into account, this is not the case and nuclear structure plays an important role as will be discussed in the next paragraphs. The effect of nuclear structure is also essential in explaining the E0 transitions.

E. Tabulated internal conversion coefficients

For a comparison with experimental results a crude estimate such as has been presented in the preceeding paragraphs is not sufficient. Detailed theory of internal conversion has been reviewed by several authors elsewhere. (HSe 68, Ros 68, Pau 75).

The emission of internal-conversion electrons in a nuclear transition is influenced in two ways by the finite size of the nucleus.

1) The finite size of the nuclear charge distribution has an important effect on the electron wave function which determine the emission probabilities. (See eq. 3.1.3.)

2) The finite size of the nucleus leads to internal conversion occurring within the nucleus (penetration effect).

In cases on hindered nuclear transitions the penetration effect becomes an important internal electron-emission mechanism. (HSe 68, Chu 60, Gre 58, Chu 56). These are referred to as the static and dynamic nuclear effects respectively.

When taking into account the static effect, i.e. the atomic electron is considered as always being outside the nucleus, the nuclear matrix elements in the expressions for the transition probabilities of gamma-transitions and conversion electron transitions are equal, and cancel when the conversion coefficient is calculated, as was the case in the estimate of the conversion coefficient discussed in the preceeding paragaphs. Hence internal-conversion coefficient is essentially nuclear structure independent. However, experimental data indicate that the dynamic effects are especially important for some heavy nuclei (Gre 58) for E1 and M1 transitions mainly, and of course for E0 transitions which are entirely caused by penetration effects. (Pau 75, Ros 68).

These nuclear structure dependent contributions to internal conversion were first noted by Church and Weneser, (CWe 56) in explaining E0 transitios. Soon afterwards the same authors (Chu 56) and others (Gre 58) introduced modifications to the theory of the interactions involved in internal conversion, in order to accomodate anomalities in some theoretical and experimental conversion coefficients. The conversion coefficients presented in tables (Dra 69, Hag 68, Rös 78, Dra 75, Ban 78, Dra 71, Tru 72) were calculated including finite

nuclear size but without taking account of penetration effects. Atomic screening was taken into account and relativistic second order perturbation calcultions were performed. In this work the latest available tables of Rösel et al (Rös 78) were used. Interpolation of the tabulated values was made using cubic splines, which according to Rösel et al (Rös 78) gives "an error within the rounding error of the three relevant digits". Some graphs of such interpolated values are presended in fig. 10 - 12.

FIGURE 10

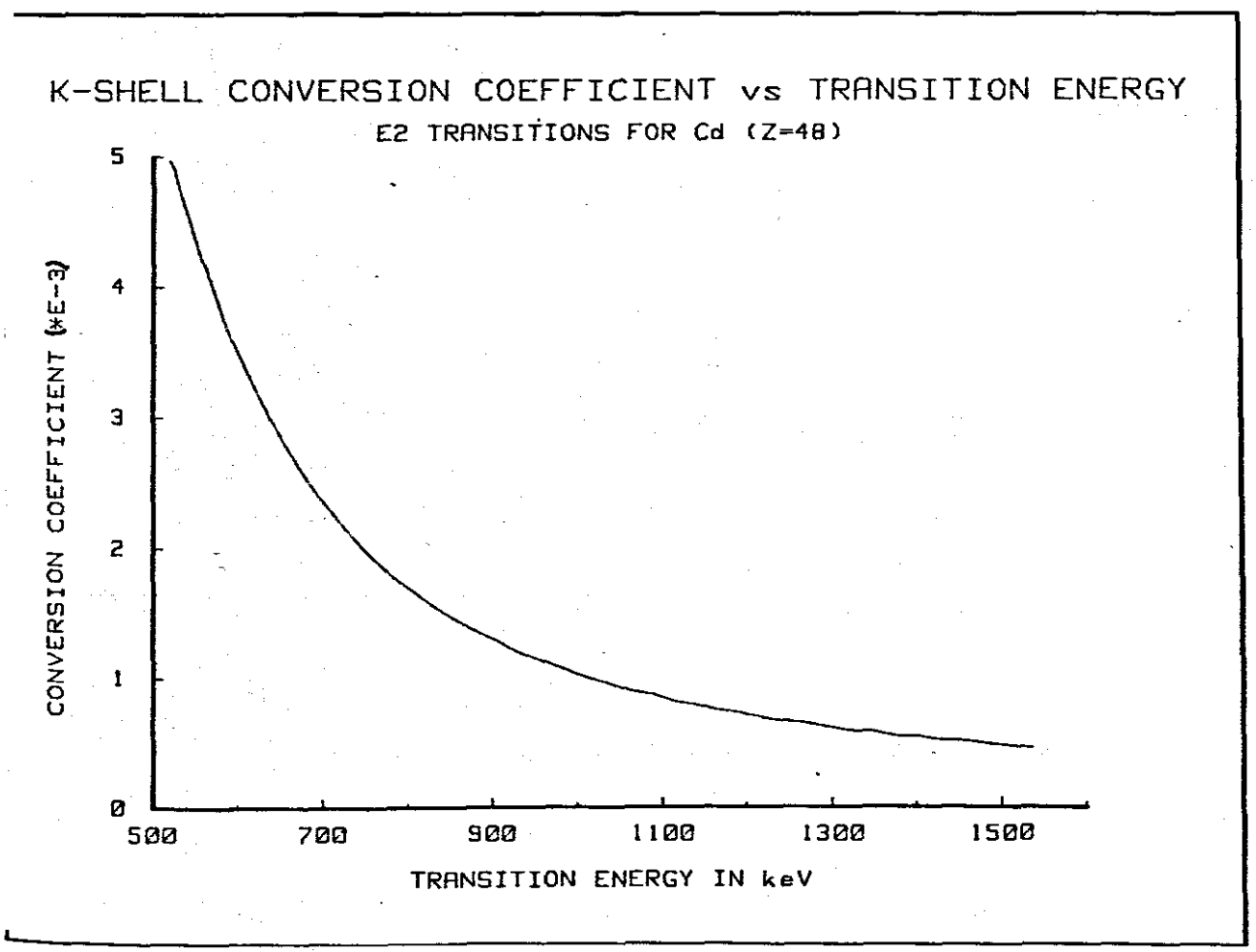

FIGURE 10: The E2 conversion coefficient vs transition energy in keV for Cd (Z = 48) for K-shell electrons. The graphs were obtained by interpolating tabled values (Rös 78).

FIGURE 11

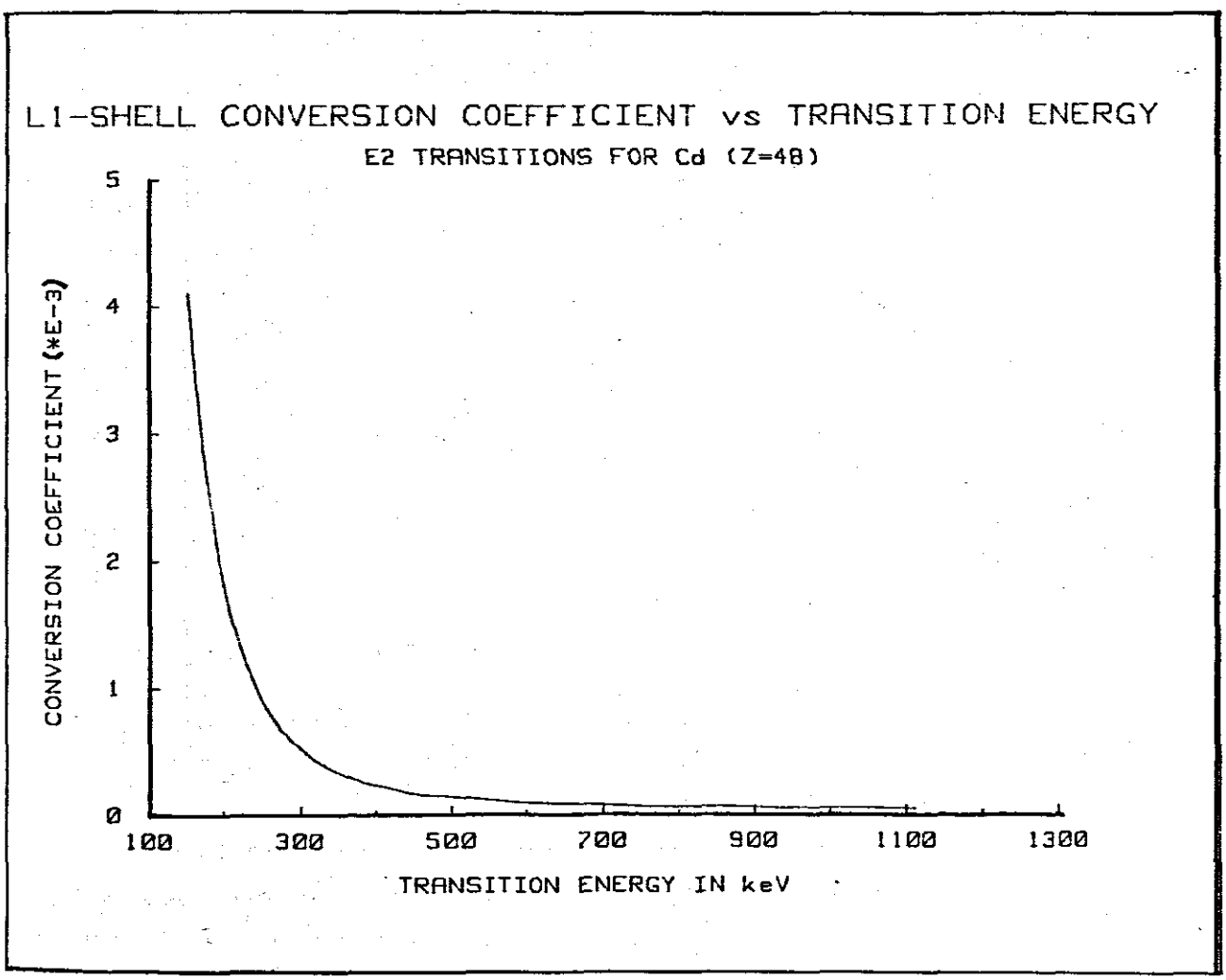

FIGURE 11: The E2 conversion coefficient vs transition energy for Cd (Z = 48) for the total LI-shell. The graphs were obtained by interpolating tabled values (Rös 78).

FIGURE 12

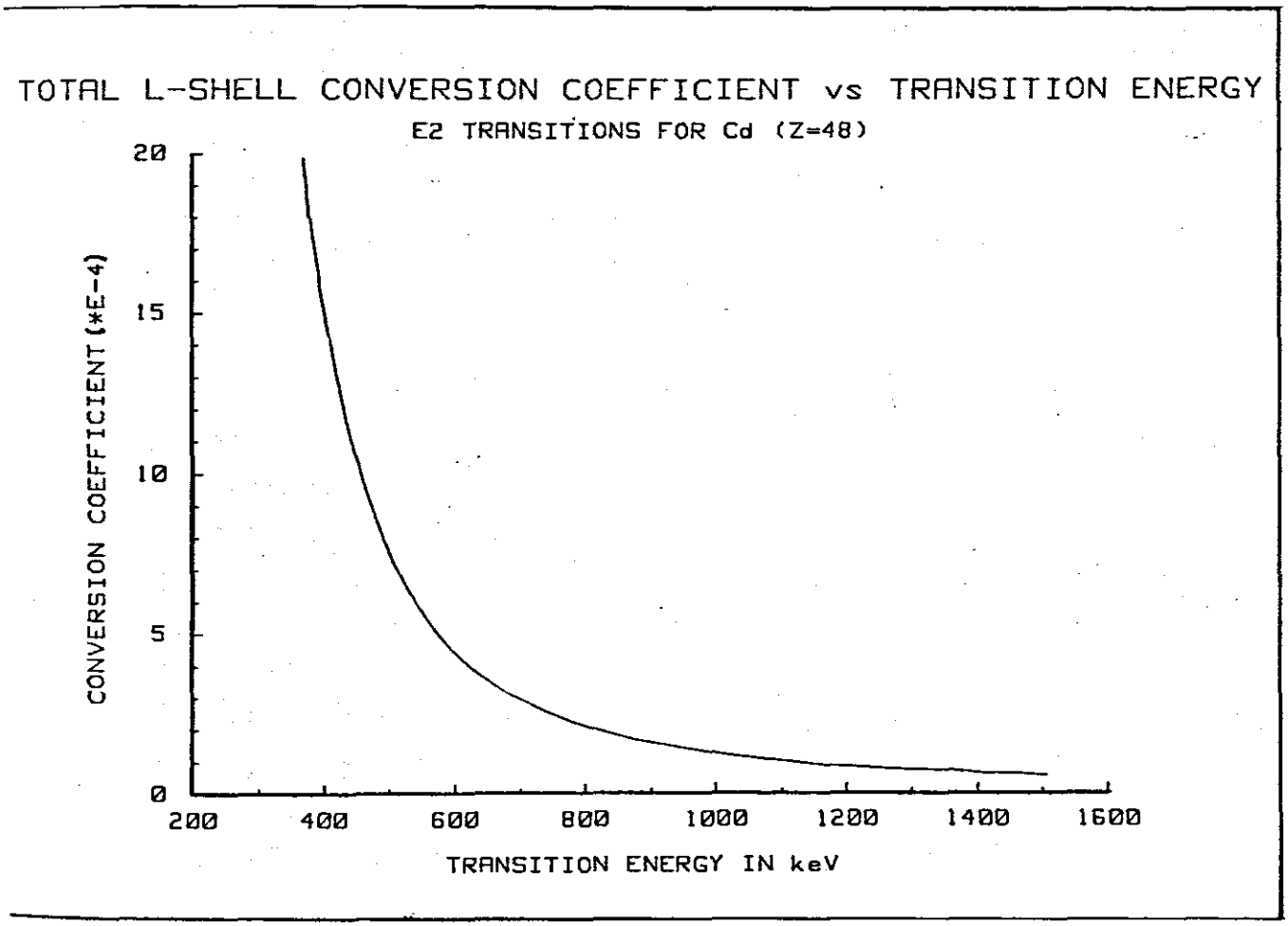

FIGURE 12: The E2 conversion coefficient vs transition energy for Cd (Z = 48) for the total L-shell. The graphs were obtained by interpolating tabled values (Rös 78).

In cases where penetration effects are important, information in addition to the conversion coefficients and directional particle parameters is required for electron-emission analysis. In such cases the internal- conversion coefficients are written as

$$\alpha = \alpha_0 (1 + A_1\lambda_1 + A_2\lambda_1^2 + A_3\lambda_2 + A_4\lambda_2^2 + A_5\lambda_1\lambda_2 + A_6\lambda_3 + A_7\lambda_1\lambda_3)$$

...3.1.7

for pure electric multipole radiation, where α_0 is the tabulated conversion coefficient, λ_1, are ratios of nuclear electromagnetic matrix elements (Hag 68, Pau 75) and A_i are penetration coefficients for penetration effects, which can be found in tables eg. Hager and Seltzer (Hag 69). Similarly for magnetic multipole radiation $\beta = \beta_0(1 + \beta_1\lambda + \beta_2\lambda^2)$, using the notation of Hager and Seltzer (Hag 68, Hag 69, Kri 73). The relationship between notations used by various authors for penetration coefficients can be found in Hager and Seltzer (Hag 69) and Pauli et al. (Pau 75.) Theoretical background on this work can be found elsewhere. (Pau 75, Rös 68, Chu 60).

With the availability of accurate non penetration conversion coefficients, it is therefore now possible to determine the peneteration matrix elements λ, by experimental determination of the conversion coefficient in cases where penetration is noticable. Clearly these penetration effects are mostly noticable for K-shell conversion. Such experimental work is discussed by Kripic et al. (Kri 73) and others (Gia 82, GPe 82, Hag 66, Lom 66).

In pure M1 transitions the process is simple since the conversion coefficient depends on λ and λ^2. However for E1 transitions the situation is more complicated, and additional data is required from angular distribution experiments (see section 3.4). Such experiments are discussed by Hager and Seltzer

(HSe 66) Very often M1 + E2 mixtures are used to determine λ. (Gia 82, GPe 82, Fuj 81). The K-conversion coefficient of such a M1 and E2 mixed transition, when penetration effects are taken into account for the M1 component but not for the E2 component, is given by

$$\alpha_K(\text{exp}) = \frac{\alpha_K(M1)[1+b_1\lambda + b_2\lambda^2] + \delta^2\alpha_K(E2)}{1 + \delta^2} \qquad \ldots 3.1.8$$

ref. (Hag 69)
where $\alpha_K(\text{exp})$ is the experimentally determined conversion coefficient, $\alpha_K(M1)$ and $\alpha_K(E2)$ the theoretical conversion coefficients without penetration effect, b_1 and b_2 are tabulated particle parameters from Hager and Seltzer (Hag 69) and δ the gamma mixing ratio. The results of such an experiment for ^{107}Cd is shown in Figure 13, with δ^2 known from other work. (Gia 82)

FIGURE 13

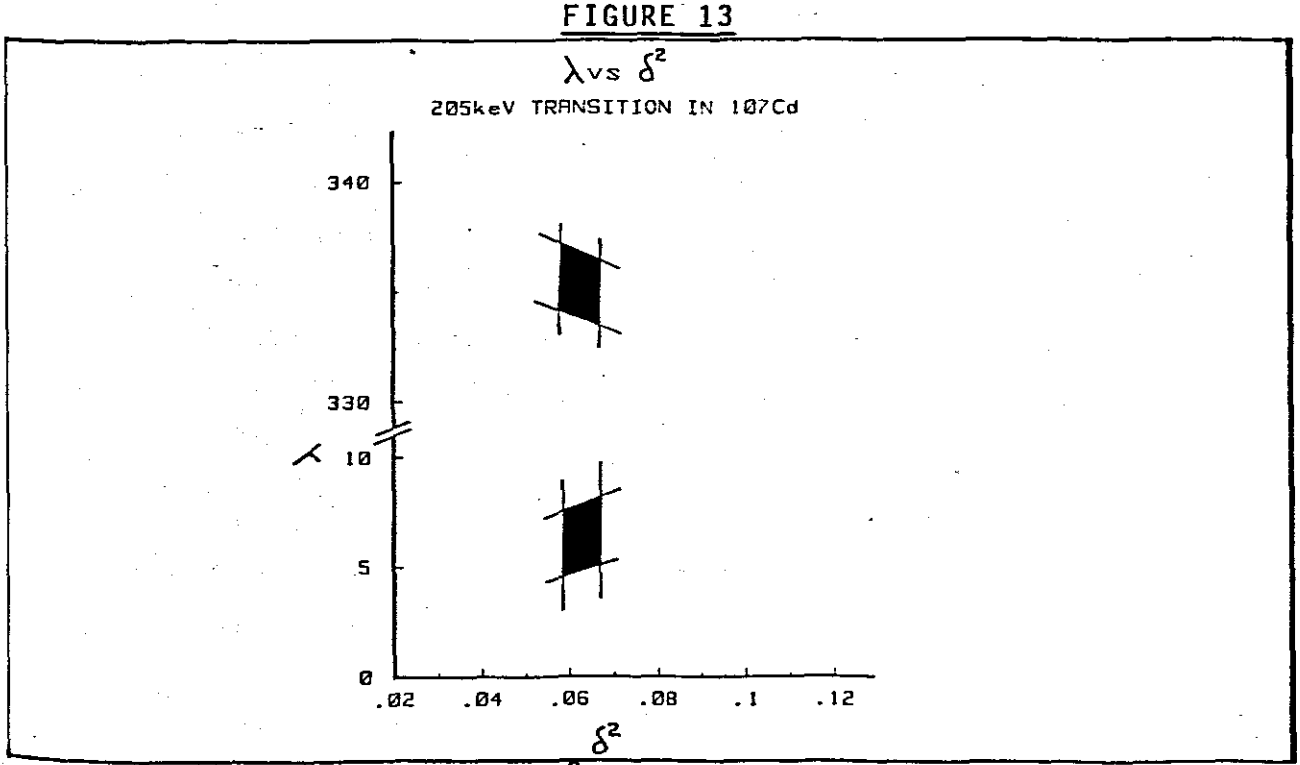

FIGURE 13 A plot λ versus δ^2 for the 205 keV transition in ^{107}Cd for values of α_k (205 keV) differing by one standard deviation either way from the measured value. The figure was copied from ref. (Gia 82) to serve as an illustration.

F Penetration effect and directional distribution

Penetration effects affect the directional distribution of conversion electrons. This matter is discussed in Section 3.4.

3.2 Electric monopole transitions

A General

In the previous paragraphs it was pointed out that penetration of the nucleus resulted in the fact that the rate of internal conversion is not determined completely by the gamma-ray emission rate. Nuclear matrix elements for internal conversion appear as a result of penetration of the charge and current distributions of the nucleus and hence carry distinctive information about the nuclear structure. The most striking penetration effect is the fact that E0 internal conversion takes place.

As stated before, monopole transitions are totally forbidden for gamma-emission since a photon must carry away at least 1ħ in angular momentum. Hence low-energy electric-monopole E0 transition proceed solely by internal conversion with zero units of angular momentum transferred to the ejected electron. For energies greater than $2mc^2$ monopole pair production is also possible.

However it should be noted that in the case of M0 "transitions" the matrix elements $\langle j_f \left| M(M0) \right| j_i \rangle$ vanish. (Bor 64, Pau 75).

Two situations lead to E0 internal conversion:

a) Transitions between $j_i^{\pm} = 0$ and $j_f^{\pm} = 0$. In this case E0 internal conversion is the only possible internal conversion process, and single photon emission is not allowed; and

b) Transitions between $j_i^{\pm} = j_f^{\pm} \neq 0$. In the latter case it was pointed out by Church and Weneser (Chu 55, CWe 56) that E0 internal conversion strongly competes with E2 and M1, gamma emission as well as internal conversion. This is demonstrated by the figure taken from Church and Weneser (CWe 56).

FIGURE 14

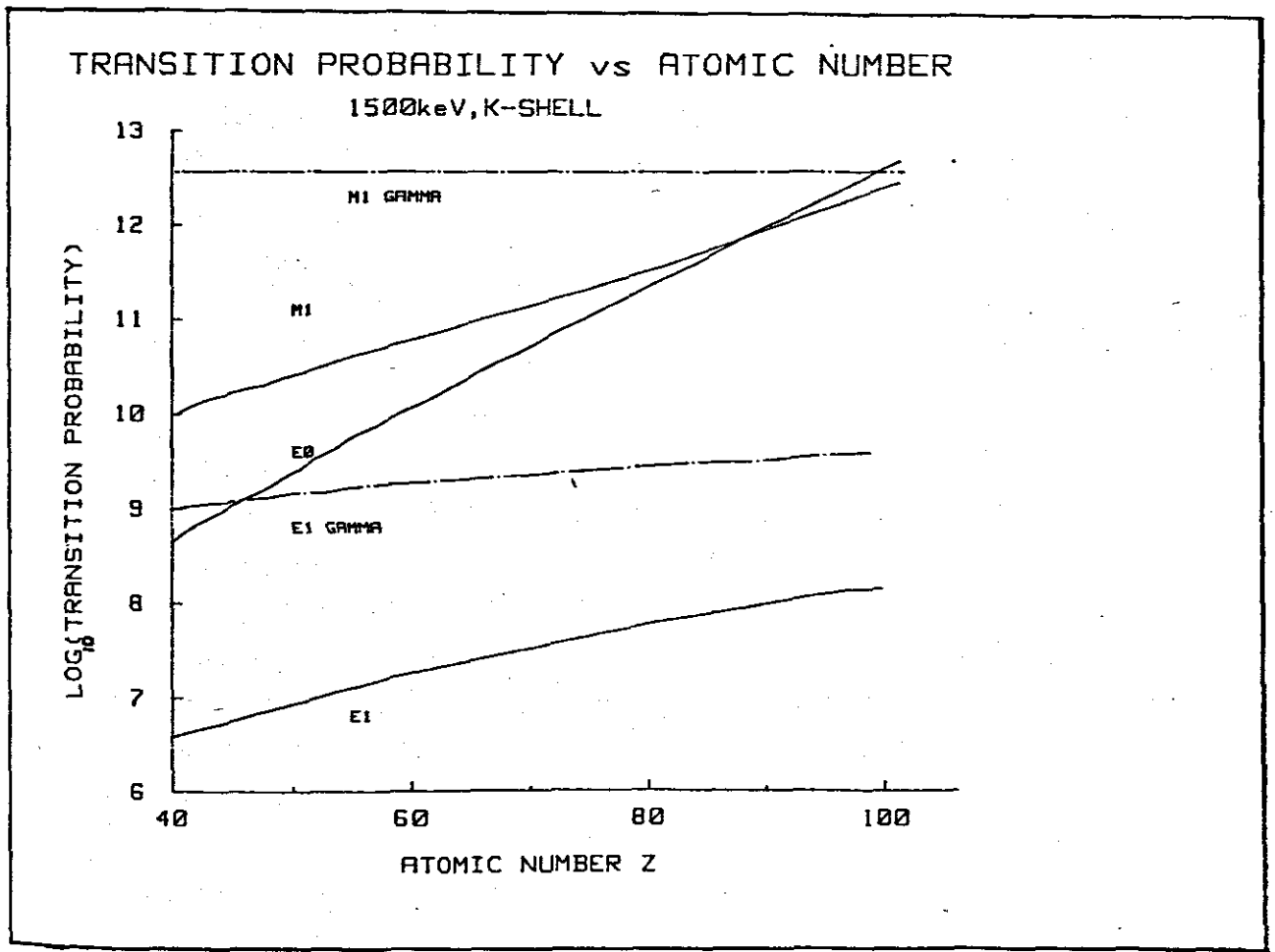

FIGURE 14: Transition probability for electric-monopole (E0) conversion in the K-shell as a function of the atomic number Z for a transition energy of one mc^2. These results have been derived by assuming ρ=1. The analogous Weisskopf estimates for the M1 and E2 gamma-ray and K-shell conversion probabilities, are included for comparison. The figure was taken from ref. (CWe 56) to serve as an illustration of the relative magnitudes of the transition probabilities.

Examples of $0^+ \rightarrow 0^+$ E0 transitions as well as $j_i^{\pm} \rightarrow j_f^{\pm}$ E0 transitions are numerous. However only one example of $0^- \rightarrow 0^-$ E0 transition is known, being an E0 transition in ^{212}Bi (176 keV). ref.(Bor 64, Ald 72). The transition probability $T_K(E0)$ for E0 internal conversion is custumarily written as

$$T_K(E0) = \Omega_K \rho^2(E0) \qquad ...3.2.1$$

(Chu 55, Bor 64, Lan 82)
where Ω_K is the so called electronic factor (similarly one can define $T_L = \Omega_L \rho$ etc.) and $\rho(E0)$ nuclear strength parameter, containing the nuclear matrix elements. The electronic factor Ω can be calculated if the energy of the transition is known and the electronic wave function is known.

$$\Omega = 8\pi\alpha k \frac{mc^2}{\hbar} A(E0) s^{-1} \qquad ...3.2.2$$

(Voi 76, Ald 72, Pau 75, Hag 69)
where $\alpha = 1/137$ spectroscopic factor and k is energy in mc^2 units and A(E0) are coefficients calculated for each atom and each shell and tabulated by Hager and Selzer, (Hag 69) and can also be found elsewhere. (Bel 70). The nuclear strength parameter, $\rho(E0)$, depends on the nuclear structure and is hence model dependent and the quantity to be determined experimentally in order to test particular nuclear models.

$$\rho(E0) = \langle j_f \| M(E0) \| j_i \rangle \qquad ...3.2.3$$

where M(E0) is the electric monopole operator as defined by Lange et al (Lan 82). Several such theoretical predictions of ρ for various types of nuclear models have been presented. (Lan 82, Ald 72, Pau 75, Tak 83, Dav 66). A rough estimate of $T_K(E0)$ for $0^+ \rightarrow 0^+$ has been predicted by Blatt and Weisskopf (Bla 79) for a single particle transition, which can give a qualitative indication of the value of $T_K(E0)$ and its dependence on atomic number Z and transition energy.

$$T_K(E0) = 0{,}5\ Z^3 (E/mc^2)^{\frac{1}{2}} \times 10^4\ s^{-1} \qquad ...3.2.4$$

where $E = E_i - E_f - B_K = \frac{\hbar^2 k^2}{2m}$ is the energy of the ejected electron with E_i and E_f and the initial and final nuclear energies respectively and B_K the atomic binding energy of the K-shell electron.

FIGURE 15

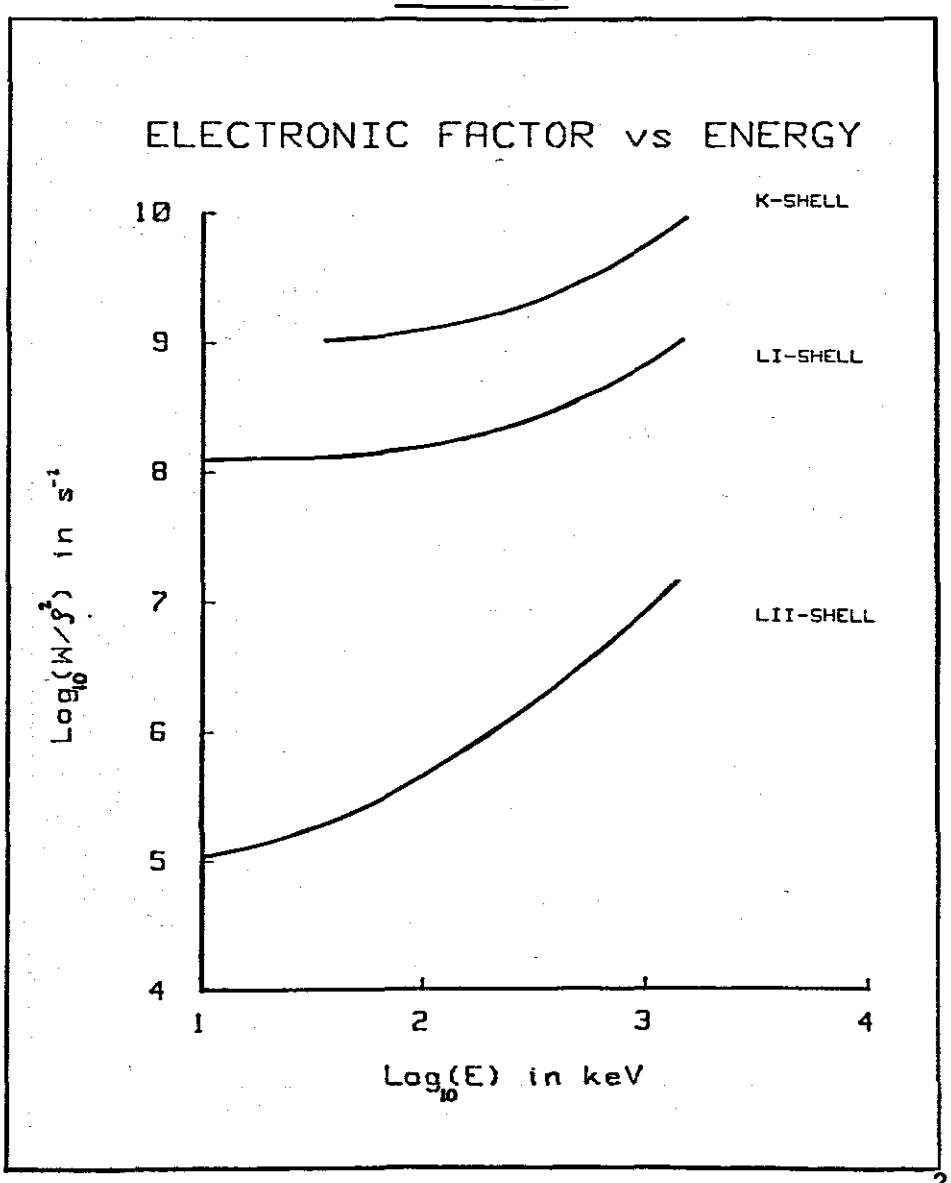

FIGURE 15: The reduced E0 transition probability $T(E0)/\rho^2$ in s^{-1} vs transition energy in keV for Z = 50 for subshells K, L1 and L2. The graphs were obtained by interpolating tabled values. ref. (Hag 69)

From this it can be seen that $T_K(E0)$ increases rapidly with Z and hence becomes increasingly important for heavy nuclei, where it can become the main contribution to nuclear deexcitation in the event of a $j_i = j_f \neq 0$ transition as is indicated by figure 14. Although $T_K(E0)$ increases with energy it should be noted that for gamma-radiation T_γ increases rapidly with energy eg. $T_\gamma(EL) \sim \omega^{2L+1}$ (see eq. 2.3.4), hence the domination of E0 internal conversion over gamma-radiation would be confined to lower energy transitions. Using the tables of Hager and Seltzer (Hag 69) values of $T_K(E0)/\rho^2(E0)$ can be plotted. This is illustrated in fig. 16.

FIGURE 16

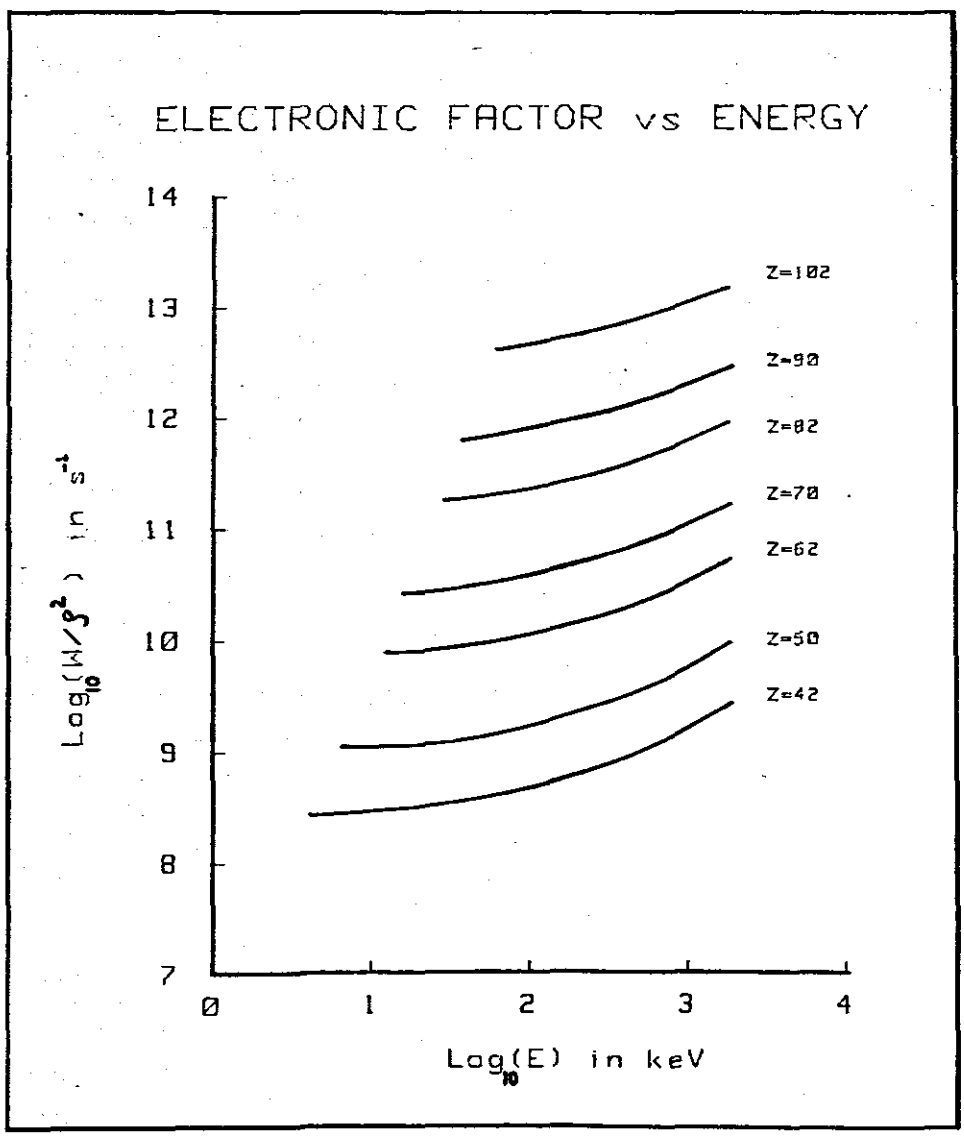

FIGURE 16: The reduced E0 transition probability $T(E0)/\rho^2$ in s^{-1} vs transition energy in keV for K-shell for various atomic numbers Z. The graphs were obtained by interpolating tabled values (Hag 69).

In experimental work the ratio

$$q^2 = \frac{T_K(E0)}{T_K(E2)} = \frac{T_K(E0)}{T_\gamma(E2)\,\alpha_K} \qquad \ldots 3.2.5$$

(Lan 82, Ald 72)

is measured to determine the value of ρ since it follows:

$$q^2 = \frac{\Omega_K\ \rho^2(E0)}{T_\gamma(E2)\ \alpha_K} \qquad \ldots 3.2.6$$

$$\text{and hence } \rho(E0) = q \sqrt{\frac{\alpha_K\ T_\gamma(E2)}{\Omega_K}} \qquad \ldots 3.2.7$$

$$q = \sqrt{\frac{\alpha_K\ B(E2)\ 1{,}221\times10^9\ E_\gamma^{\,5}}{\Omega_K}}$$

where Ω_K is the electronic factor for K-shell conversion, α_K is the E2 K-shell conversion coefficient, and $T_\gamma(E2) = 1{,}221 \times 10^{13}\ E_\gamma^5\ B(E2, j_i \to j_f)$ with E_γ in MeV.

The value of $B(E2, j_i \to j_f)$ can be determined by Coulomb excitation experiments. (Ald 72).

FIGURE 17

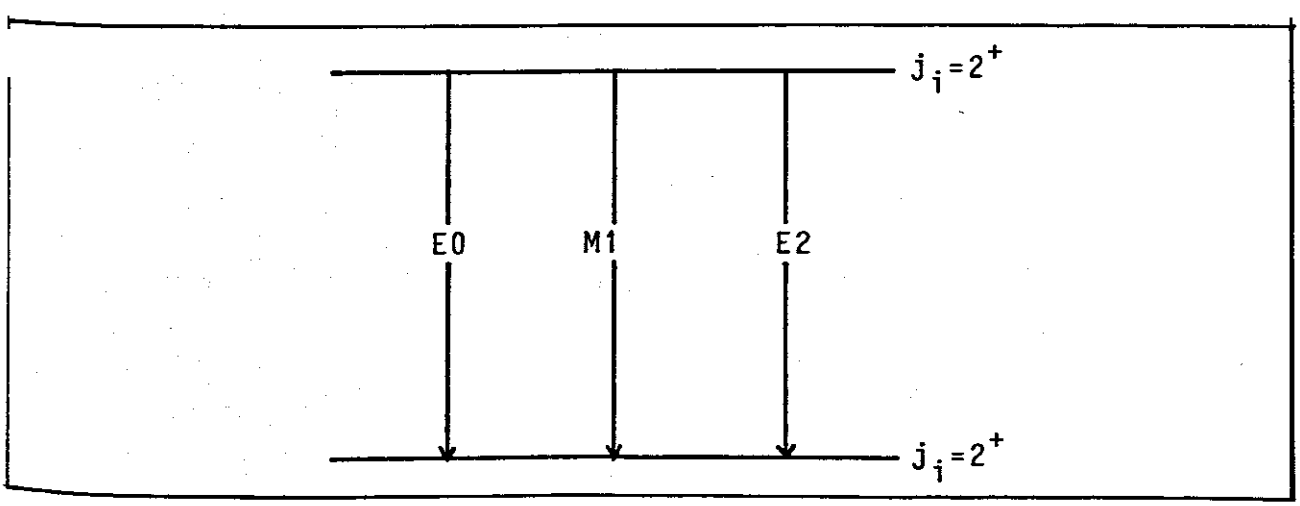

FIGURE 17: A schematic illustration of deexiation where E0-M1-E2 mixing is possible. The M1 and E2 transitions proceed via gamma-radiation and internal conversion.

In the event of a transition $j_i \rightarrow j_f$, $j_i = j_f \neq 0$, where it is possible to get EO, E2, M1 admixtures, the ratio q^2 is defined as:

$$q^2 = \frac{T_K(EO)}{T_K(E2)} = \frac{I_K(EO)}{I_K(E2)}$$ which is the ratio of

the intensities of K-shell conversion electrons of the competing EO and E2 transitions.

$$\text{Hence } q^2 = \frac{I_K(TOT) - I_K(E2) - I_K(M1)}{I_K(E2)}$$

$$= \frac{I_K(TOT)}{I_K(E2)} - 1 - \frac{I_K(M1)}{I_K(E2)}$$

$$= \frac{\alpha_K(EXP)\ I_\gamma(TOT)}{I_K(E2)} -1- \frac{\alpha_K(M1)\ I_\gamma(M1)}{\alpha_K(E2)\ I_\gamma(E2)}$$

$$= \frac{\alpha_K(EXP)[I_\gamma(E2)+I_\gamma(M1)]}{I_\gamma(E2)\ \alpha_K(E2)} -1- \frac{\alpha_K(M1)}{\delta^2 \alpha_K(E2)}$$

$$= \alpha_K(EXP)\ [\frac{1}{\alpha_K(E2)} + \frac{1}{\delta^2 \alpha_K(E2)}] -1- \frac{\alpha_K(M1)}{\delta^2 \alpha_K(E2)}$$

Multiplying by $\delta^2 \alpha_K(E2)$, then

$$\delta^2 q^2 \alpha_K(E2) = \alpha_K(EXP)[\delta^2 + 1] - \delta^2 \alpha_K(E2) - \alpha_K(M1)$$

$$\therefore \alpha_K(EXP) = \frac{1}{1+\delta^2} [\delta^2(1+q^2)\ \alpha_K(E2) + \alpha_K(M1)] \qquad ...3.2.8$$

ref. (Ald 72)

The penetration effect of M1 conversion is neglected and $\alpha_K(E2)$ and $\alpha_K(M1)$ values from the tables are used. If the total internal conversion coefficient $\alpha_K(EXP)$ is determined experimentally, the value of q^2 can be obtained.

Should the M1 penetration effect however not be negligible, directional distribution or correlations experiments have to be performed to get sufficient information about λ, the M1 penetration parameter. (Ald 72) (see section 3.4). Tabulated values of $\alpha_K(M1)$ could then be corrected to include penetration effects.

B The quantity q^2 in $0^+ \rightarrow 0^+$ transitions

In the case of $0^+ \rightarrow 0^+$ transitions only E0 transitions are allowed. It is convenient to define a similar ratio: (Lan 82).

$$q^2 = \frac{T_K(E0, 0^+ \rightarrow 0^+)}{T_K(E2, 0^+ \rightarrow 2^+)} \qquad \ldots 3.2.9$$

An example of such a situation is illustrated in Figure 18.

FIGURE 18

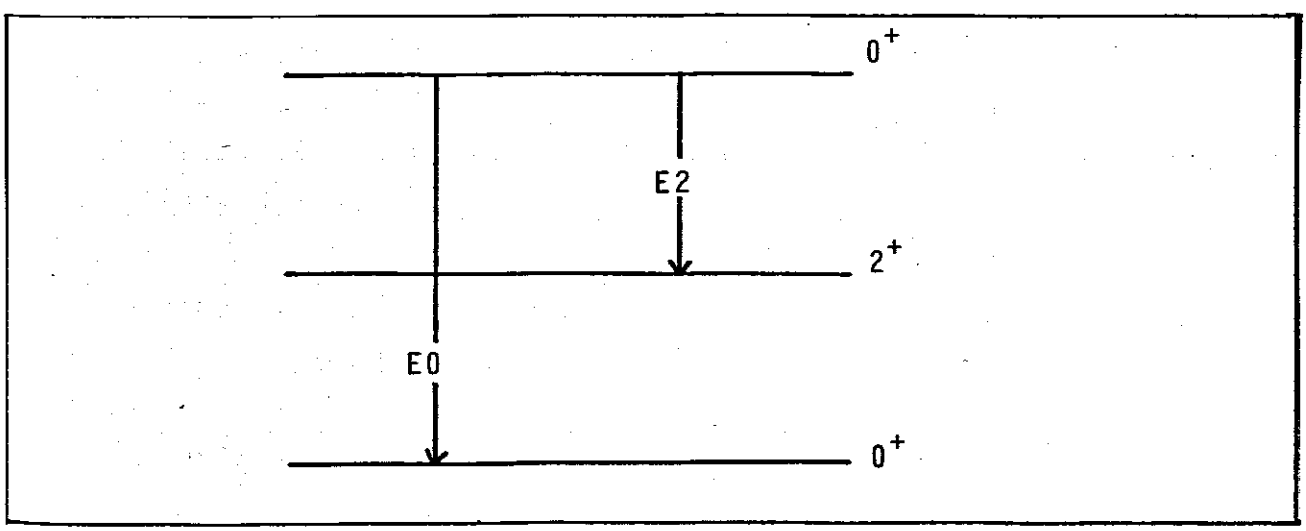

FIGURE 18: The internal conversion electron transitions relevant to equation 3.2.9 for ^{112}Cd are indicated.

This makes measurement of q^2 very easy since,

a) All the conversion electrons from the $0^+ \rightarrow 0^+$ transition are E0 electrons, and the intensity $I_K(E0)$ can be obtained directly.

b) All the conversion electrons from the $0^+ \rightarrow 2^+$ transition are E2 electrons, and the intensity $I_K(E2)$ can be obtained directly.

Clearly eq's. 3.2.6 and 3.2.7 still hold and values of $\rho(E0)$ can be obtained. It is also sometimes useful for comparison with theory to introduce the dimensionless ratio

$$X(E0/E2) = \frac{B(E0, j_i \rightarrow j_f)}{B(E2, j_i \rightarrow j_f')} \qquad \ldots 3.2.10$$

where $B(E0) = e^2 R^4 \rho^2(E0)$ the so called E0 nuclear transition probability, with

R = nuclear radius
e = 1,6 x 10^{-19} C, and
B(E2) is the reduced E2 transition probability defined earlier (eq. 2.1.4).

$$B(E2) = \frac{T_\gamma(E2)}{1{,}221 \times 10^9 \; E_\gamma^5}$$

with E_γ in MeV, the gamma energy of the E2 transition.

$$\text{and hence } X(E0/E2) = \frac{e^2 R^4 \rho^2(E0) \; 1{,}221 \times 10^9 \; E_\gamma^5}{T_\gamma(E2)}$$

$$\text{but } \rho^2(E0) = \frac{q^2\ \alpha_K(E2)T_\gamma(E2)}{\Omega_K}$$

$$\text{hence } X(E0/E2) = \frac{e^2R^4q^2\alpha_K(E2)\ 1{,}221 \times 10^9 E_\gamma^5}{\Omega_K}$$

$$= 2{,}53 \times 10^9\ A^{4/3}q^2\ \alpha_K(E2)\ \frac{E_\gamma^5}{\Omega_K} \qquad \ldots 3.2.11$$

ref. (Ald 72, Dav 66, Kum 75)
using $R = 1{,}2\ A^{1/3}$ [fm]
and recalling that the units of B(E2) are e^2fm^4.

Some ratios $\rho(E0)$ and $X(E0/E2)$ are presented in Alduschekenkov and Vionova (Ald 72) for most even-even nuclei. Theoretical values for some even-even nuclei are also presented elsewhere. (Dav 66, Kum 75, Tak 83) Recently (Kuz 82) it was pointed out that in cases where E0 conversion is retarded, allowance for intermediate electron-nuclear states must be made in the theoretical calculation since in such cases the correction can be several percent.

3.3 Internal Pair Production

A General

Internal pair production is an alternative mode of nuclear deexcitation competing with gamma-radiation and internal conversion for transitions of energy $E > 2mc^2$, where m is electron rest mass. (Ros 35, Ros 49, Tho 40, Bor 64). It is useful to define an internal pair production coefficient in similar fashion as internal conversion. (Bor 64, Wil 68, Sof 81)

$$\alpha_\pi = \frac{I_{e^+e^-}}{I_\gamma} \qquad \ldots 3.3.1$$

where I_γ is the intensity of a particular multipole transition; and $I_{e^+e^-}$ is the corresponding intensity of electron-positron pairs. Unlike internal conversion the internal pair production process is not dependent on the atomic shells, and also the electrons or positrons are obviously not mono-energetic. However, α_π does depend on multipolarity of the transition and can be used for determining spin and parity of nuclear states. (Sch 78, War 65). Calculated values of these coefficients are available (Sch 79) and figures 19 and 20 give interpolations of these values.

FIGURES 19

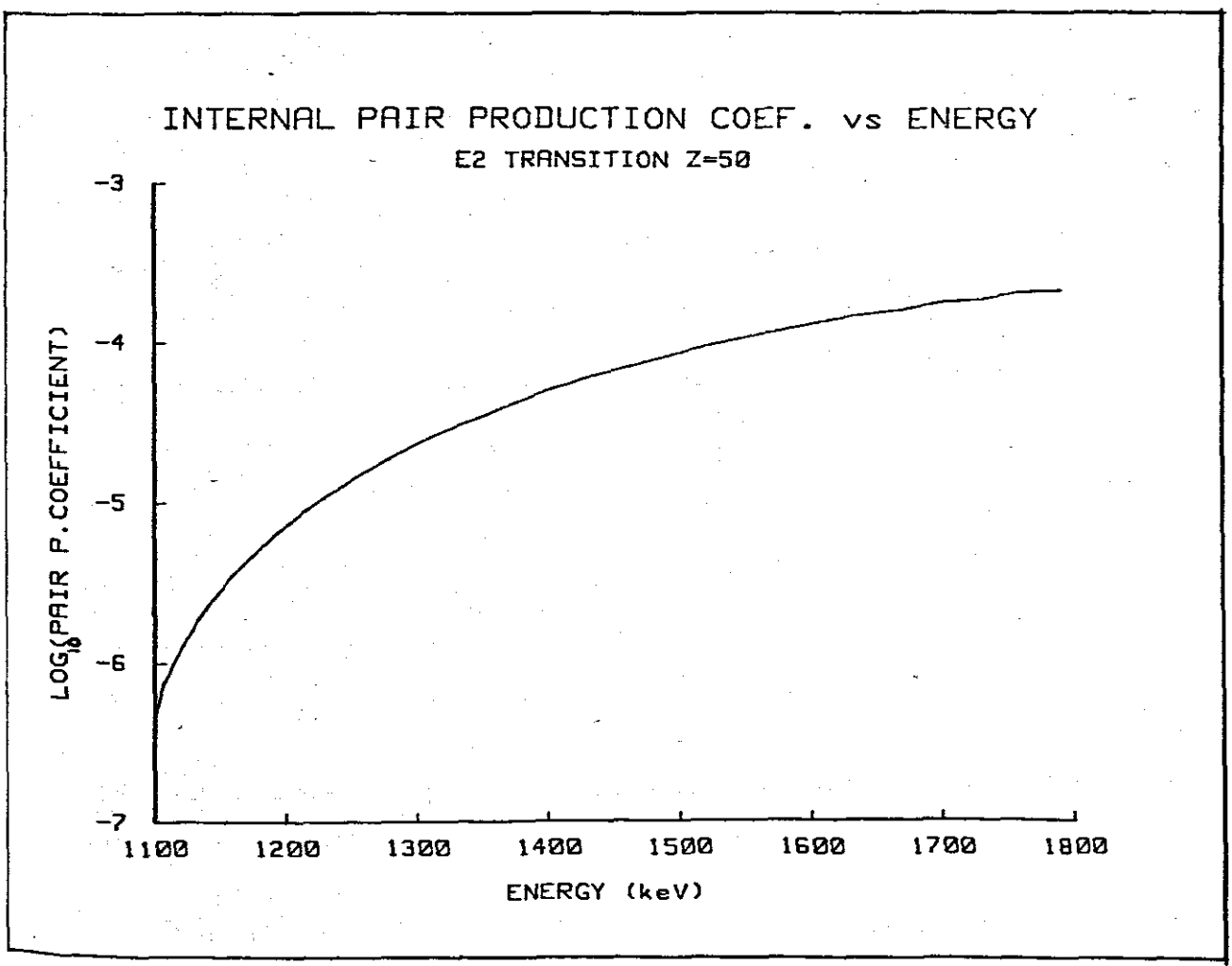

FIGURE 19: Internal pair production coefficient for Z = 50 vs transition energy in keV for E2 transitions.

FIGURE 20

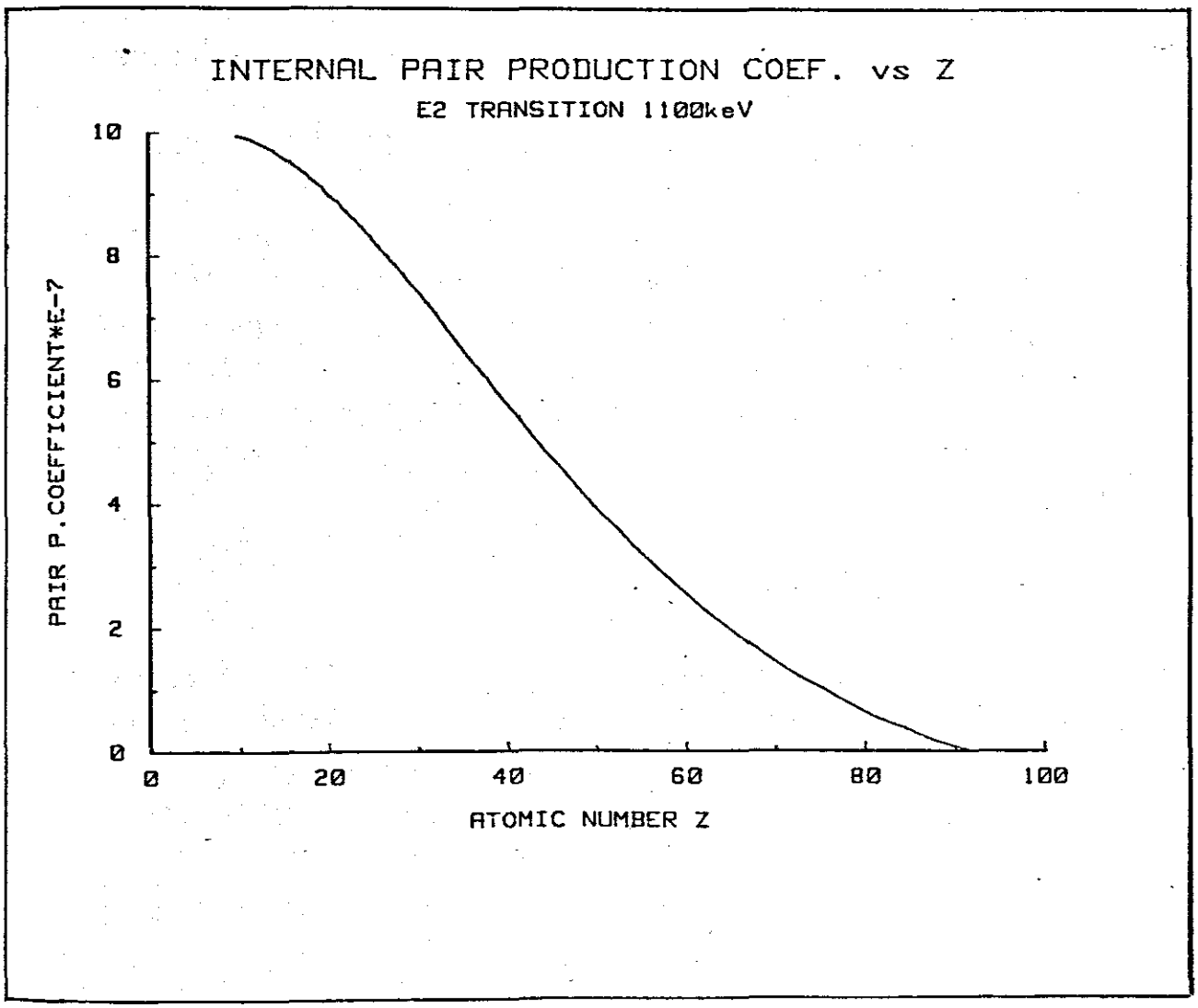

FIGURE 20: Internal pair production coefficient for 1100 keV E2 transition vs atomic number Z.

From these figures it is apparent that internal pair production is important at low Z and very high energies, where it can compete favourably with gamma-radiation and internal conversion.

B EO transitions

Of special interest are EO transitions $0^+ \rightarrow 0^+$, since except for EO internal conversion, EO internal pair production is the only mode of deexcitation. The total EO internal-pair transition probability $\omega_\pi(EO)$ is defined as

$$\omega_\pi(EO) = \rho^2 \Omega_\pi(EO)$$

ref. (Bor 64)
in analogy to the internal conversion probability where ρ is the monopole matrix element, $\Omega_\pi(EO)$ is the electronic factor for internal pair production. Detailed theory is discussed elsewhere (Bor 64, Sof 81, Wil 70, Wil 69). Soff et al (Sof 81) defined a ratio

$$\eta = \frac{P_{e^+e^-}}{P_e} \qquad \ldots 3.3.3$$

which is the ratio of the probability of electron positron pair production $P_{e^+e^-}$ to the probability of internal conversion P_e for EO transitions. Figures 21 and 22 show the results of the theoretical values of η. (Sof. 81).

FIGURE 21

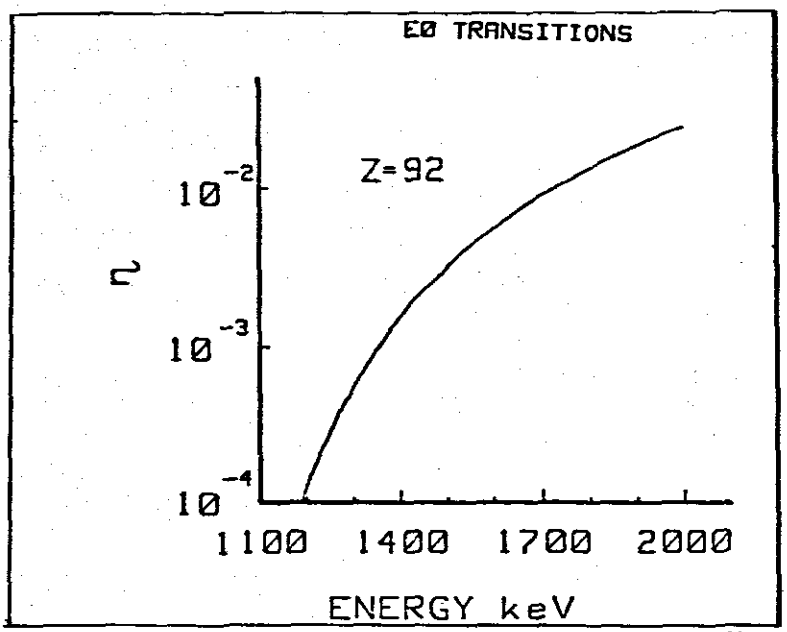

FIGURE 21: The ratio η vs transition energy in keV for E0 transitions. Z = 92. The figure was taken from ref. (Sof 81) and is intended to indicate the general trend.

FIGURE 22

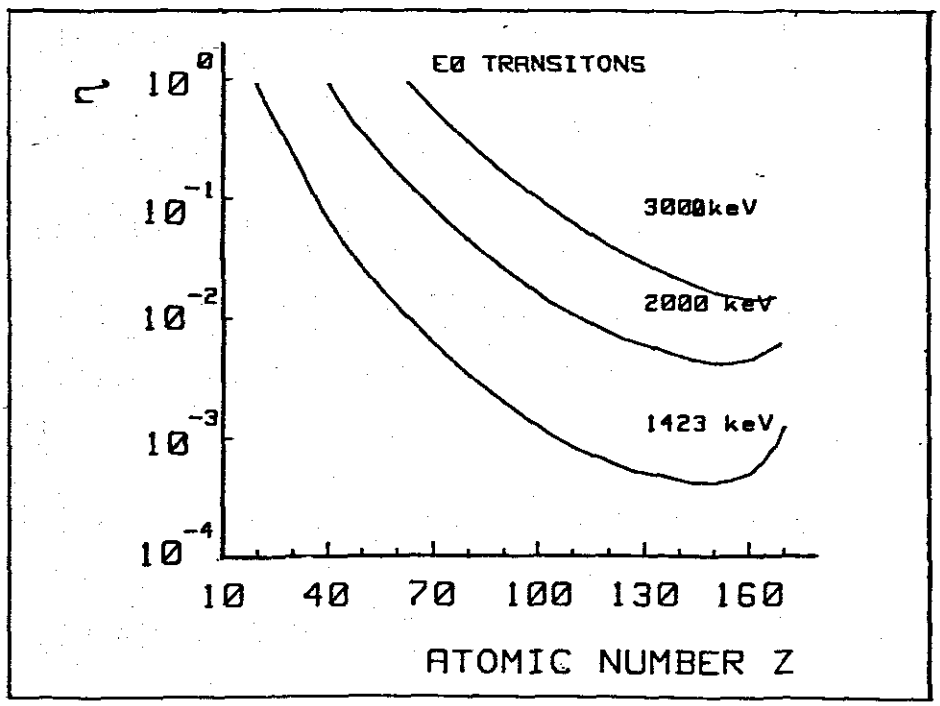

FIGURE 22: The ratio η vs atomic nuclear Z for E0 transitions of various transition energies. The figure was taken from ref. (Sof 81) and is intended to indicate the general trends.

From these results it is clear that η depends strongly on Z, the atomic number, and E, the transition energy. For the transition presently investigated in this work specifically, η is negligibly small ($\eta < 10^{-2}$ for $Z < 40$, $E < 1\,400$ keV). It is thus valid to assume that the E0 transitions proceed solely by internal conversion at these energies. Descriptions of experimental procedures for studying internal pair production are discussed elsewhere (War 65, Pas 78).

3.4 Angular distribution of conversion electrons

A General

The angular distribution of conversion electrons differ from the angular distribution of gamma-rays. It can be obtained by introducing normalized directional particle parameter b_k, where b_k depends on the subshell from which the electron is removed, the transition energy and the multipolarity of the transition, as well as Z. (Hag 68, Fau 83, Mor 76, Ham 75).

The distribution for conversion electrons can be written as:

$$W_e(\theta) = 1 + A_2(e)\, P_2(\cos\theta) + A_4(e)\, P_4(\cos\theta) + \ldots \qquad \ldots 3.4.1$$

where $A_k(e) = b_k A_k$.

Similarly to the gamma-radiation coefficients A_k, $A_k(e)$, in the case of multipole mixing, will depend on the mixing ratio:

$$A_k(e) = \frac{1}{1+\delta^2(e)}\, b_k(\Pi,L,\Pi,L)B_k(j_i)F_k(L,L,j_i,j_f) +$$

$$2\delta(e)b_k(\Pi,L,\Pi',L')B_k(j_i)F_k(L,L',j_i,j_f)$$

$$+ \delta^2(e)b_k(\Pi',L',\Pi',L')B_k(j_i)F_k(L',L',j_i,j_f)$$

with $\delta(e) = \delta\sqrt{\frac{\alpha(\Pi', L')}{\alpha(\Pi, L)}}$ ...3.4.2

where δ is the gamma mixing ratio defined in eq. 2.1.3. (Fau 83, Ham 75) and again $L' = L + 1$.

Calculated values of the normalized directional particle parameters b_2 can be obtained from tables by Hager and Seltzer. (Hag 68) . The higher ranks b_4 and b_6 can be found by recurrence relations presented by the same authors. Once again, these parameters are normalized so that $\int_0^{4\pi} W_e(\theta) d\Omega = 4\pi$.

In obtaining results from internal conversion measurements these distributions must be taken into account. For this purpose a simple program (Appendix B) can be used to determine $W_e(\theta)$ for each particular angle θ with the beam-line for each transition. If the experimental values A_k are not known, estimates of σ/j_i should be made, empirically or according to a specific model. As an illustration figures of $W_e(\theta)$ are produced here using A_k for complete alignment.

On comparison with distributions of gamma-rays, it is obvious that the distributions of conversion electrons can differ considerably from that of gamma-rays for the same transition.

Since the anisotropic distribution of conversion electrons stems from the fact that the angular momenta of the excited nuclei are aligned perpendicular to the beam axis, and such alignment is described by the statistical tensor B_k, it is clear that radiation with $j_i = 0$ will be isotropic, or simply $B_k(0) = 0$. Hence E0 conversion electrons are emitted isotropically as well as all pure multipole radiations where $j_i = 0$.

For E0 transitions where $j_i \neq 0$, E0 transitions compete with M1 and E2 multipole emissions, and although pure E0 transitions are emitted isotropically, the E0 presence influences the angular distribution and an interference parameter $b_2(E0, E2)$ (Ham 75, Pau 75, Hag 69) has to be introduced. In such a case $A_k(e)$ depends on $\delta(e)$ and on q

$$A(e) = [1+\delta^2(e)(1+q^2)]^{-1}[b_k(M1,M1)B_k(j_i)F_k(1,1,j_i,j_f) + 2\delta(e)b_k(M1,E2)B_k(j_i)F_k(1,2,j_i,j_f) + 2\delta(e)qb_k(E0,E2)B_k(j_i) + \delta^2(e)b_k(E2,E2)B_k(j_i)F_k(2,2,j_i,j_f)] \quad ...3.4.3$$

ref. (Ham 75, Pau 75)

It should be noted that no $b_k(E0,M1)$ parameter exists and that $b_k(E0,E2) = 0$ for $k > 2$. (Pau 75, Hag 69). Tabulated values can be found in tables presented in ref. Hag 69. Examples of such experimental work is described by J.H. Hamilton (Ham 75).

Angular distributions of conversion electrons can be used to determine multipolarities of electromagnetic transitions and determination of ratios of subshell conversion coefficients of different subshells. Using a spectrometer resembling one gap of a mini-orange spectrometer, Faust et al (Fas 83) performed such experiments.

Here again, as for gamma-radiation, in an experimental arrangement $W_e(\theta)$, would be represented by

$$W_e(\theta) = \sum_{k=0}^{\infty} q_k A'_k(e) P_k \cos\theta. \quad k \text{ even}$$

$$= \sum_{k=0}^{\infty} q_k \alpha_k A_k(e) P_k \cos\theta. \quad k \text{ even.} \quad ...3.4.4$$

FIGURE 23

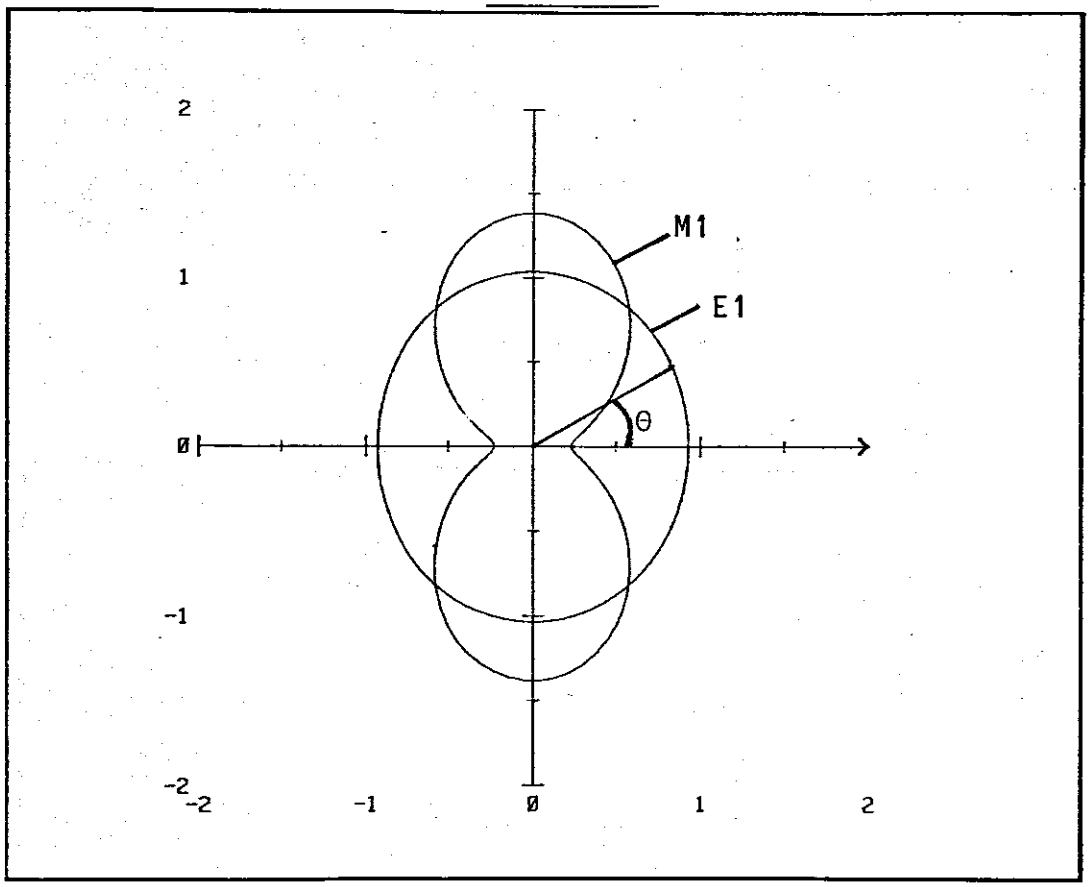

FIGURE 23: Angular distribution $W_e(\theta)$ of internal conversion electrons from aligned nuclei for $j_i = 1$ and $j_f = 0$, 1300 keV E1 and M1 transitions. Z = 48.

B Penetration effect and directional distribution

When penetration effects are important (Kri 73, Chu 60) terms must be added to direction particle parameters as well.

$$b_2'(EL,EL) = b_2(EL,EL)(1 + C_1\lambda_1 + C_2\lambda_1^2 + C_3\lambda_2 + C_4\lambda_2^2),$$

$$b_2'(ML,ML) = b_2(ML,ML)(1 + D_1\lambda + D_2\lambda^2),$$

$$b_2'(EL,ML') = b_2(EL,ML')(1 + E_1\lambda + E_2\lambda^2),$$

$$b_2'(ML,EL') = b_2(ML,EL')\ (1 + F_1\lambda) \qquad \ldots 3.4.5$$

ref. (Hag 69)

with $L' = L + 1$ and where b_2 are the parameters discussed previously and tabulated by Hager and Seltzer (Hag 68). The coefficients C_i, D_i, E_i and F_i are tabulated by Hager and Seltzer. (Hag 69). Detail about b_4 recurrence relations and b_2 interference particle parameters are also given elsewhere. (Hag 69).

FIGURE 24

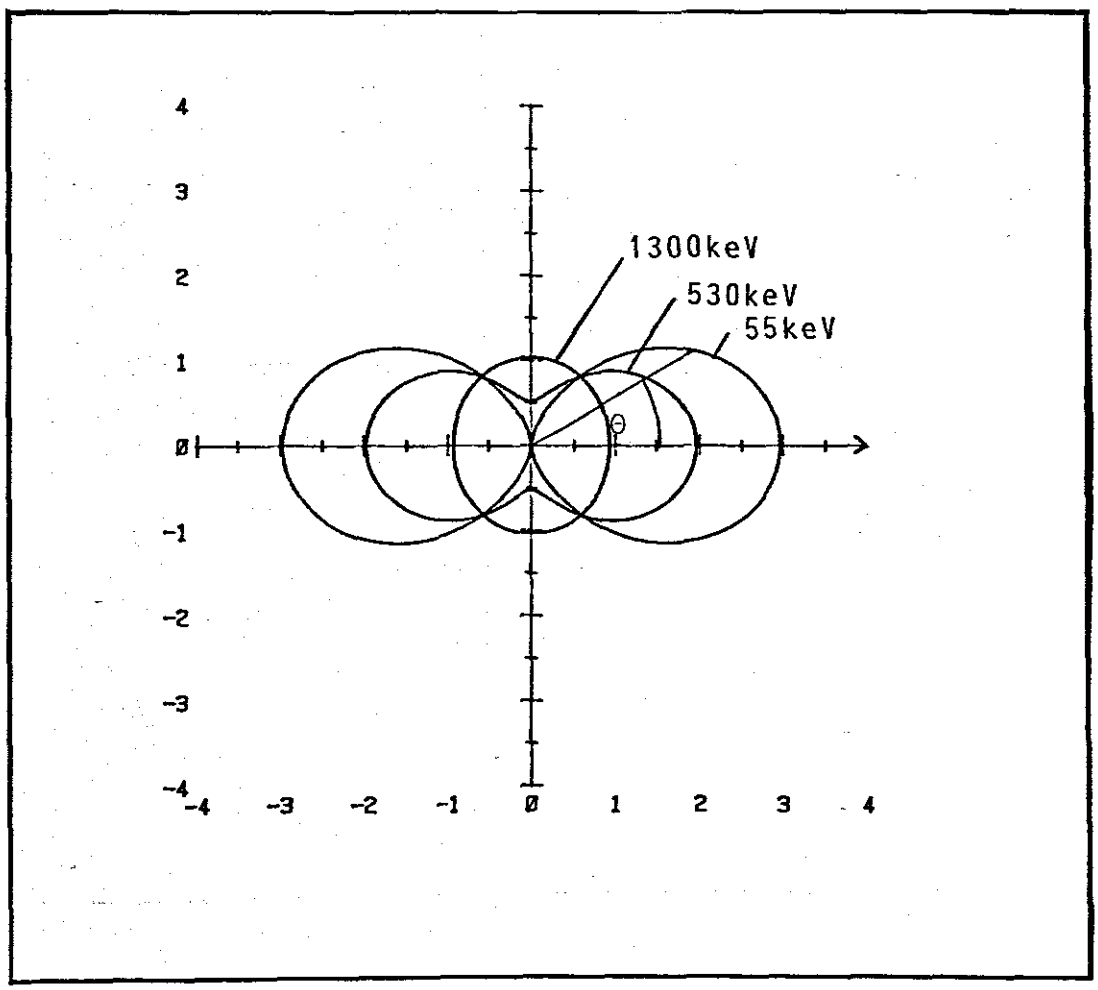

FIGURE 24: Angular distribution $W_e(\Theta)$ of internal conversion electrons from aligned nuclei for $j_i = 1$ and $j_f = 0$, E1 transitions for various transition energies. Z = 48.

FIGURE 25

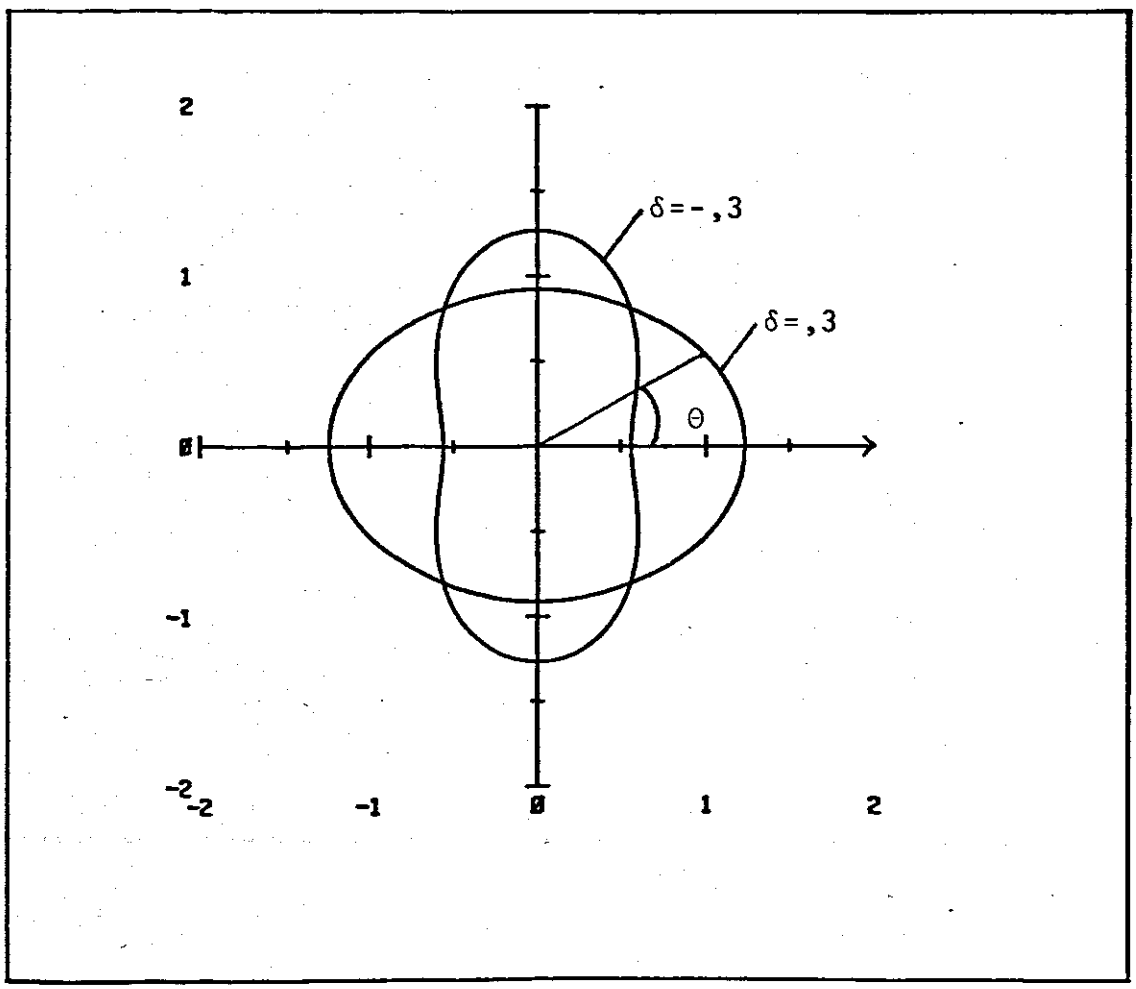

FIGURE 25: Angular distribution $W_e(\Theta)$ of internal conversion electrons from aligned nuclei for $j_i = 2$ and $j_f = 1$, 1300 keV transition for E1/M2 admixture (δ = -0,3) and M2/E1 admixture (δ = +0,3). Z = 48.

FIGURE 26

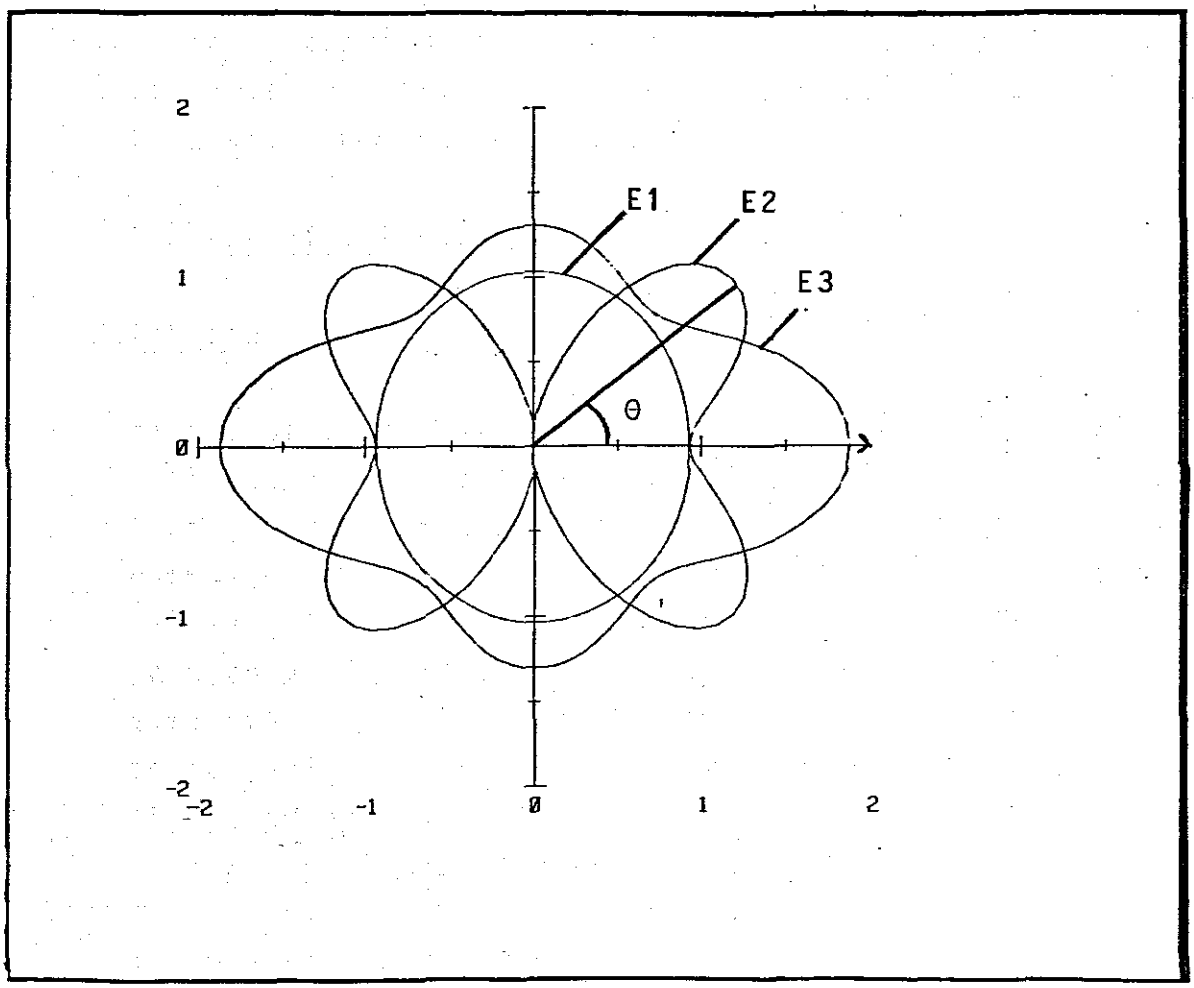

FIGURE 26: Angular distribution $W_e(\theta)$ of internal conversion electrons from aligned nuclei for E1 ($j_i = 1$, $j_f = 0$), E2($j_i = 2$, $j_f = 0$) and E3($j_i = 3$, $j_f = 0$) transitions. 1300 keV transitions, Z = 38.

CHAPTER 4

THE MINI-ORANGE ELECTRON SPECTROMETER

4.0 The apparatus

In this work a mini-orange electron spectrometer was used. It consists basically of two components; the Si(Li) detector, and a magnetic filter.

4.1 The Si(Li) detector

Introduction

In recent years semiconductor devices have almost completely replaced all other techniques of charged particle detection. These devices produce signals linearly proportional to the energy of the incident particle or photon. In this work a Si(Li) detector from Schlumberger was used. The detector was particularly suitable due to its compactness (300 mm^2 sensitive area), and the fact that these detectors are insensitive to magnetic fields. High energy resolution was obtained (1,75 keV at 624 keV), enabling resolution of K,L and M electron peaks of the sources investigated.

A Detector thickness

i) Stopping power

In this work electron-energies below 1,5 MeV were considered, and from table 5 it can be seen that a detector of thickness 4 mm will be sufficient to effectively stop all electrons.

TABLE 5

ENERGY (MeV)	RANGE (mm)
5,00	12,7
4,00	10,3
3,00	7,86
2,00	5,02
1,50	3,63
1,00	2,29
0,80	1,74
0,60	1,20
0,50	0,936
0,40	0,687
0,30	0,451
0,25	0,341
0,20	0,242
0,15	0,152

TABLE 5 The mean range of electrons in silicon, taken from ref. (Ber 69.)

According to Berger et al (Ber 69) the probability of total absorbtion of 1,5 MeV electron in 3 mm silicon is 0,80. This value steadily increases to 0,86 as the energy falls to 0,5MeV, and remains at this value for lower energies. The effectivity of the detector was hence considered to be the same for all electrons with energies below 1,5 MeV.

ii) Detection sensitivity

The Si(Li) detector is sensitive only in the depletion layer. The thickness of the depletion layer varies as $\sqrt{V\rho}$, where V is the applied bias voltage, and ρ the resistivity of the base material. This is illustrated in fig. 27 (ref. Gib 68). For the detector used in this work a bias voltage of -500V was used.

FIGURE 27

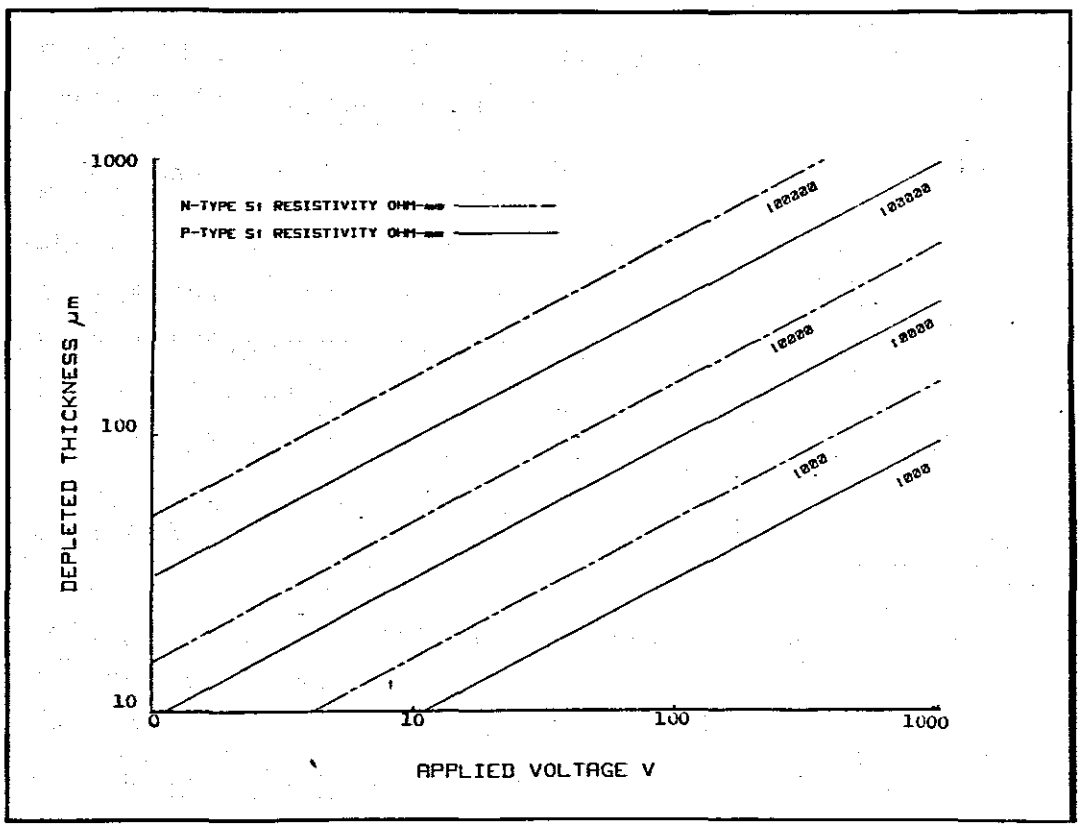

FIGURE 27: The depleted thickness of n- and p-type silicon vs applied voltage for different resistivities. The figure was taken from ref. (Gou 66).

B Operating temperature

i) Detector noise

In order to prevent excessive noise in the detector, the crystal should be an insulator to prevent continuous current

between the electrodes. Semiconductors do not fulfil this condition since at room temperature the conduction band is not completely empty due to thermal exitation, since E_g is small compared to kT. Under normal conditions the number of electrons n in the conduction band is given by

$$n = A\, T^{3/2} \exp(-E_g/2kT) \qquad ...4.1.1$$

where:

A = constant for given material
T = absolute temperature
E_g = is the band gap
k = Boltzmann's constant.

(Gou 66)

This problem is partially overcome by cooling the detector crystal to 77 K.

ii) Collection time

A number of electron-hole pairs n is produced when an incident particle is effectively stopped in the sensitive layer, proportional to the energy of the particle. These electron-hole pairs drift through the depleted region under an applied field. The drift velocity v_d of a carrier is given by $v_d = \mu E$ where μ is carrier mobility in $m^2.V^{-1}.s^{-1}$ and E electric field, in V/m, due to the applied bias voltage. From Fig. 28 it is clear that low detector temperature ensures short collection time. Since hole mobilities are less than for electrons the pulse has a slight tail. This is schematically depicted in Figure 29. It is however a much faster pulse with shorter tail compared to that of a gas counter which might extend to 100 μs.

FIGURE 28

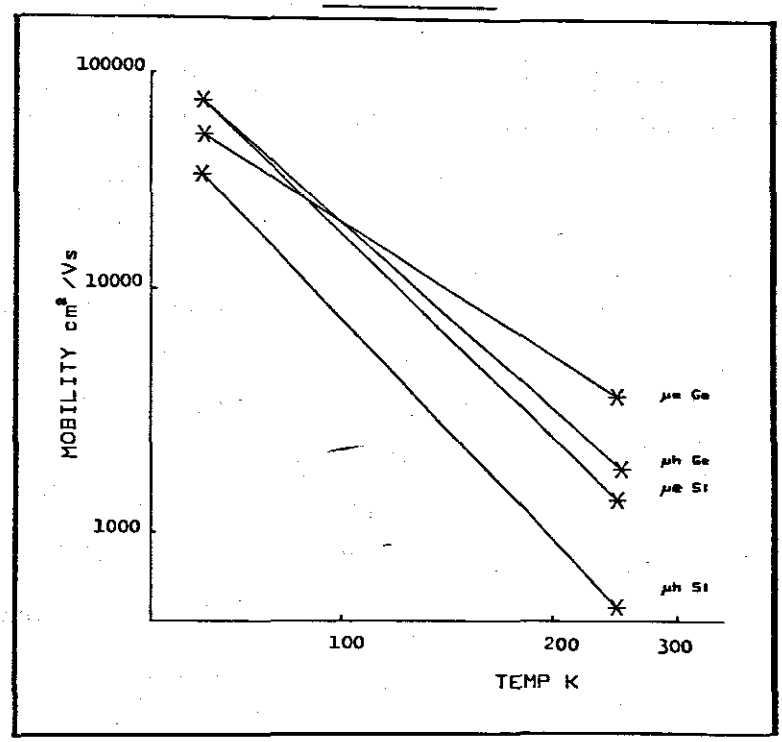

FIGURE 28: Carrier mobilities in silicon and germanium vs. temperature. This illustrative figure was taken from ref. (Gau 66).

FIGURE 29

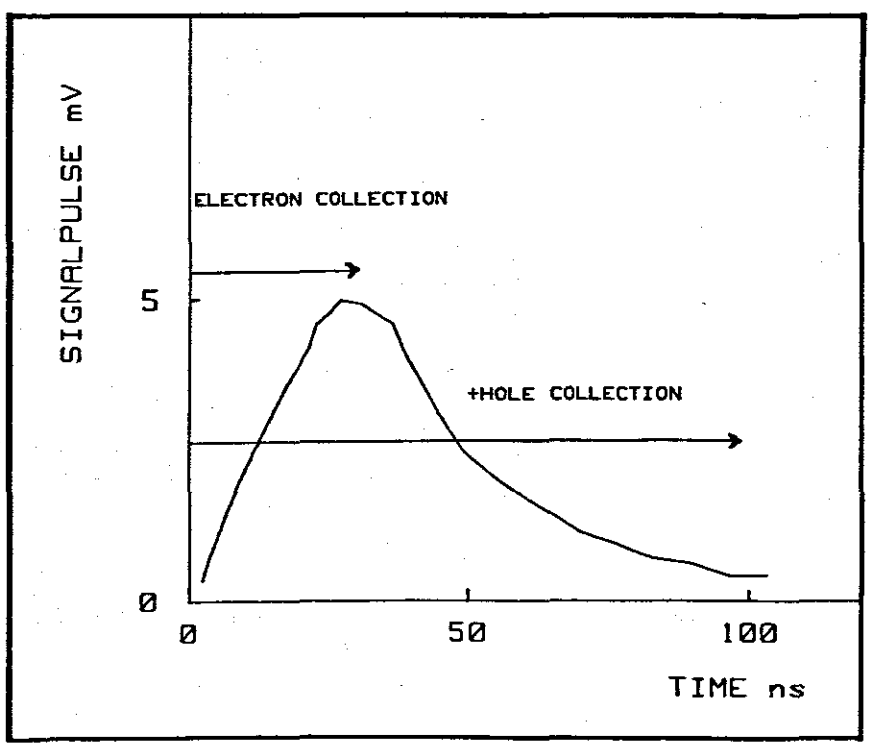

FIGURE 29: A schematic representation of a typical signal shape in silicon detectors (Tai 80)

C Pulse height

If a particle of energy E is effectively stopped in the depletion layer, the total charge q collected per event, will be

$$q = ne = \frac{Ee}{\varepsilon} \qquad \ldots 4.1.3$$

where n is the number of electron-hole pairs formed, and ε is the energy required for pair formation. The signal is removed as a charge pulse and fed to a charge-sensitive preamplifier based on a FET to eliminate noise pulses (Tai 80). The preamplifier used in this work was supplied by Schlumberger with the detector. (Type PSC 761)

FIGURE 30

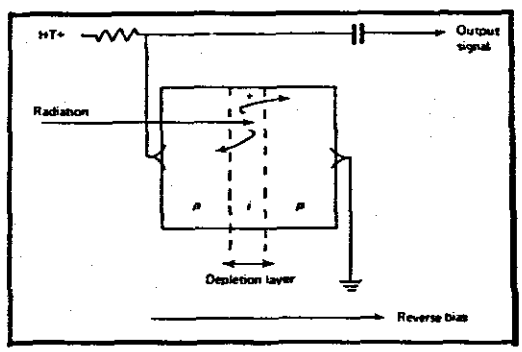

FIGURE 30 A schematic diagram of reverse bias junction detector.

FIGURE 31

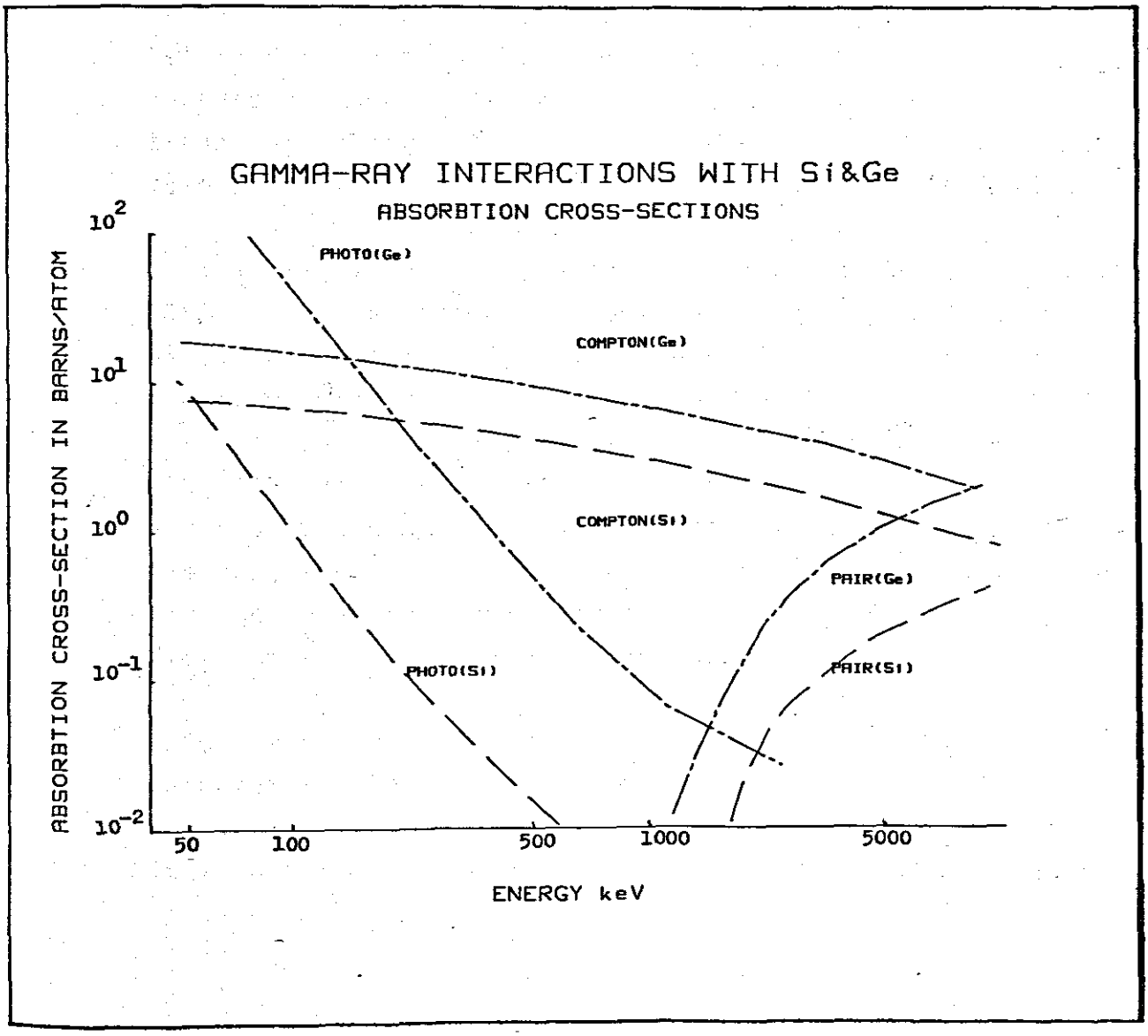

FIGURE 31 The variation of the photoelectric, Compton, and pair-production cross sections in silicon and germanium with energy. The graphs are intended to give an general indication of the orders of magnitude involved. Taken from ref. (Hol 66.)

D Sensitivity

Si(Li) and Ge(Li) detectors are sensitive to charged particles as well as photons. Neutrons also effect the detector due to (n,p) and (n,α) reactions in Si and Ge.

As seen in Figure 31 the photoelectric absorbtion cross-section of Si is considerably less than that of Ge. This makes Ge(Li) detectors more suitable for gamma-spectroscopy. Si(Li) detectors are often used as electron-spectrometers, because of lower backscattering coefficient of Si for electrons, Si having a lower Z than Ge. Si detector also has lower sensitivity to γ-radiation present with the electrons.

Using a ^{207}Bi source with strong gamma-rays at 569,67 keV and 1063,6 keV, Compton-edges would be expected at 393,0 keV and 857,5 keV respectively. In figure 32 a spectrum which was recorded using a ^{207}Bi source and a Si(Li) detector is shown. The gamma-peak at 569,67 keV is clearly visible, together with the two Compton-edges mentioned above. It should be noted that the K and L internal conversion electron peaks of the 569,67 keV and 1 063,6 keV transitions are however much stronger than the gamma-peaks, although the conversion coefficients are much smaller than unity. (Both $\alpha < 0,1$).

This clearly demonstrates the high sensitivity of the Si(Li) detector to electrons at these energies compared to gamma-rays, as was predicted. In conversion electron spectroscopy it is desirable to eliminate all background caused by gamma-rays.

FIGURE 32

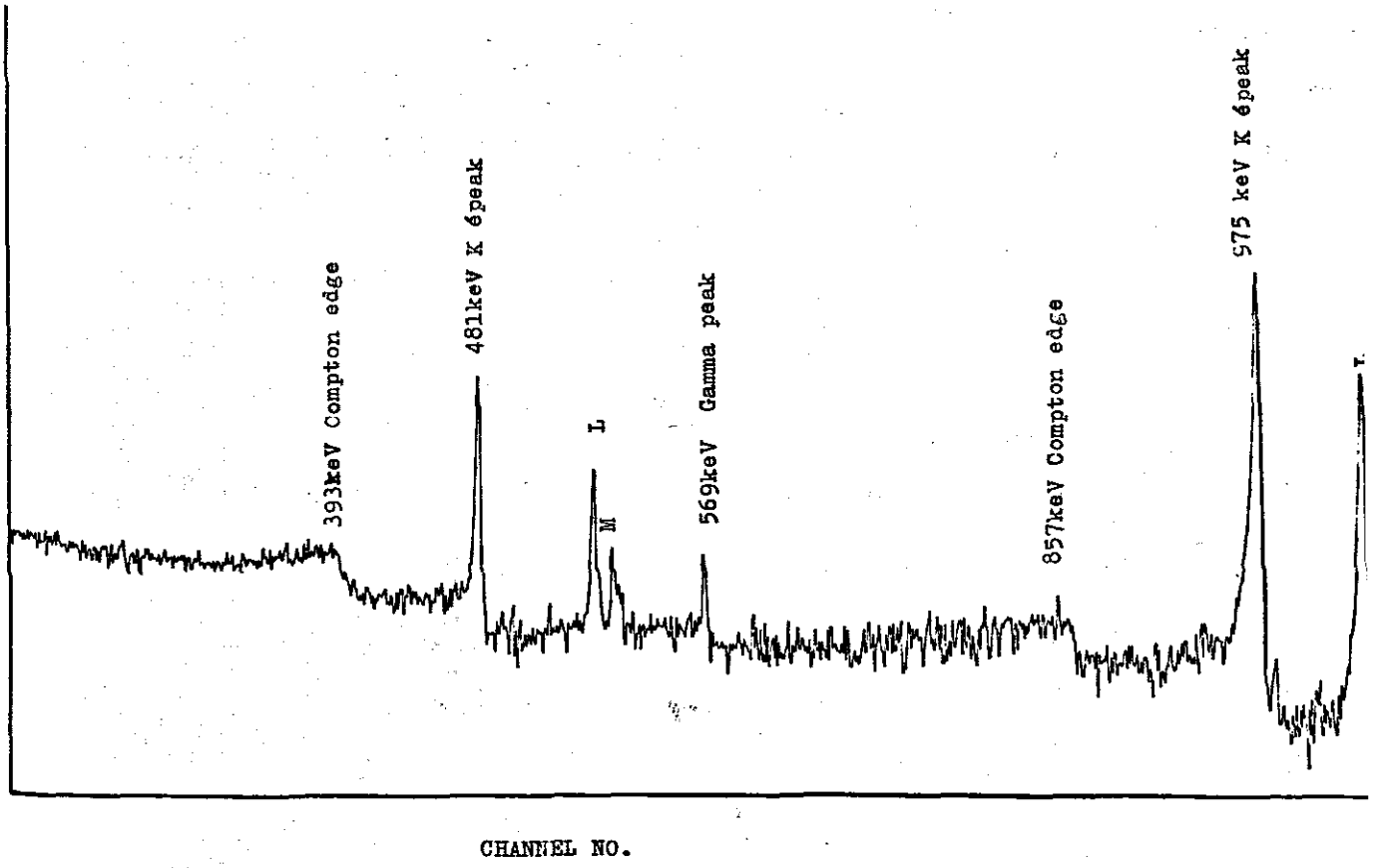

FIGURE 32 A recorded ^{207}Bi spectrum using the unshielded Si(Li) detector. The distance from source to detector was 20 mm and collection time was 5 minutes.

E Backscattering and Bremsstrahlung

Electrons that backscatter near the surface of the detector have a high probability of leaving the detector without depositing all their energy. This causes the tail on the low energy side of the pulse height distribution. Bremsstrahlung also contributes to the loss of total absorbtion, varying from 10 % at 300 keV to 20 % at 600 keV and 50 % at 1 200 keV (Wal 68). The backscattering coefficient also depends on the angle of incidence to the detector surface, as is shown in figure 33.

FIGURE 33

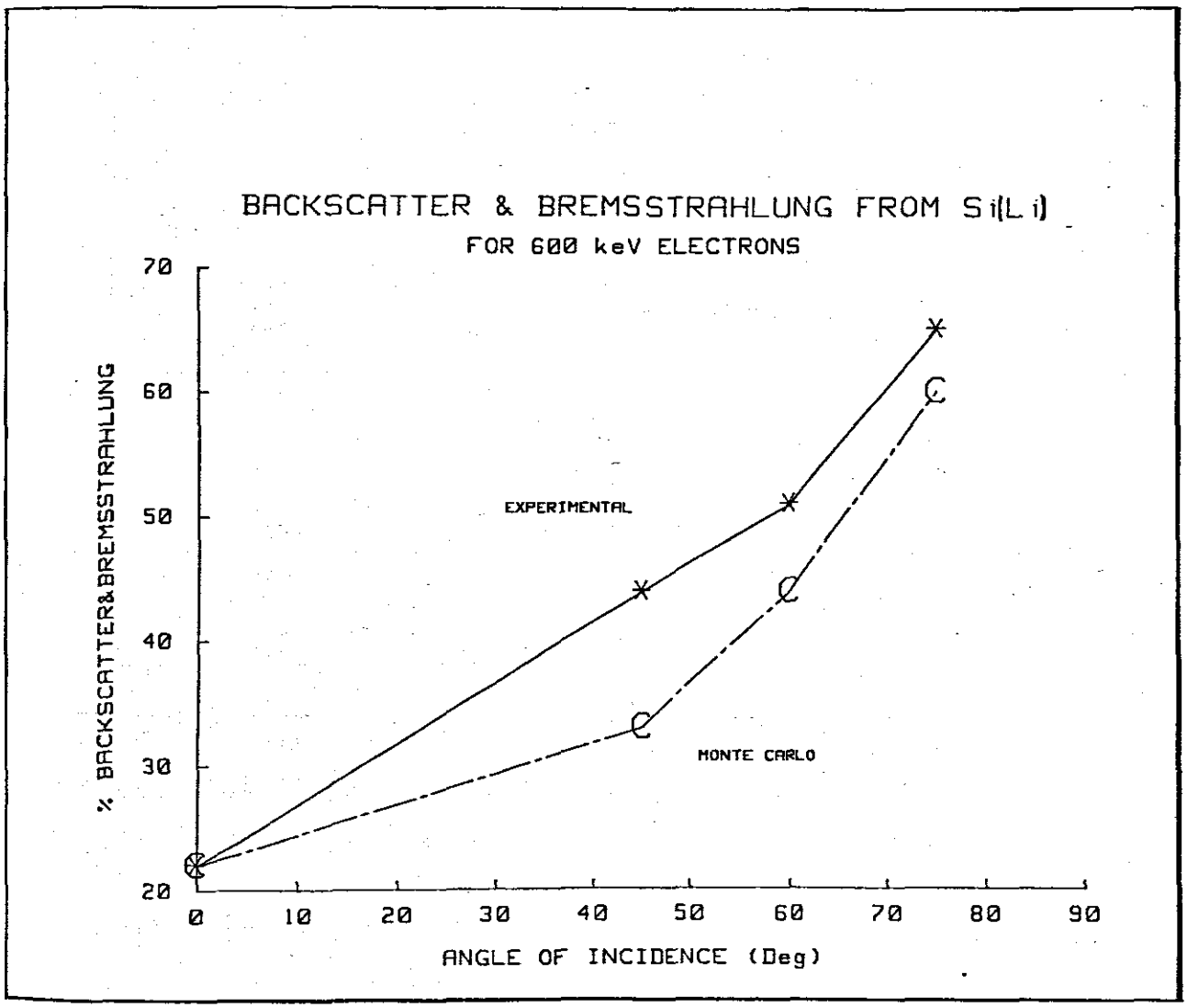

FIGURE 33: The variation of backscattering and bremsstrahlung of 600 keV electrons from Si(Li) detector with angle of incidence. Values taken from Waldschmidt et al (Wal 68) are plotted here.

For electrons of normal incidence the percentage backscattering seems to be practically independent of the energy of the electrons as is displayed in fig. 34. (Ber 69, Wal 68). The values of Hühn and Schneider seem to contradict this, but this seems to be due the failure to correct for electrons losing energy at the collimator in front of the detector. (Ber 69).

FIGURE 34

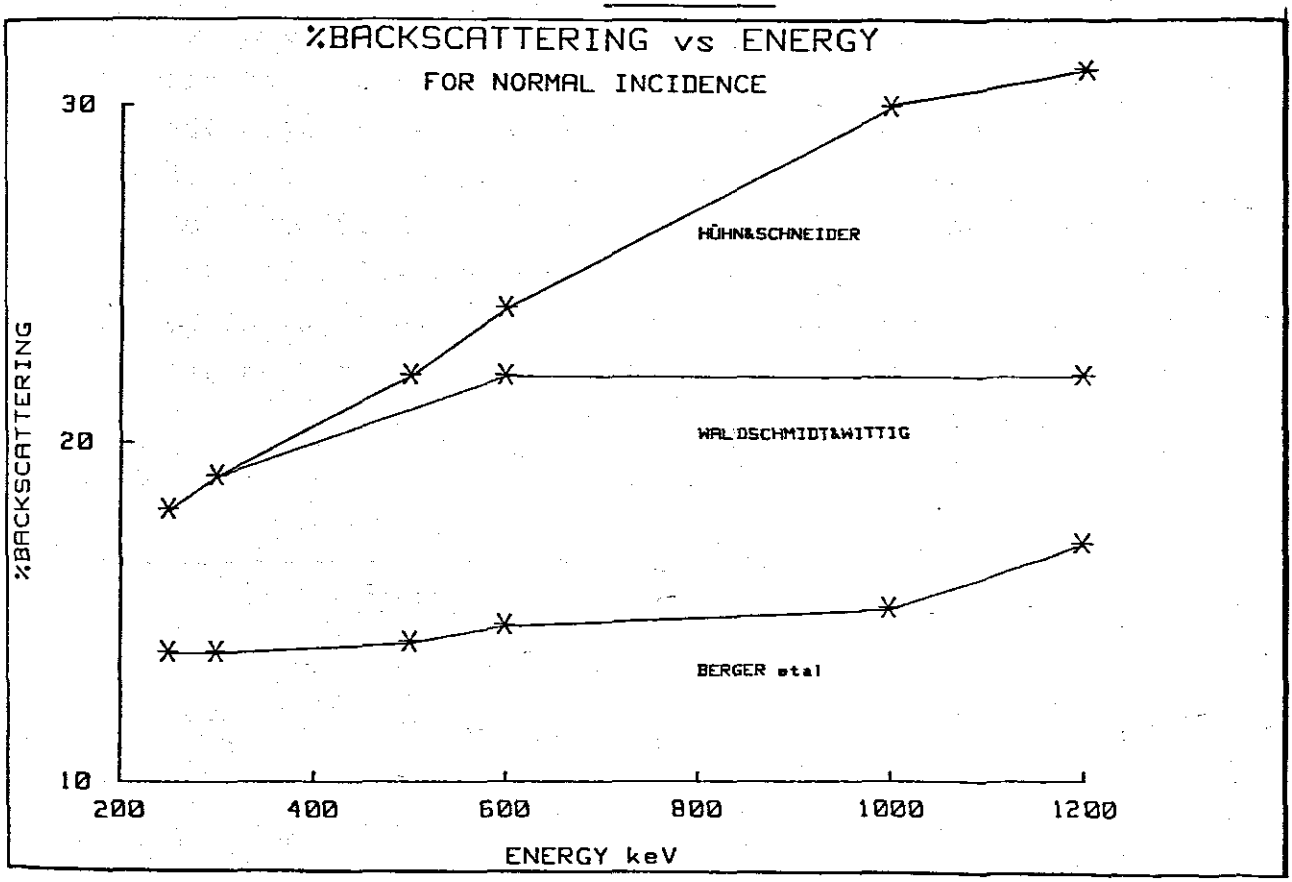

FIGURE 34: Backscattering of normal incident electrons from Si(Li) detector for different electron energies. Values as given by Berger et al. (Ber 69) are plotted.

4.2 The magnetic filter

In most cases gamma-, beta- and positron-backgrounds are present when conversion electron spectra are recorded. In such a spectrum with a Si(Li) detector only, the conversion lines are hidden under a continuous spectrum due to this high background. In-beam experiments where conversion spectra are recorded following nuclear reactions produced by accelerated particles usually require spectrometers with the following characteristics:

a) Good energy resolution
b) High transmission efficiency
c) Greatly reduced sensitivity to unwanted radiations such as gamma- and X-rays, delta electrons, scattered particle beams, betas and positrons and other reaction products such as neutrons.

Using a mini-orange type magnetic filter with a Si(Li) detector these requirements are met, and it has the additional advantage of compactness. Similar magnetic filters have been described in detail by several authors. (Ish 75, Kli 72, Kli 78, Neu 79, Kli 75, Ish 71). Small, strong, permanent magnets of $SmCo_5$ are arranged around a central absorber to form a miniture version of a toroidal or orange electron spectrometer, hence the name mini-orange. (See figures 35 and 36.)

FIGURE 35

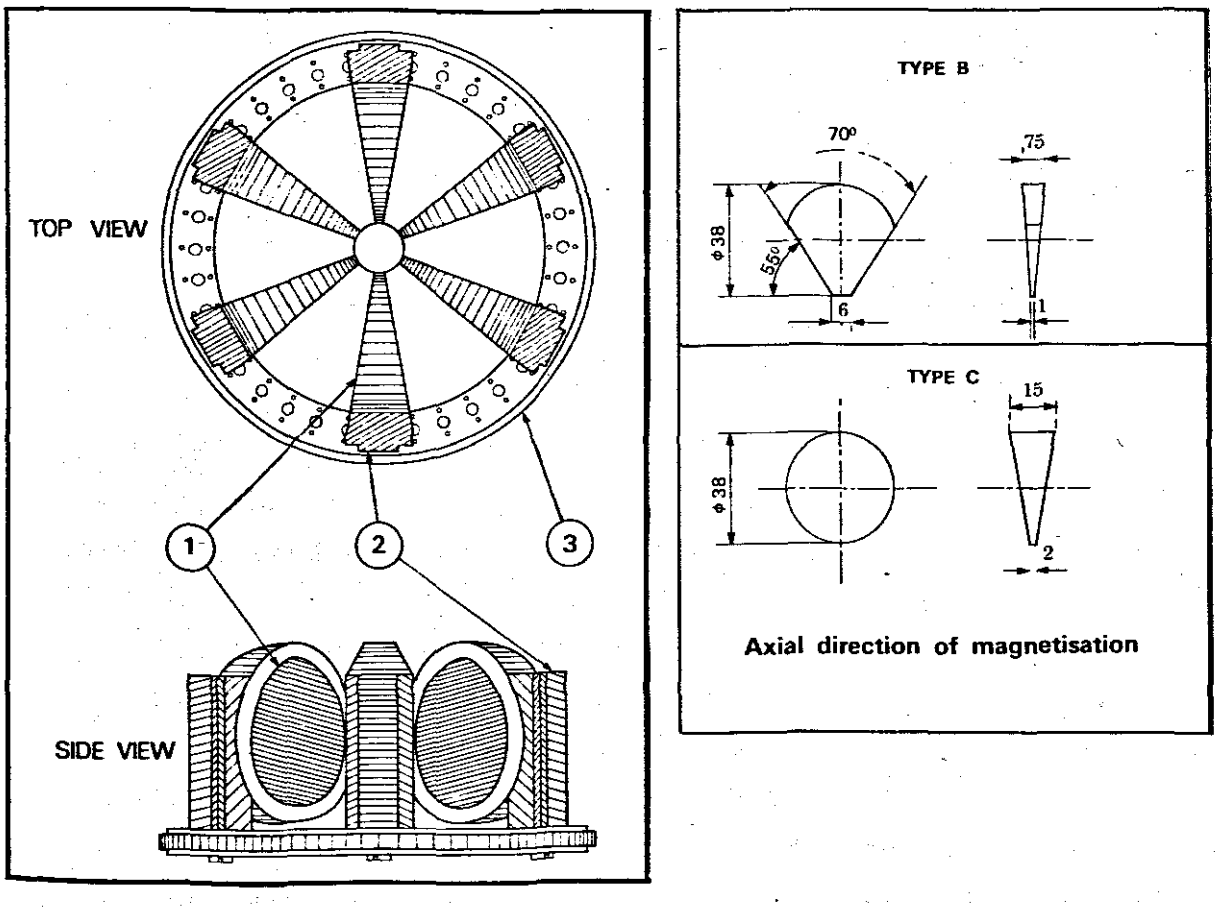

FIGURE 35: a) Schematic drawing of six C-type magnets on mounting ring with (1) RECOMA magnets (2) mounting bracket and (3) mounting ring ref. (Spo 84).
b) Shapes of the two different magnets employed. (Spo 84).

FIGURE 36

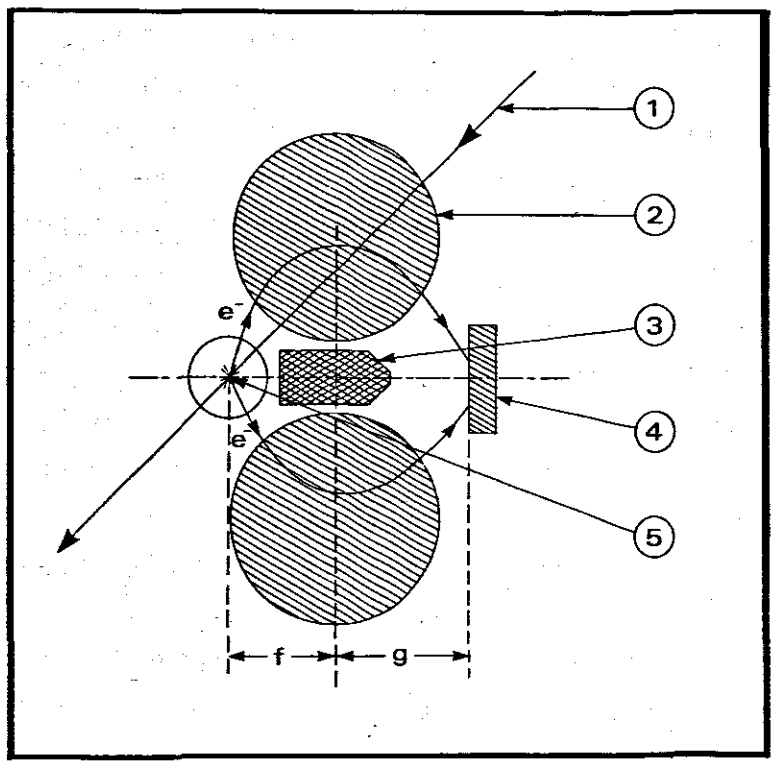

FIGURE 36: Schematic drawing of source, magnets and detector geometry, showing (1) beam-path, (2) magnet, (3) absorber for gamma-rays (and neutrons), (4) detector and (5) source. (Spo 84).

The toroidal field focusses electrons around the central absorber to the detector and diverges the positrons. Using a relatively large surface (300 mm^2) Si(Li) detector compared to the magnetic field area (~3 000 mm^2), a wide energy range of electrons pass through the gaps between the magnets towards the detector and no longer acts as a conventional spectrometer. The resolution of the mini-orange depends entirely on the abilities of the Si(Li) detector. The transmission of the spectrometer however is determined by the magnetic filter and its relative position to source and detector.

Aluminium with Z = 13 was chosen as material for the chamber to reduce residual background caused by secondary Compton and photo-electrons created at the surface of the chamber. Direct gamma- and X-rays from the source were attenuated by the central lead absorber. For in-beam measurements the neutron flux can be reduced by using a backward angle of detection and by placing the detector far away from source so that the solid angle of detection is small. The effect of δ-electrons is also reduced by chosing a backward detection angle, since they are strongly peacked in the beam direction (Bel 82), and by choosing a transmission discriminating against low energy electrons. (Kli 75)

The effect of the filter on the recorded spectrum

Using an ^{152}Eu source, the action of the magnetic filter was demonstrated. From the figures 37 and 38 the following observations were made.

a) The β-background was dramatically reduced using the filter
b) The use of this specific filter results in a maximum transmission in the 400- 500 keV region.
c) At high energies the transmission is very low.
d) Where the transmission is high the signal to background ratio is much larger than without the filter.

See figures 37 and 38.

4.3 Transmission of mini-orange spectrometer

In order to determine the correct rate of emission of conversion electrons at a specific energy, the absolute transmission curve has to be determined experimentally. The

FIGURE 37

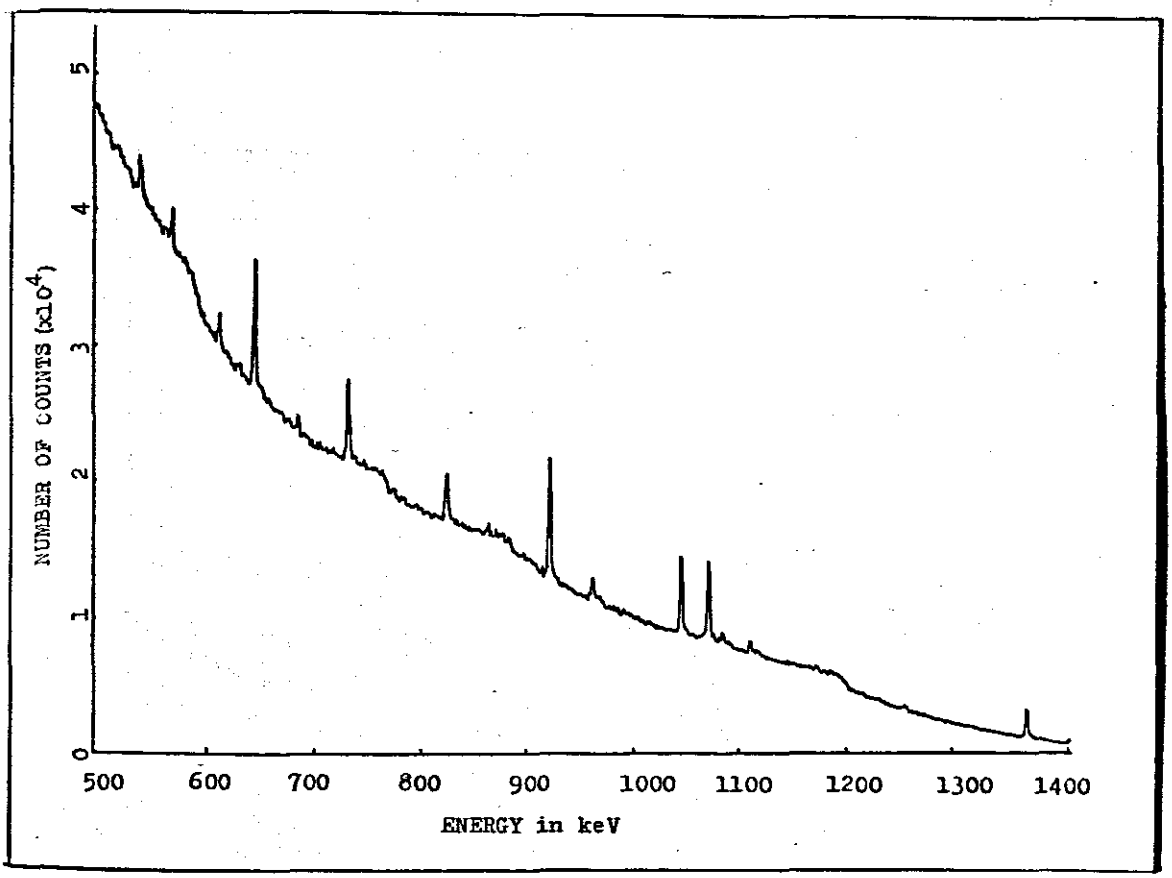

FIGURE 37: The Eu spectrum recorded without the central absorber and magnetic filter.

FIGURE 38

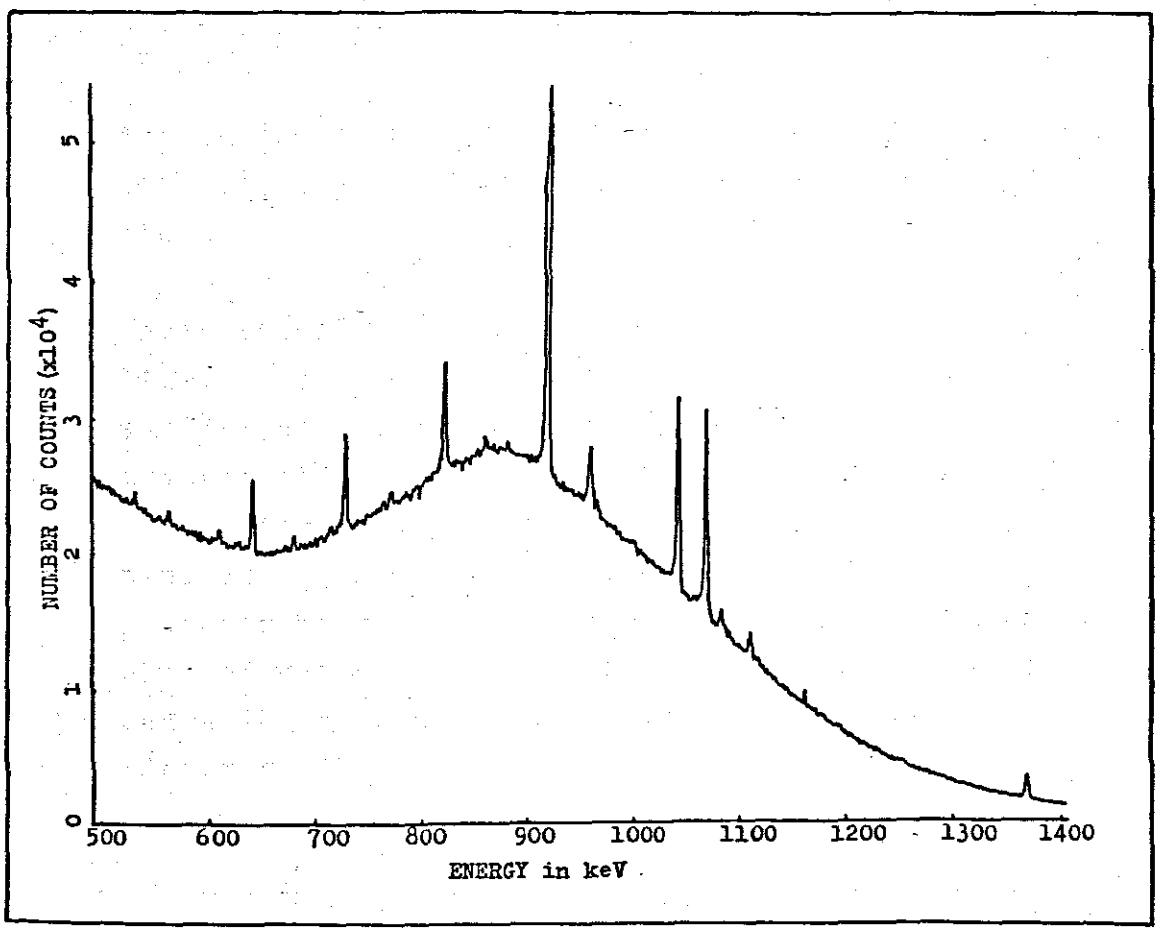

FIGURE 38: The Eu spectrum recorded with the central absorber and magnetic filter.

transmission T(E) of the mini-orange spectrometer depends on the type of magnets used and their configuration, as well as the detector- and source distances g and f (see fig. 36) from the magnets, and the energy of the electrons and the detector response.

$$T(E) = \frac{N_m(E)}{N_o(E)} \qquad \ldots 4.3.1$$

$N_m(E)$ = no. electrons counted by mini-orange
$N_o(E)$ = no. of electrons emmited over 4π.

For calibration ^{137}Cs, ^{134}Cs, ^{207}Bi, ^{152}Eu sources were used to calculate the transmission curves for various configurations.

These sources were chosen because of their convenient half-life values, and because they emmit conversion electrons of sufficient intensity over the energy range for which the transmission of the spectrometer had to be calculated. For the calibration purposes the sources were prepared by depositing chlorides of the isotopes onto a Formvar film mounted on a copper ring. The chlorides were in a solution of 0,1 n HCl, of which one drop was deposited onto the film at a time and allowed to dry until sufficient activity was obtained. (See fig. 39)

FIGURE 39

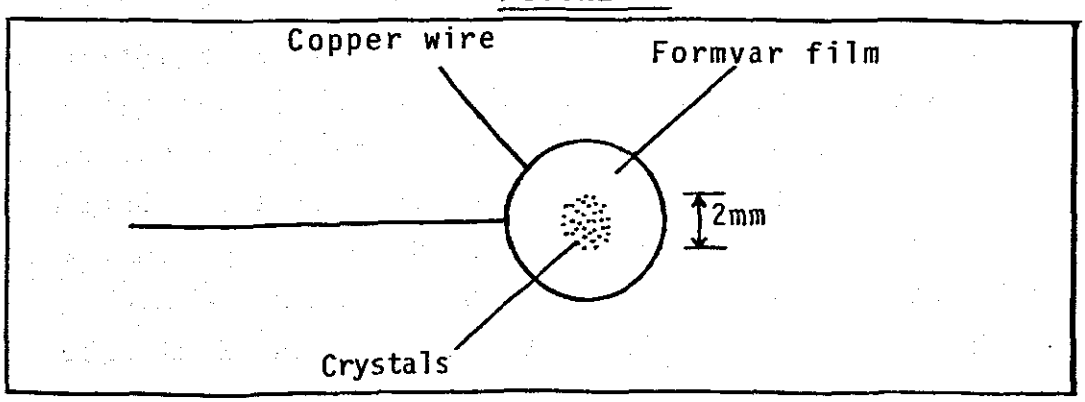

FIGURE 39 Diagram of source holder.

The radioactive material was spread over an area with diameter about 2 mm. The decay schemes and the spectra of the isotopes used for calibration are given in Figures 40 to 43. The transition energies are given in keV together with the number of gamma transitions per hundred decays of the parent nucleus. Some energy levels are indicated (in keV) together with the spin and parities of the levels. See figures 40 - 43. In table 6 some further information on the sources is given.

TABLE 6

RADIOACTIVE NUCLEUS	DECAY PROCESS	PRODUCT NUCLEUS	HALFLIFE
^{152}Eu	β^- 27,9%	^{152}Gd	13,3y
^{152}Eu	β^+ & k capture 72,1%	^{152}Sm	13,3y
^{207}Bi	β^+ & k capture 100%	^{207}Pb	38y
^{137}Cs	β^- 100%	^{137}Ba	30y
^{134}Cs	β^- 99,9%	^{134}Ba	2,062y

TABLE 6: The various radioactive nuclei used and some characteristics of the decays.

In order to determine the correct energies of the conversion electron peaks the binding energies of the atomic electrons of the K- shell of the isotopes used for calibration had to be taken into account. The electron binding energy is defined as the energy required to bring an atomic electron from its bound state to the lowest state where it is free from the attractive forces of the nucleus. The binding energies of atomic electrons can be obtained from the X-ray absorbtion edge in X-ray emmission spectra, or more directly from electron spectroscopic data. (Has 66). Values used in this work were obtained from ref. (Has 66.)

FIGURE 40

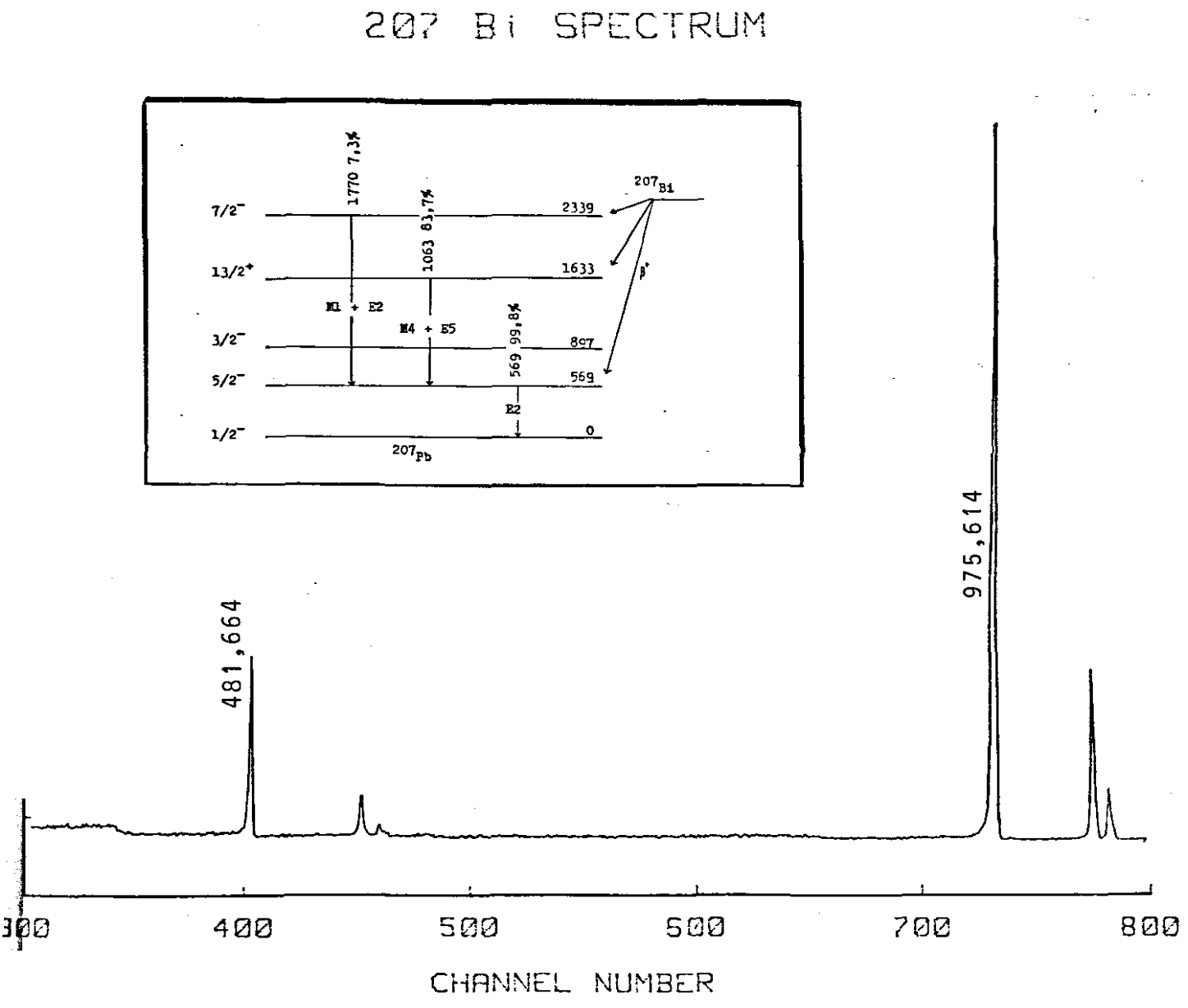

FIGURE 40: Decay scheme and recorded spectrum of ^{207}Pb.

FIGURE 41

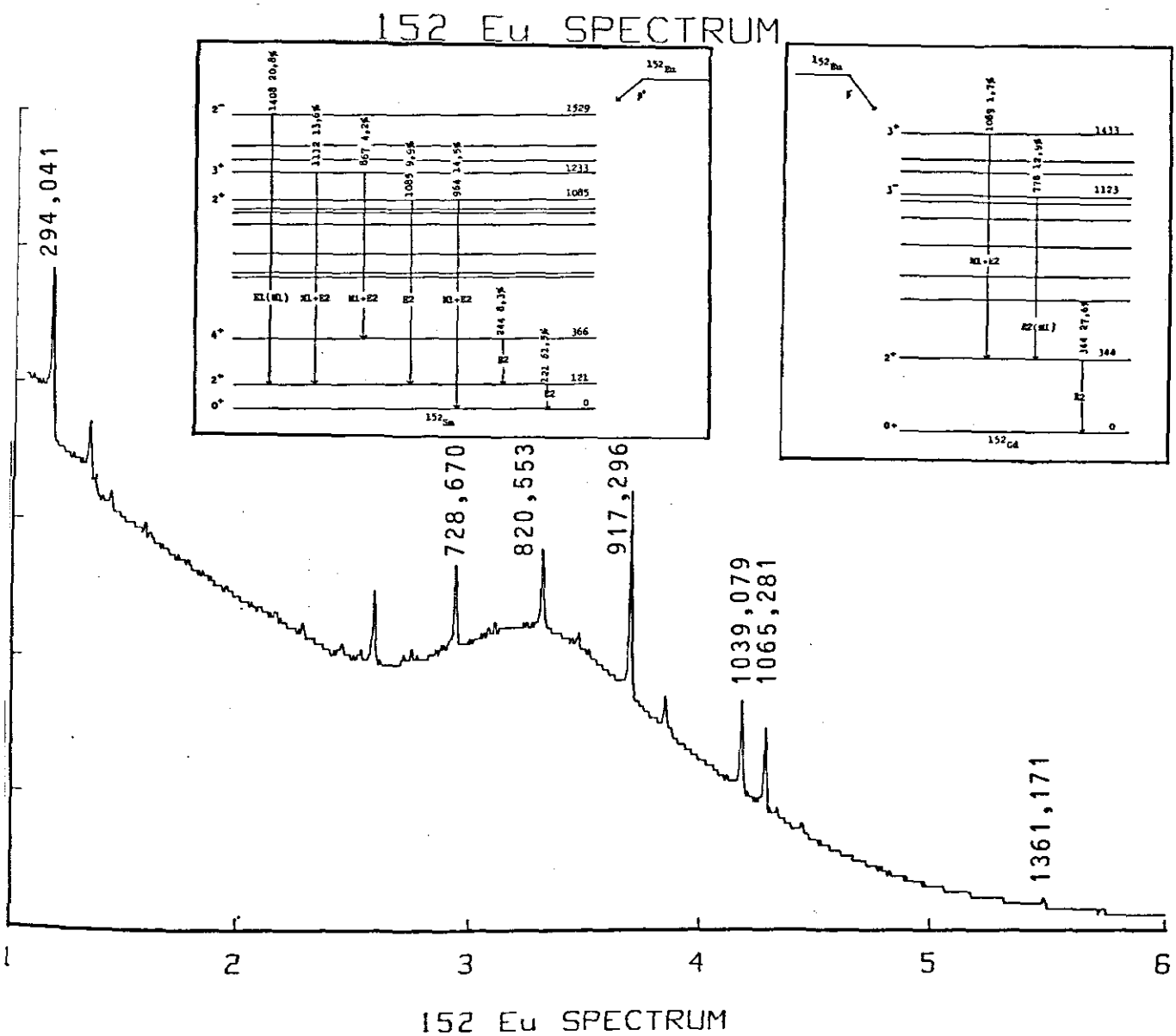

FIGURE 41: Decay schemes of ^{152}Sm and ^{152}Gd with the recorded spectrum.

FIGURE 42

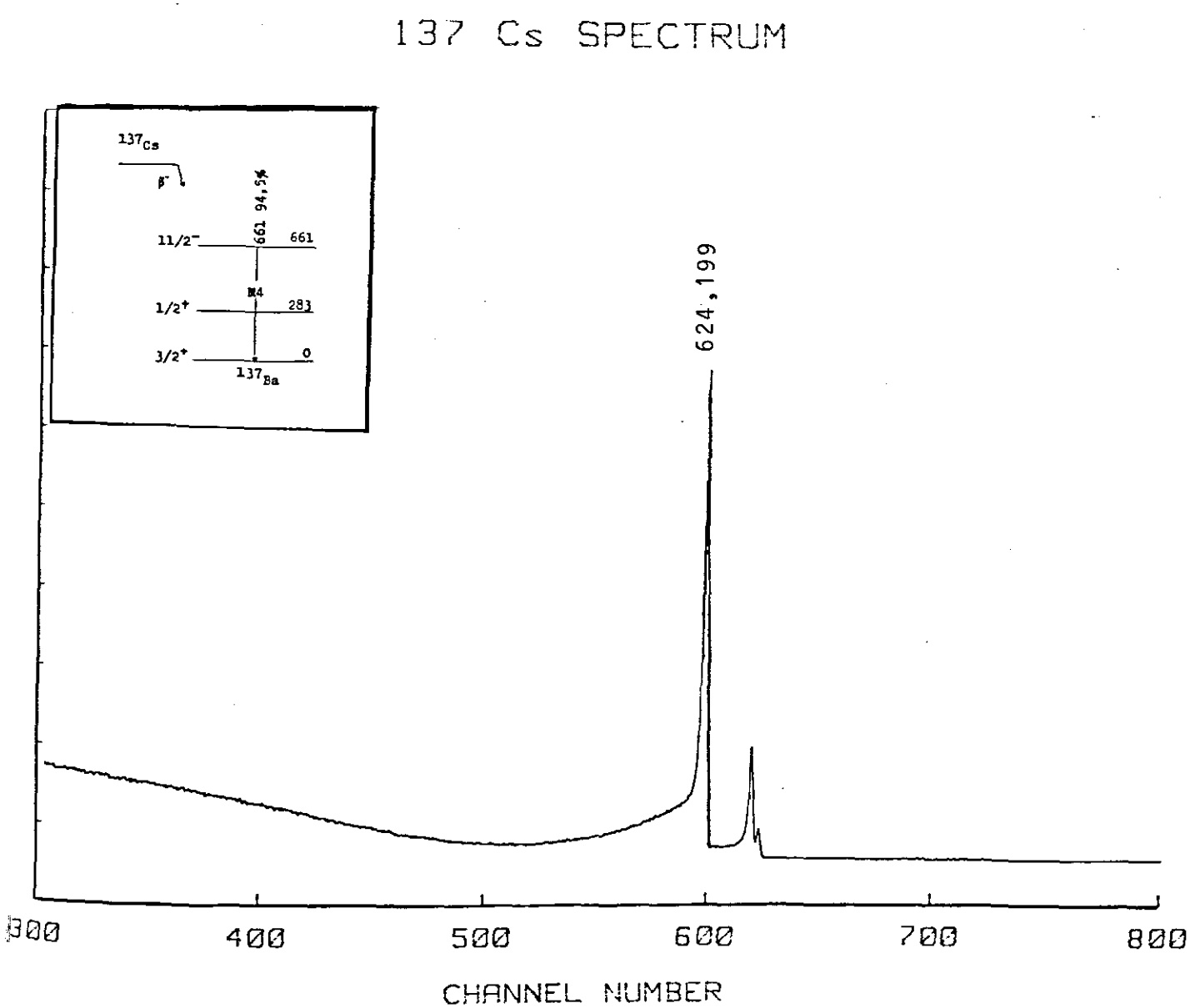

FIGURE 42: Decay scheme of ^{137}Ba and the recorded spectrum.

FIGURE 43

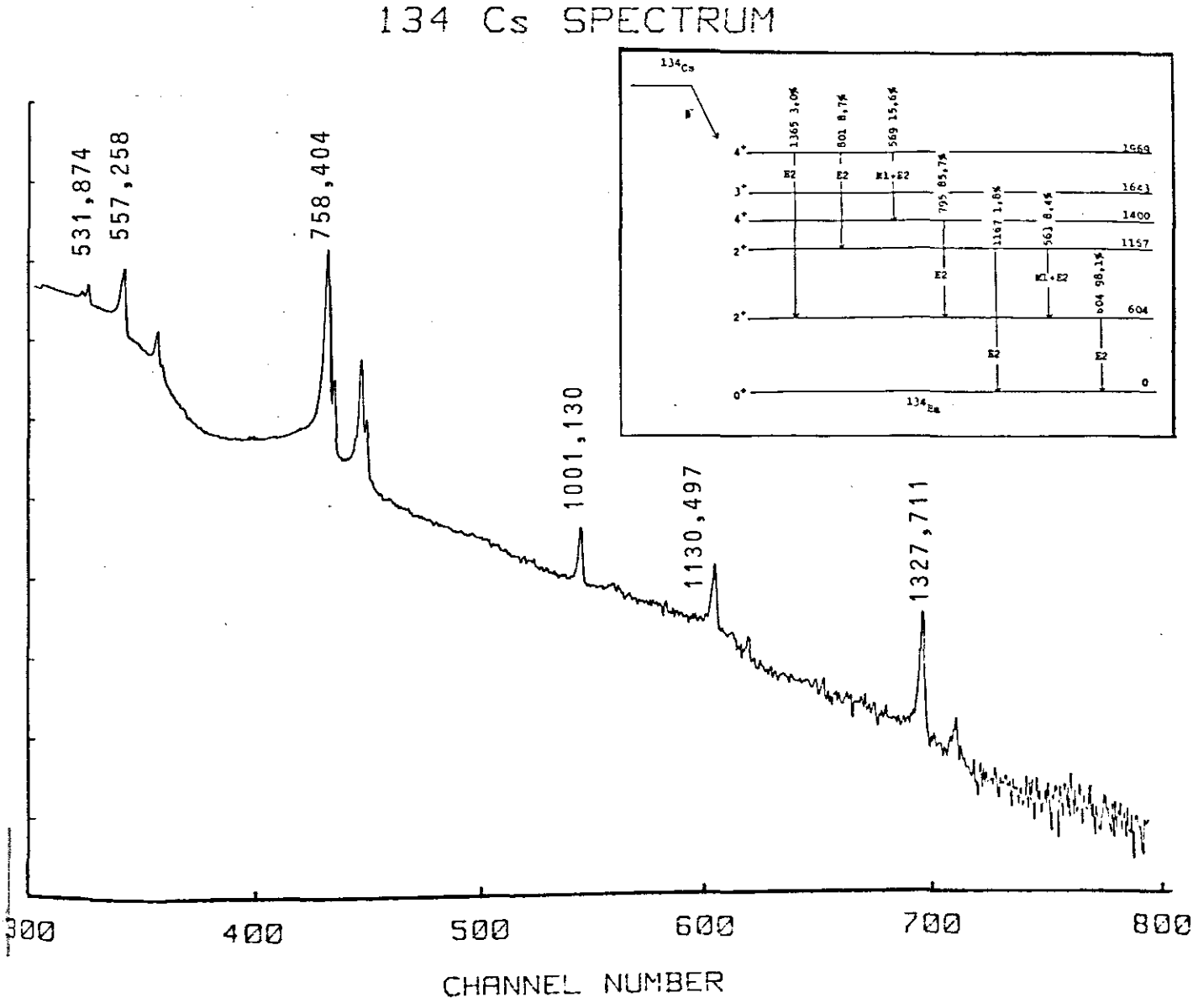

FIGURE 43: Decay scheme of ^{134}Ba and the recorded spectrum.

TABLE 7

ELEMENT	K-SHELL BINDING ENERGY IN keV.
Ba	37,441
Sm	46,835
Gd	50,240
Pb	88,006

TABLE 7: The K-shell binding energies for the calibration sources. The values were taken from ref. (Has 66.)

Each source was calibrated by placing the source at a distance f + g from the detector (see fig. 36) for a period T with no magnets or absorber. The number of conversion electrons counted in a peak $I_o(E)$ was then corrected to give the total no. of electrons emitted by the source at that energy in 4π.

It was done as follows:

$I_o(E)$ is no. of electrons in peak counted by detector.

Then $I(E) = \frac{I_o(E)}{1-k}$ is the no. of electrons which reach the detector, where k is the fraction of electrons not fully depositing their energy due to backscatter and bremsstrahlung.

...4.3.2

According to Waldschmidt and Wittig (Wal 68) only backscatter and bremsstrahlung have to be considered to account for detector losses, and they found experimentally that for electrons entering the detector at angle of incidence $\emptyset = 0°$, the value of k is virtually energy independent in the region below 2 000 keV. (See table 8).

TABLE 8

E in keV	k
300	0,19
600	0,22
1 200	0,22

TABLE 8: The backscattering and bremsstrahlung fraction k for normally incident electrons at various electron energies. The values were obtained from ref. (Wal 68) for Si(Li) detector.

$N_o(E)$ was then calculated:

The detector subtends a solid angle $A/(f+g)^2$ where A is the surface area of te Si(Li) detector.

Hence the no. electrons emitted in 4π at that energy E is

$$N_o(E) = I(E)\left[\frac{(f+g)^2}{A}\right]4\pi$$

$$= \frac{I_o(E)(f+g)^2\ 4\pi}{(1-k)A} \qquad \ldots 4.3.3$$

Since the diameter of the detector surface is 20 mm compared to f+g ranging from 50 to 100 mm, the angle of incidence for all electrons was taken to be 0°. Hence k was taken to be 0,22 (Wal 68). The exact value for k however is not critical, since one is really interested in the relative transmission of the instrument. In our case A was 300 mm^2. Several measurements were made at various distances f and g to ensure that a reliable value of $N_0(E)$ for each peak was obtained.

Using a specific geometric configuration and various numbers of different magnets, the transmission T(E) at each energy peak was calculated. The number of counts in the energy peaks were recorded for some period T and the background was subtracted as in the previous case, to obtain the number of counts in the peak $N_m(E)$. The transmission T(E) of the spectrometer was calculated for all the energies for which one has a reliable reference peak. These points were interpolated to give a graphical representation of the transmission at all energies up to 1 350 keV.

Results

The transmission of various configurations determined by varying the distance from source to centre of magnetic filter f, and the distance from the centre of the magnetic filter to the detector g. Different magnets can be arranged to form the filter. By arranging different numbers of magnets the effect of the filter can also be altered.

The intention was to determine the most suitable configuration for the experiment on ^{112}Cd. In this experiment a transmission curve with a low energy cut-off (below 500 keV) and reasonably high transmision at both 600 keV and 1 200 keV was required.

Accurate measurements were made using 6C type magnets arranged symetrically around the ring. Transmission curves for different values of f and g were determined. Using this magnet configuration the highest transmissions were achieved, for the energies of interest.

See figures 44, 45 and 46.

There is a sharp cut-off at low energies. This is particularly useful when considering transitions at higher energies when the β^- background is high. The transmission bandwidth can be seen to be very wide in some cases: approximately 400 keV in the 6C magnet configuration. If a particular energy range is of interest, a specific transmission curve can be selected to highlight the particular energy region. A definite pattern in the shift of transmission can be detected as f and g are increased. The maximum transmission gradually shifts to higher energies. One should however also note that if f and g become very large, the maximum transmission eventually decreases.

A tentative determination of the transmission for 8A type magnets was also done, however data points are few and the results can only be used to determine tendencies rather than accurately determining the transmission curve.

See figures 47 and 48.

From the figures the following conclusions were drawn:

a) The maximum transmission appears to be lower for the 8A type magnet configuration than that of corresponding configurations using 6C type magnets.

b) The transmission bandwidth for the 8A type magnet configuration seems to be much narrower than for the 6C type magnet configuration.

FIGURE 44

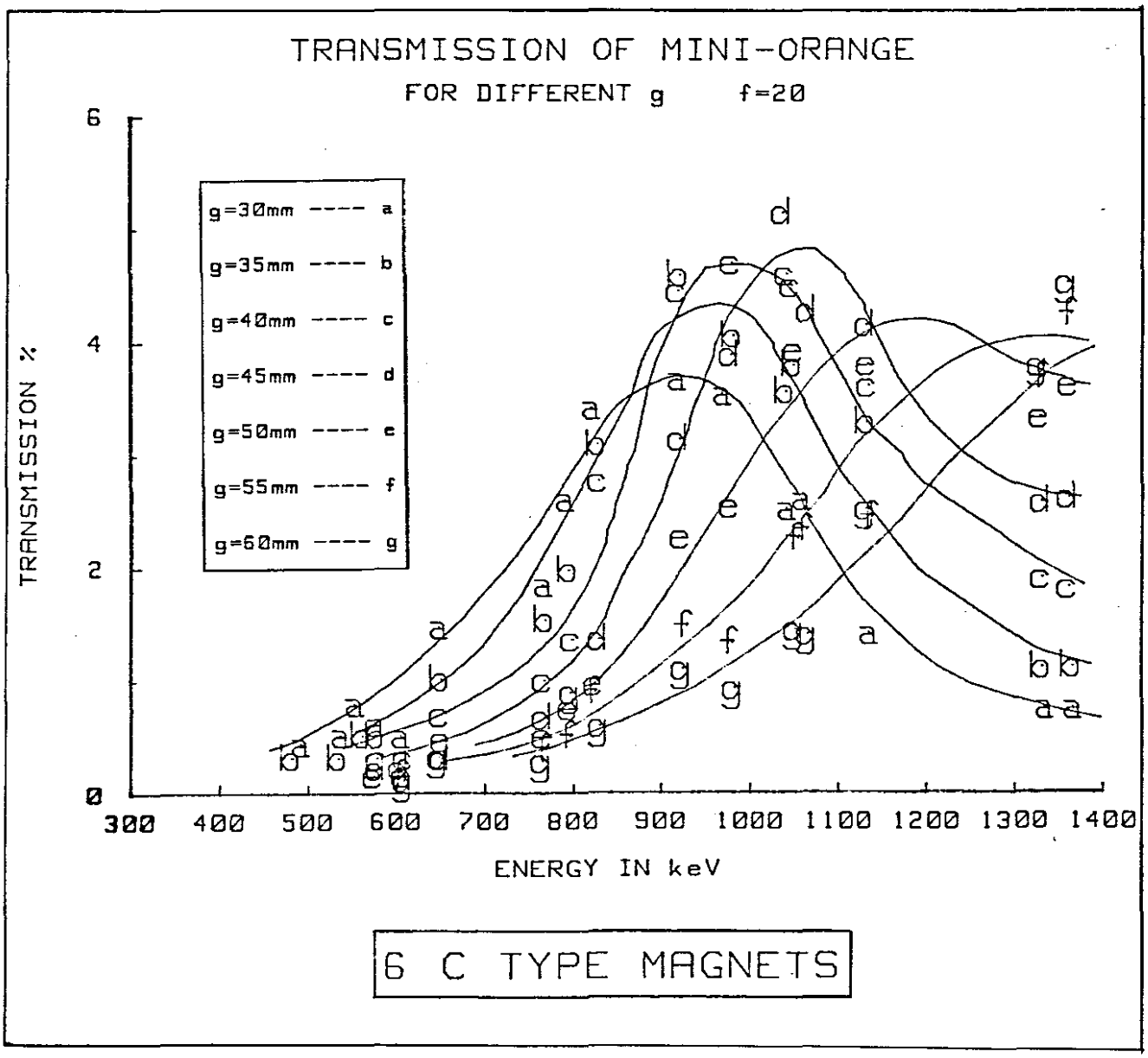

FIGURE 44: Measured transmission curves for 6C type magnets configuration for f = 20. The position of the letters a, b, c, d, e, f indicate experimental values, and the graphs are drawn to guide the eye.

FIGURE 45

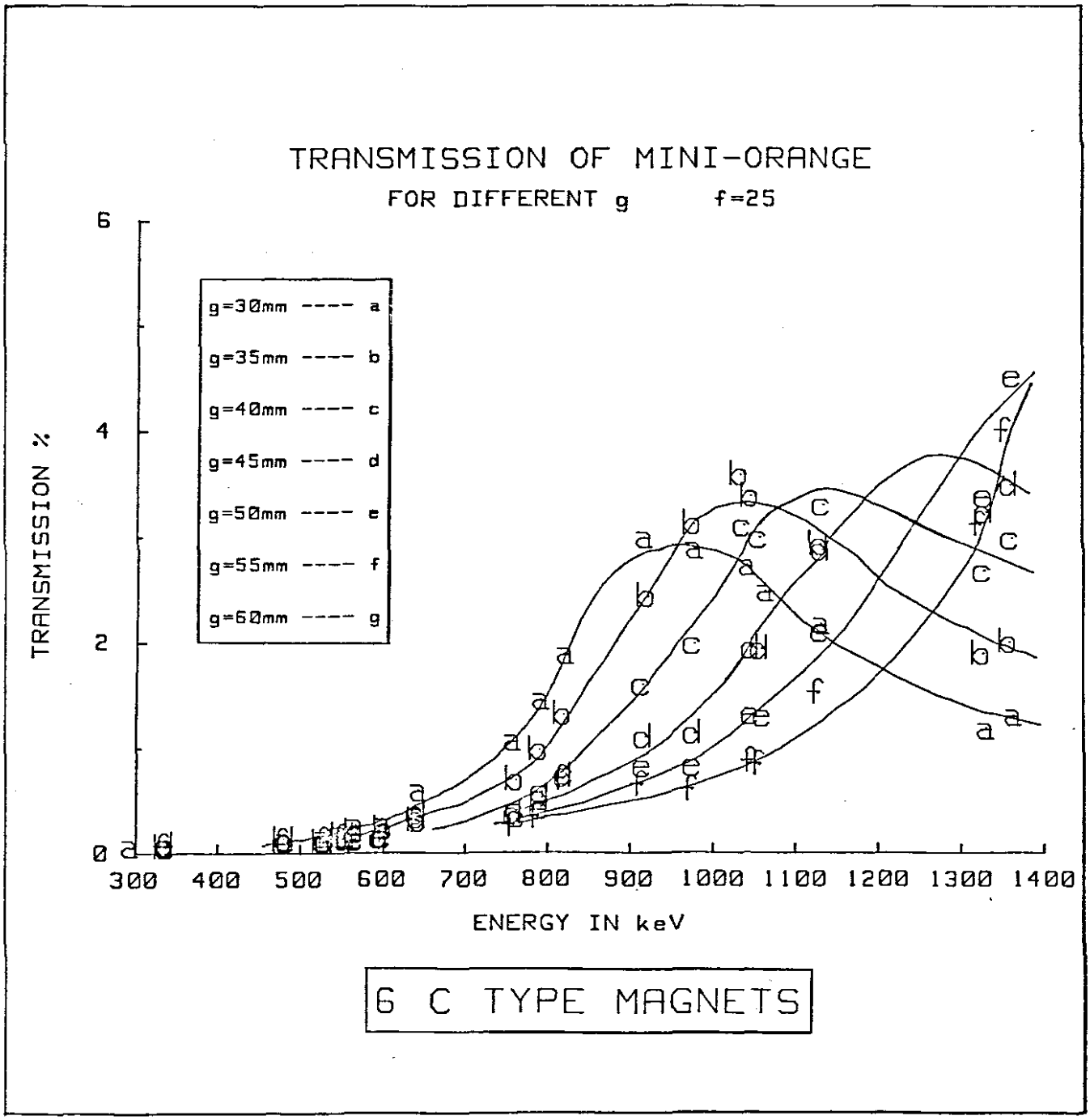

FIGURE 45: Measured transmission curves for 6C type magnets configuration for f = 25. The position of the letters a, b, c, d, e, f indicate experimental values, and the graphs are drawn to guide the eye.

FIGURE 46

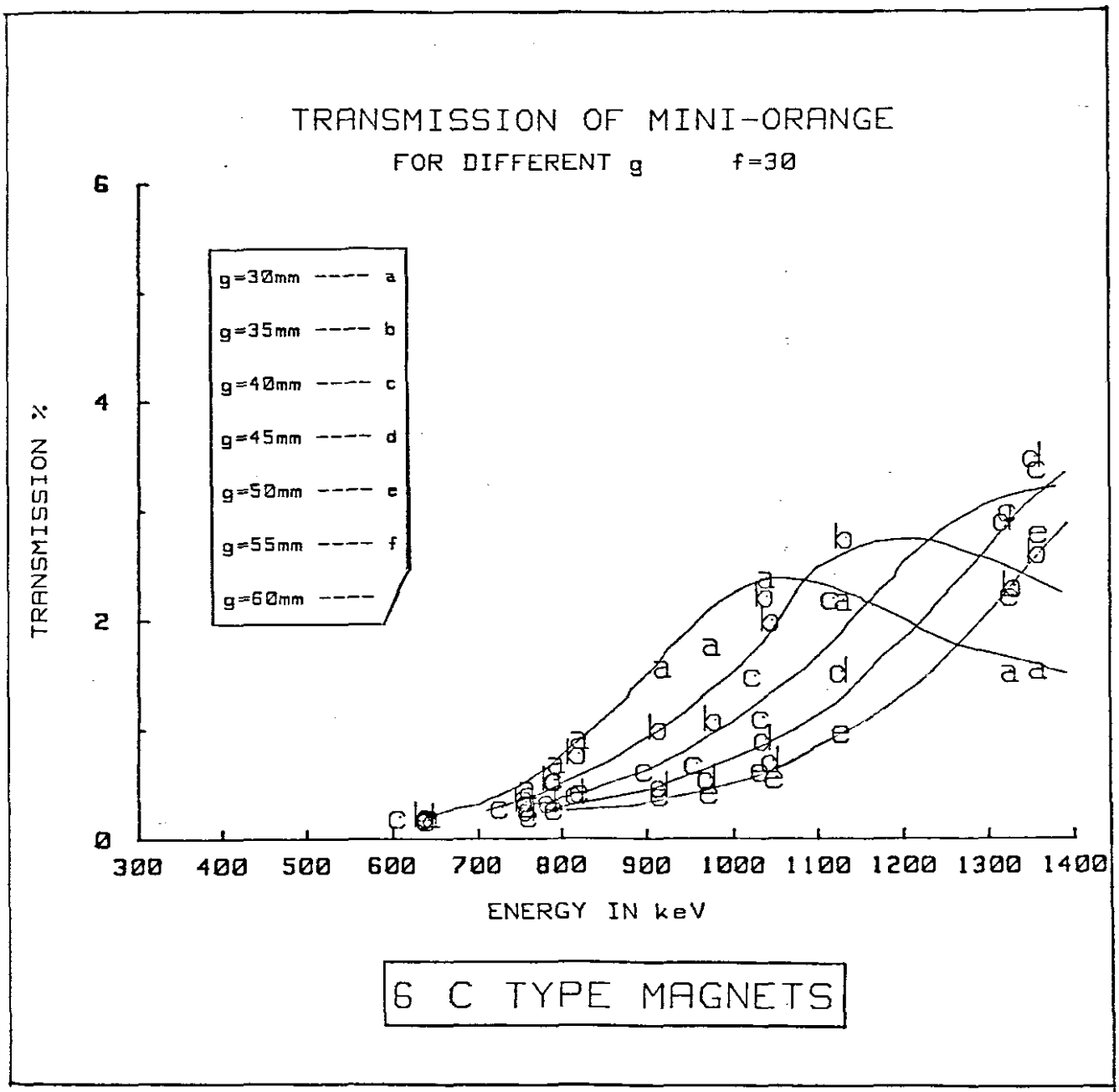

FIGURE 46: Measured transition curves for 6C type magnets configuration for f = 30. The position of the letters a, b, c, d, e, f indicate experimental values, and the graphs are drawn to guide the eye.

FIGURE 47

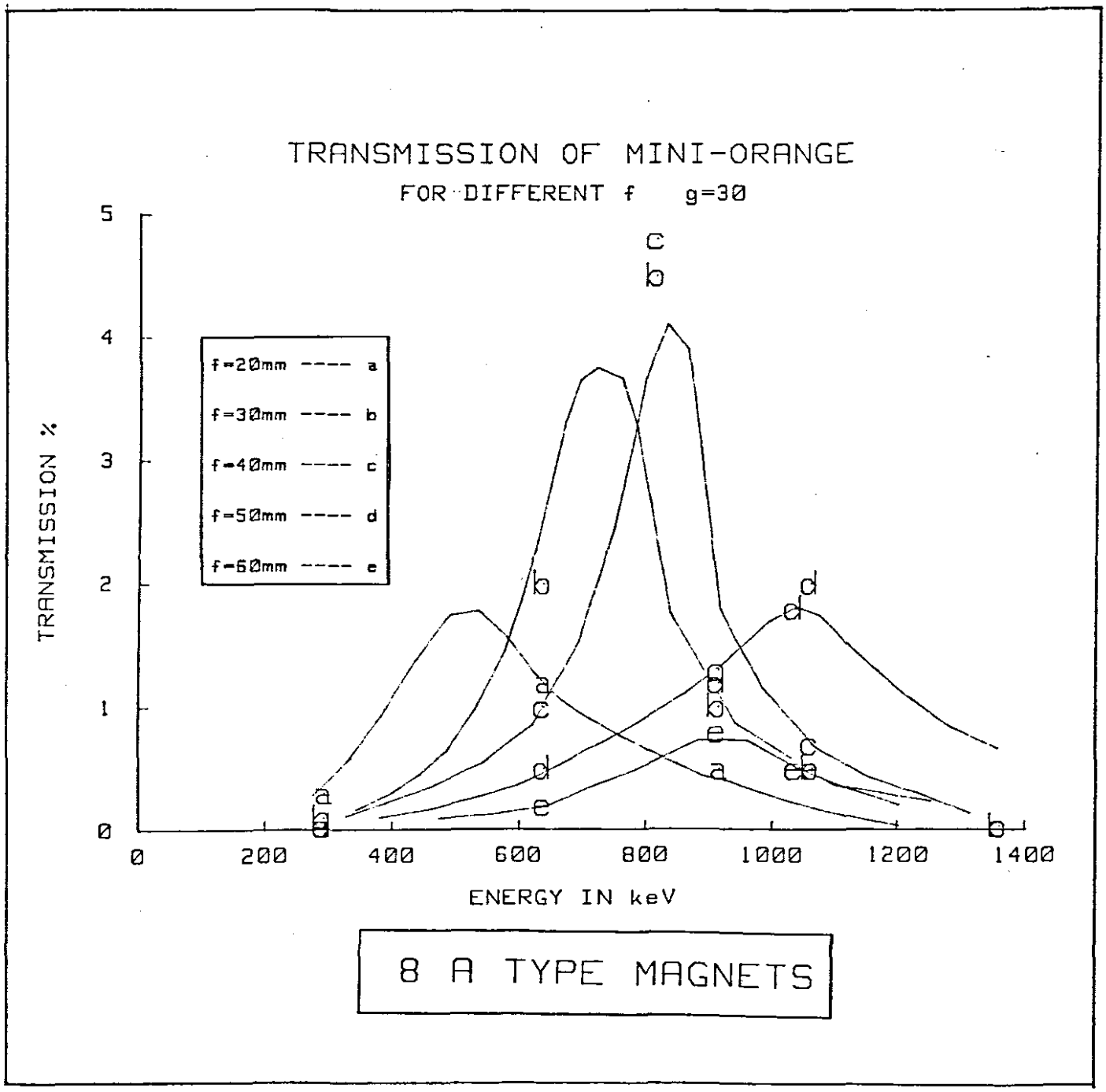

FIGURE 47: Measured transmission curves for 8A type magnets configuration for g = 30. The position of the letters a, b, c, d, e indicate experimental values. The graphs are drawn to guide the eye.

FIGURE 48

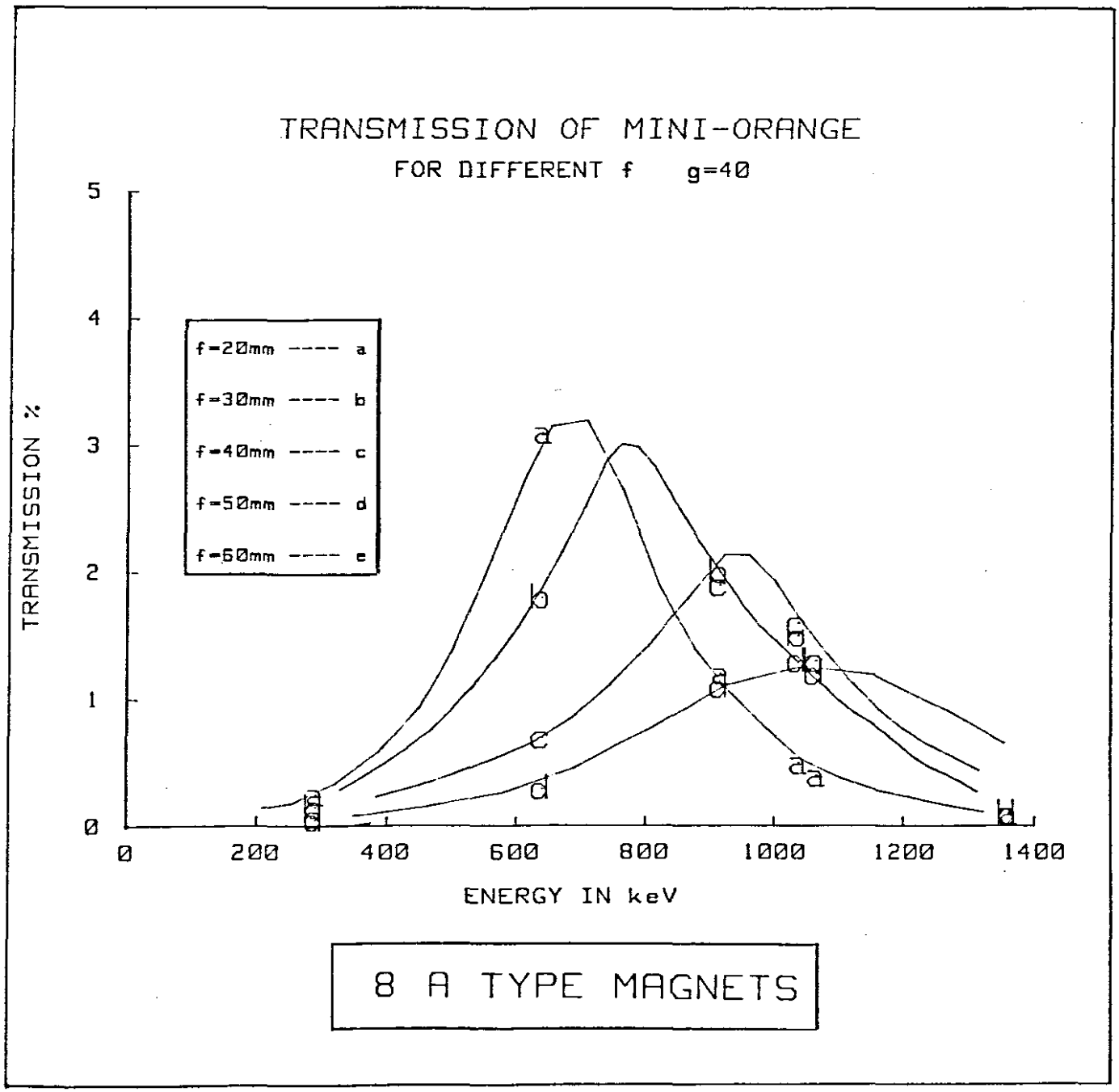

FIGURE 48: Measured transmission curves for 8A type magnets configuration for g = 40. The position of the letters a, b, c, d indicate experimental values. The graphs are drawn to guide the eye.

c) Maximum transmission appear to generally lie at lower energies compared to the 6C type magnets case.

A 4C type magnet configuration with a fixed g = 30, was used to demonstrate the effect of different values of f on the transmission. The 494 keV conversion electrons from a ^{207}Bi source were used. It can clearly be seen that the transmission at 494 keV initially increases as g is increased, it reaches a maximum at f = 20 mm and then gradually decreases.

See figure 49.

General remarks

From these results it is clear that the choice of a suitable transmission curve is not trivial. In all the cases there is a sharp cut-off at the low energy edge, which is useful for elimination β^- background to keep the count rate low (and hence dead time of detector low).

However none of the configurations provides maximum transmission at both 600 keV and 1 200 keV. The configurations with 6C type magnets appeared to be the only feasible option. In order to detect both transitions simultaniously a compromise had to be made, using the 6C configuration with f = 20 mm and g = 35 mm. For this purpose the transmission curves for 6C type magnets were carefully determined.

4.4 Angular distribution and position of detector for in-beam work

In chapter 2 it was pointed out that the angular distribution of conversion electrons emitted from orientated stated is generally not isotropic. When intensities of transitions of different multipolarity are to be compared, it would be essential that the angular distributions are taken into account.

FIGURE 49

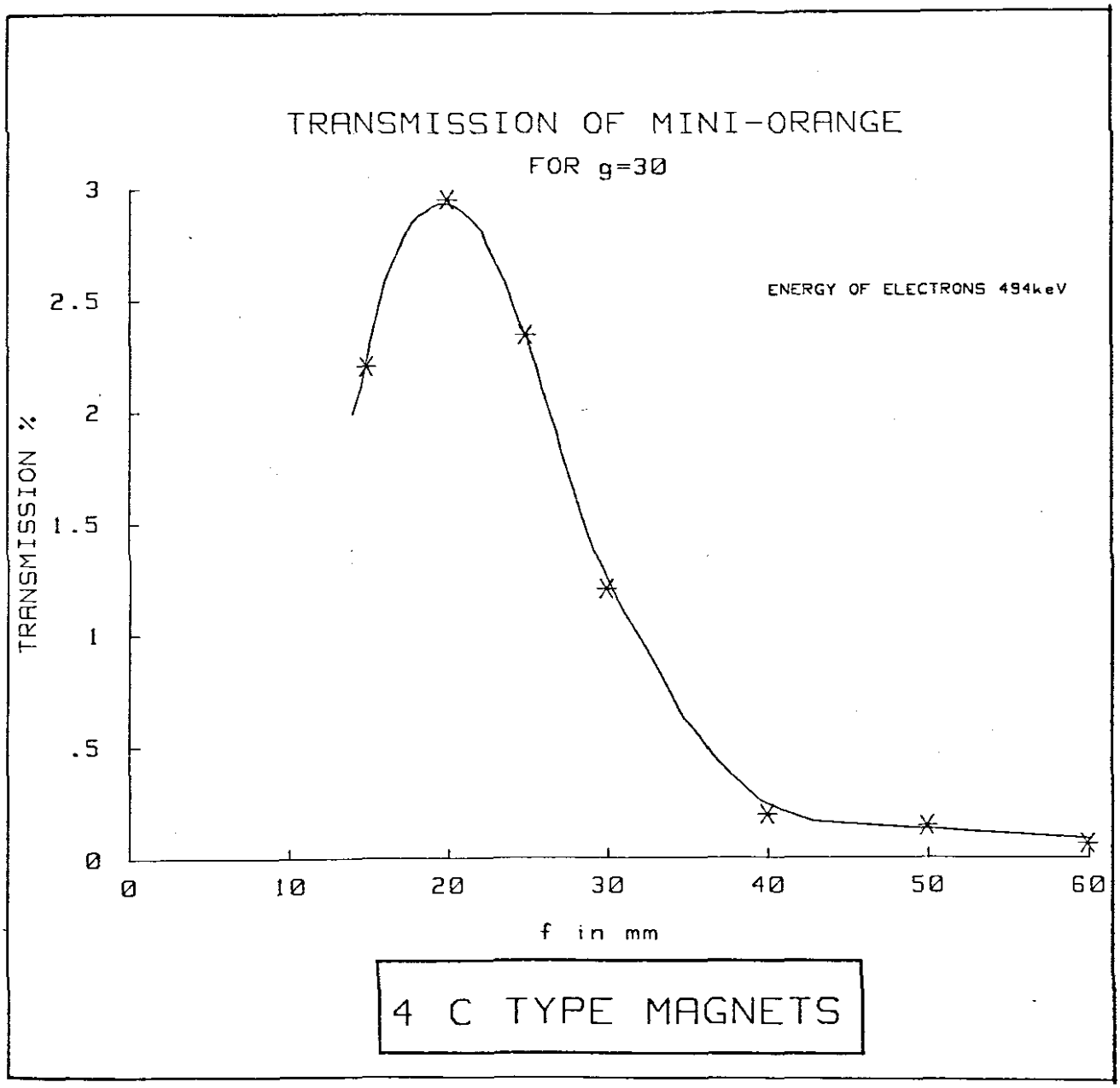

FIGURE 49: Measured transmission of 494 keV electrons using a 4C type maganets configuration for g = 30. Experimental values are indicated and lines drawn to guide the eye.

We recall that for conversion electrons

$$W_e(\theta) = \sum_{k=o}^{\infty} q_k \alpha_k A_k(e) P_k(\cos\theta), \quad k = \text{even}$$

where the symbols used are as defined in section 3.4.

Generally A_2 is substantially larger than A_4 and A_6 for gamma-rays and it is often convenient to terminate the expansion at the second term. This would imply

$$W(\theta) = 1 + q_2 \alpha_2 A_2(e) P_2 \cos\theta$$

At $\theta = \pm 55°, \pm 125°$, $P_2(\cos\theta) = 0$.

Hence if the detector were to be situated at one of these angles with respect to the beamline, the intensities of different transitions would be directly comparable. This can be seen in figures 3, 4, 5 in Chapter 2.

However, as is clear from section 3.4 this simple picture is not generally true for conversion electrons since $A_k(e)$ depend on b_k, the directional particle parameters, and in some cases the argument that $A_2(e) > A_4(e) > A_6(e)$ will not hold. Calculations of $W_e(\theta)$ would then still be necessary. Also from a practical point of view, it would be more convenient to place the detector at $\pm 45°$ or $\pm 135°$ to the beam direction. The backward angle, 135° was chosen to reduce the δ-electron background.

The parameters q_k for the mini-orange spectrometer represents the attenuation of the angular distribution by the finite solid angle between the target or source, and the magnets of the spectrometer.

These parameters q_k are energy dependent since the top angle $\emptyset$ that envelops the trajectories of the electrons that are transmitted varies with energy. The angle $\emptyset$ is the maximum angle with respect to the straight line joining the source and the detector, for which an electron of a particular energy can leave the source and still reach the detector. The angle $\emptyset$ is larger for low energies since these electrons can follow more outward trajectories i.e larger $\emptyset$ and still reach the detector. The attenuation will therefore be larger for higher energies. The attenuation factors q_k can be calculated for a spectrometer and the specific configuration used, by the formula presented by Steffen et al. (Ste 69.)

$$q_2 = 1/2 \cos\emptyset (\cos\emptyset + 1)$$
$$q_4 = 1/8 \cos\emptyset (\cos\emptyset + 1)(7\cos^2\emptyset - 3)$$

Feenstra (Fee 79) calculated these factors for a mini- orange spectrometer for different energies. A table of these values is presented here as typical values.

TABLE 9

ENERGY keV	ATTENUATION FACTOR	
	q_2	q_4
450	0,63	0,17
560	0,65	0,22
790	0,68	0,27
1 050	0,72	0,34
1 300	0,75	0,42
1 550	0,79	0,53

TABLE 9: The attenuation factors q_k as presented by Feenstra (Fee 79)

When the factors q_k and σ/j_i are known from measurements, then the angular distribution $W_e(\theta)$ can be calculated.

In this work however, the two transitions of interest in ^{112}Cd are both transitions where $j_i = 0$. It was pointed out in section 3.4 that such conversion electrons are emmitted isotropically. Hence in this particular case no corrections for angular distributions have to be made; and only the relative transmissions have to be taken into account.

4.5 Vacuum system

To allow sufficient mean free path for the electrons the pressure inside the chamber is held at 10^{-5} Pa. The detector is operated at liquid nitrogen temperature, hence it is essential that the pressure never increases to allow vapours to condense on the surface of the detector and hence damage it. For this reason an oil free turbo-molecular pump, Pfeiffer TPU 170 was used, together with a liquid nitrogen trap to keep the chamber vapour free. A rotary pump provided the forevacuum. In the case where the chamber was opened, the detector could be withdrawn and a valve closed to isolate the cooled detector. The main valve could then be closed and the chamber could be opened to air, for experimental adjustments.

FIGURE 50

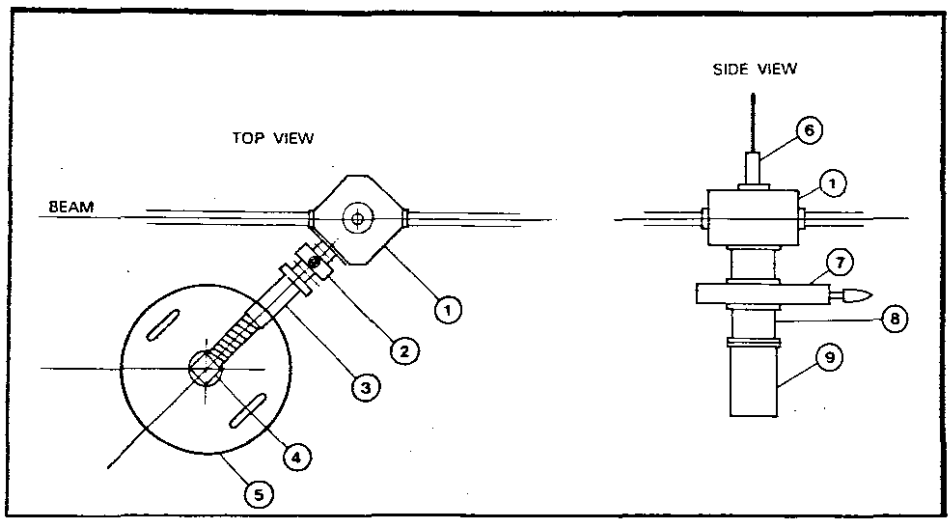

FIGURE 50: Arrangement of the vacuum system in the beam line. The parts shown are:

1) Vacuum chamber,
2) valve,
3) telescopic adjustment of detector,
4) cold finger,
5) Liquid nitrogen dewar,
6) target ladder system,
7) valve,
8) liquid nitrogen trap, and
9) turbo-molecular pump.

(Spo 84)

CHAPTER 5

THE ^{112}Cd EXPERIMENT

5.0 The experiment

Internal conversion electrons from an excited ^{112}Cd nucleus were detected using the mini-orange spectrometer. The excited ^{112}Cd nucleus was produced by bombarding a ^{112}Cd foil with 12 MeV protons.

5.1 The $0_1^+ \rightarrow 0_g^+$ transition of ^{112}Cd

The experiment was performed to determine the ratio X(E0/E2) and ρ^2(E0) for the deexcitation of the first 0^+ excited state in ^{112}Cd. This was done in order to obtain information about the structure of the nucleus of ^{112}Cd which can not be obtained by gamma-ray measurements. A further discussion about the relation between the ratio X(E0/E2), ρ^2(E0) and the structure of the nucleus, is presented in section 3.2.1 and section 6.1.

5.2 Properties of ^{112}Cd

The $^{112}_{48}Cd_{64}$ isotope is one of the 8 stable Cd isotopes. All the even-even nuclei like ^{112}Cd are of particular interest since they have low lying 0^+ excited states from which $0_1^+ \rightarrow 0_g^+$ E0 internal conversion transitions take place. As mentioned before, such E0 transition rates are important for the determination of ρ^2(E0), the monopole matrix element which yields valuable information about nuclear structure.

The Cadmium even-even nuclei are of special interest since while the lowest four excited energy levels $j^{\pi} = 2_1^+$, 0_1^+, 2_2^+, 4_1^+ are in qualitative agreement with the prediction of a spherical vibrational model, there are additional $j^{\pi} = 0^+$, 2^+ intruder states just above the $j^{\pi} = 4_1^+$ state. (Sam 81)

FIGURE 51

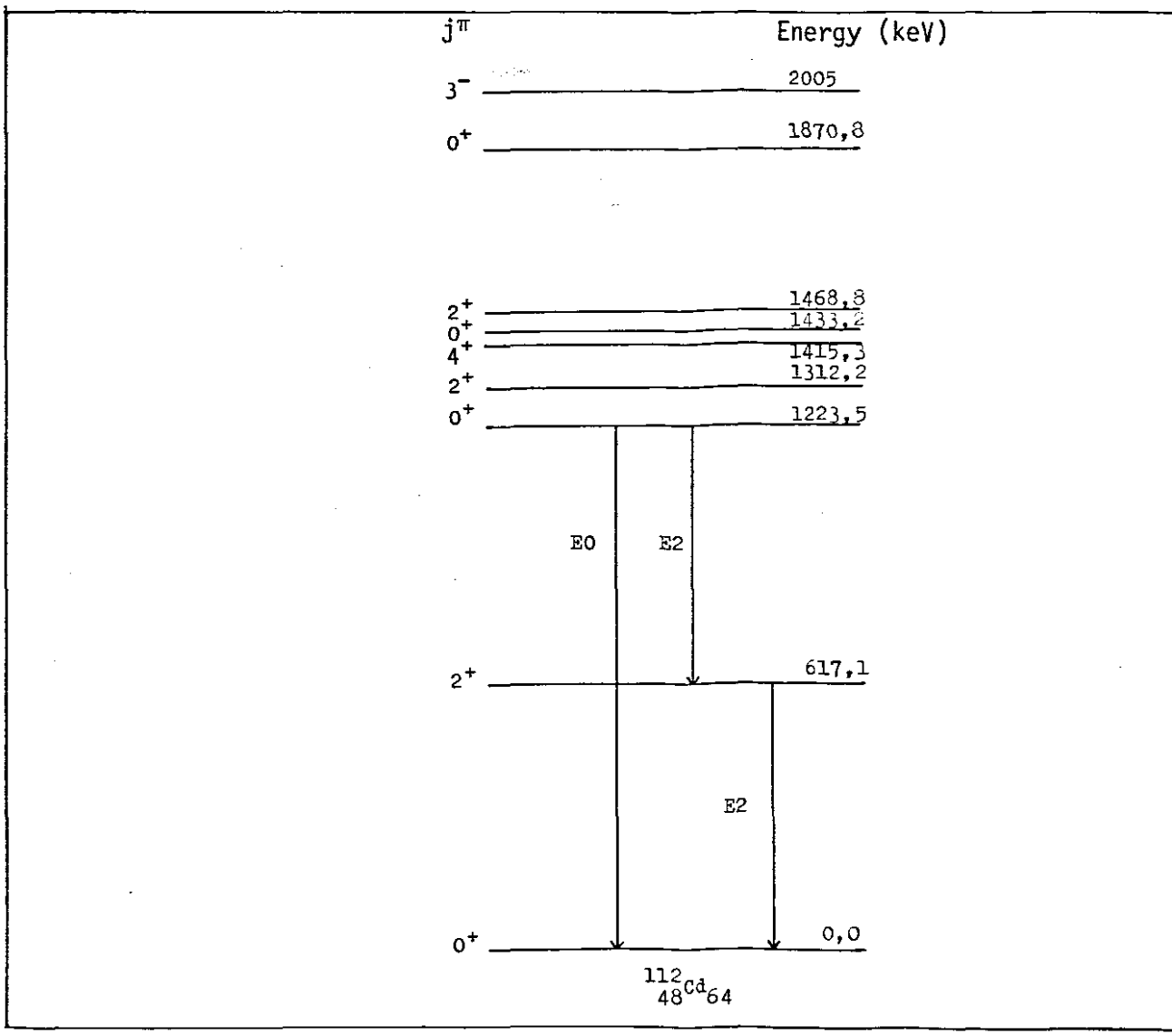

FIGURE 51: Energy level scheme of ^{112}Cd.

5.3 The $^{112}Cd(p,n)^{112}In$ reaction

For the production of excited ^{112}Cd nuclei several reactions were considered. Only reactions with Q values such that the required projectile energies can be achieved with the 6 MV Tandem Van der Graaf accelerator, were considered.

Reactions where ^{112}Cd is the direct product nucleus such as $^{110}Pd(\alpha, 2n)^{112}Cd$, $^{110}Pd(^{3}He,n)^{112}Cd$, $^{112}Cd(p,p)^{112}Cd$ and $^{111}Cd(d,n)^{112}Cd$ have the disadvantage that the measurement of an internal conversion spectrum would have to be taken during the time the beam is on, with neutron, δ-electron and higher gamma-ray backgrounds present. Also an α-particle brings in significant amount of angular momentum and higher angular momentum states would be populated rather than 0^+ states.

More attractive alternatives were considered, where the radioactive precursor of ^{112}Cd is produced. (See figure 52). From the figure it is clear that producing either ^{112}Ag or ^{112}In by reactions such as $^{100}Ag(\alpha,n)^{112}In$, $^{110}Pd(^{3}He,n)^{112}Ag$ (And 77) or $^{112}Cd(p,n)^{112}In$, would solve both problems previously mentioned. The ^{112}Ag ground state decays solely by β^-- decay to ^{112}Cd with a half life of 3,14 hr (NDS 80, NDS 72, Wal 72, Mac 70) and ^{112}In decays by β^--decay to ^{112}Sn ground state and by β^+-decay and electron capture to ^{112}Cd with half-life of 14,4 m.(NDS 80, NDS 72)

This implies that it would be possible to produce ^{112}In or ^{112}Ag in the beam and then interupt the beam and proceed to collect the internal conversion spectrum of ^{112}Cd without interference from the beam and background radiation from other subsequent short lived reaction products.

FIGURE 52

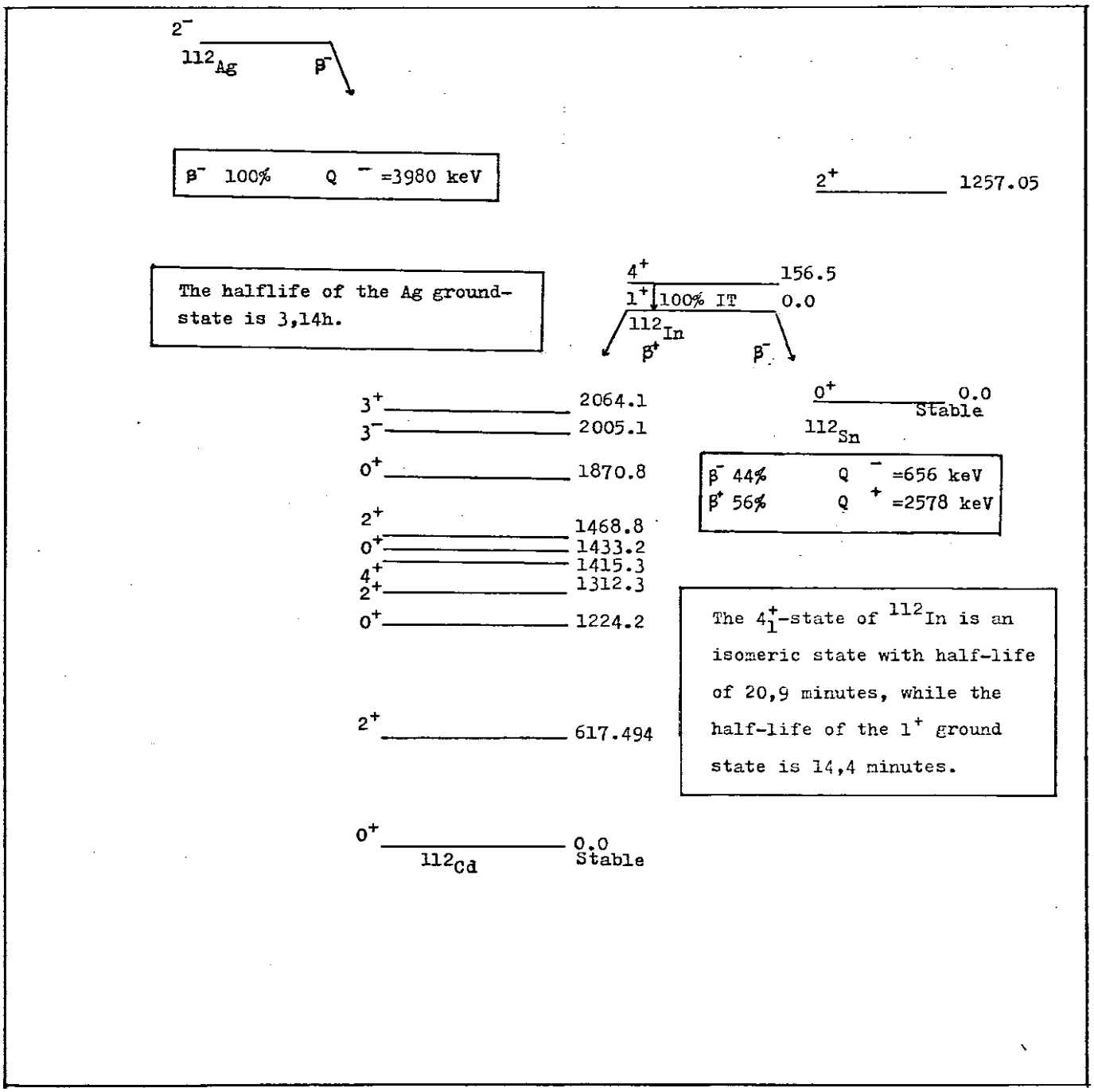

FIGURE 52: The decay schemes of ^{112}Ag and ^{112}In producing the product nucleus ^{112}Cd.

The reaction $^{112}Cd(p,n)^{112}In$ was chosen because of the simplicity of the reaction and the availability of ^{112}Cd from with isotopic purity of 97,05 % from Oak Ridge National Laboratory. For the reaction $^{112}Cd(p,n)^{112}In$ the Q-value is -3,37 MeV (NDT 72). A proton beam energy of ±11 MeV was used, assuming (Kap 64) that the maximum cross-section for the (p,n) reaction is maximum at proton energy just below the Q value for the (p,2n) reaction. [Q(p,2n) = -11,003 MeV (NDT 72)]. At this energy the (p,n) reaction is the dominant reaction, the other reactions are negligible (Kap 64) and the alternative reaction products are stable (NDS 81, NDS 77, NDS 71). The only slight interference which could be expected after long periods of irradiation is from the 391,691 keV isomeric transition ($T_{½}$ = 1,658 hr) from the first excited state of ^{111}Cd (NDS 81). All the electromagnetic transitions from the other reaction products have short halflives compared to the 5 min interval chosen by us between irradiation and spectrum recording. Other possible reactions are:

$^{112}Cd(p,\gamma)^{113}In$	Q = 6,054	MeV
$^{112}Cd(p,d)^{111}Cd$	Q = -7,1723	MeV
$^{111}Cd(p,t)^{113}Cd$	Q = -7,8916	MeV
$^{112}Cd(p,^{3}He)^{109}Ag$	Q = -10,7639	MeV
$^{112}Cd(p,\gamma)^{109}Ag$	Q = +3,0088	MeV.

As seen in figure 52, ^{112}In decay not only produces ^{112}Cd by β^+ decay and electron capture, but also ^{112}Sn by β^- decay. Fortunately the latter process is only 44 % of the ^{112}In decay and the decay is directly to the ground state of ^{112}Sn implying that there will be no contribution by the transitions of the ^{112}Sn to the observed spectrum.

Also for the β^- decay Q = 656 keV (NDS 80) hence β^- interference in the spectrum will only be to maximum energy of 656 keV. This is one advantage over using the reaction where ^{112}Ag is produced because ^{112}Ag β^- decay to ^{112}Cd where Q = 3,96 MeV, implying that the spectrum would be swamped by the β^- background.

In the β^+, electron capture decay of ^{112}In to ^{112}Cd, β^+ decay is 24 % of the process (Ble 53). In this experiment the magnetic filter defocusses β^+ and hence β^+ would not reach the detector.

5.4 Transition Energies

For $0_1^+ \rightarrow 0_g^+$ transition of ^{112}Cd the transition energy is 1224,23 keV, and 617,494 keV and 606,736 keV for $2_1^+ \rightarrow 0_g^+$ and $0_1^+ \rightarrow 2_1^+$ transitions respectively. (NDS 80).

In this experiment the value of 26,711 keV was used as the binding energy of the K-shell electron in ^{112}Cd. (Rös 78, Has 66), so that the energies of the conversion electrons were 1197,52 keV 590,783 keV and 580,025 keV respectively.

5.5 Preparation of the ^{112}Cd Target

Several methods were considered to prepare a 1 mg/cm^2 ^{112}Cd foil.

Rolling of a natural Cd metal into a foil of 1 mg/cm^2 proved to be fairly successful and is a method used and suggested to us by Dr. Westerberg from the Accelerator Centre Uppsala in Sweden (Wes 83). However isotopically pure ^{112}Cd could only be obtained in oxide form (CdO) from Oak Ridge National Laboratory USA.

Reduction of CdO in H_2 atmosphere was found to be a difficult process since Cd is very volatile. At the temperature where reduction takes place, the Cd immediately evaporates. The possibility of producing the foil by evaporating and condensation was henceforth also considered, but high losses of precious ^{112}Cd would occur.

The method of electroplating was finally used as described by L. Yaffe. (Yaf 62). The Cd^{++} was electroplated from a $Cd(CN)_2$ solution onto a thin aluminium cathode, using a carbon anode. The solution was prepared by desolving 80 mg KCN, 20 mg CdO, 30 mg Na_2CO_3, in the given order, in 10 ml distilled water, and 2 drops of glycerine were added. A constant current of 2,5 mA/cm^2 was maintained. After a predetermined time the aluminium cathode was removed from the solution. If the current is not properly controlled, and is allowed to rise above $3mA/cm^2$, the production of H_2 at the cathode becomes considerable, and the bubbles of H_2 give rise to uneven plating of Cd onto the aluminium foil.

It is imperative to allow the foil to dry before it is attempted to lift the Cd foil from the Al. The Cd foil of 1 mg/cm^2 is very fragile and water surface tension or the weight of a drop of water can easily ruin the foil. The edge of dried foil was carefully seperated from the Al with a sharp blade, and the rest of the Cd foil then easily peels off.

The foils were mounted on aluminium frames and fitted into the target ladder. Several foils were made from the same solution and 70 % of the CdO was retained as Cd metal in this way. These 1 mg/cm^2 foils suffered no damage when bombarded with 10 MeV protons at current of 40 nA for 4 hours.

To predetermine the thickness of the foil to be plated onto the aluminium, the following has to be considered:

Let a be the area of the foil in cm^2 and d be the required thickness in mg/cm^2, then the mass m to be deposited is $m = 2ad \times 10^{-3}$ [g] since both sides of the aluminium cathode is plated. The required current, I will be $I = 2,5$ [mA/cm^2] x a[cm^2], and the time t needed to plate the required thickness is:

$$t = \frac{2emN_A}{112\,[g.mol^{-1}]I} \qquad \ldots 5.5.1$$

with: $e = 1{,}6 \times 10^{-19}$ C
m = mass required in gram,
$N_A = 6{,}02 \times 10^{6}$ mol^{-1}.

Table 10

ISOTOPIC ANALYSIS OF TARGET	
ISOTOPE	ATOMIC %
106	0.01
108	< 0.01
110	0.21
111	0.73
112	97.05
113	0.93
114	0.99
116	0.09

TABLE 10: The isotopic composition of the CdO as supplied by Oak Ridge laboratory.

5.6 Experimental Arrangement

The mini-orange spectrometer was connected to the beam-line of the 6 MV Tandem Van der Graaf accelerator at Witwatersrand University Nuclear Physics Research Unit (NPRU).

The geometry was such that the detector was at 135° to the beam direction.

The following procedure was adopted.

a) A quartz target (for determining beam focus) and the ^{112}Cd foil was inserted into the target ladder.
b) A magnet configuration of 6 C type magnets was used spaced slightly asymmetrically as indicated in fig. 35 at a position f = 20 mm from the target position. It was indicated in section 4.7 that this configuration would be the most suited for this experiment.
c) The target ladder was adjusted to have the quartz target in the beam-line, so as to collimate the beam properly.
d) The ^{112}Cd target was then placed in the beam-line, and using an 11 MeV proton beam of 40 nA, the target was bombarded for about 30 min. During this procedure the detector was retracted to protect the detector from unneccesary radiation damage by neutrons and other reaction products.
e) The detector was placed at g = 35 mm position and the bias voltage of the detector was applied. For 30 min a spectrum was collected. The procedure d), e) was repeated several times until the neccesary statistics were obtained in the peaks under investigation.

CHAPTER 6

THE ^{112}Cd SPECTRUM AND PROCESSING OF RESULTS

6.0 Experimental results

The details of the experimental results and their processing to obtain values for $\rho^2(E0)$ and $X(E0/E2)$ are discussed. A typical conversion electron spectrum, resulting from a total of 3 hr accumulation of data, is presented in figures 53 and 54.

From the spectrum the intensity of the E0 1224,23 keV transition K shell conversion electrons as well as the intensity of the E2 606 keV transition K shell conversion electrons was determined. The areas of the peaks were determined by hand and the background was subtracted.

6.1 Calculation

It was shown in paragraph 3.2.1 that

$$\rho^2(E0) = \frac{q^2 \alpha_k(E2) T_\gamma(E2)}{\Omega_k} \qquad \text{and}$$

$$X(E0/E2) = \frac{2{,}53 \times 10^9 A^{4/3} q^2 \alpha_K(E2) E_\gamma^5}{\Omega_K}$$

with the symbols as defined in paragraph 3.2.1.

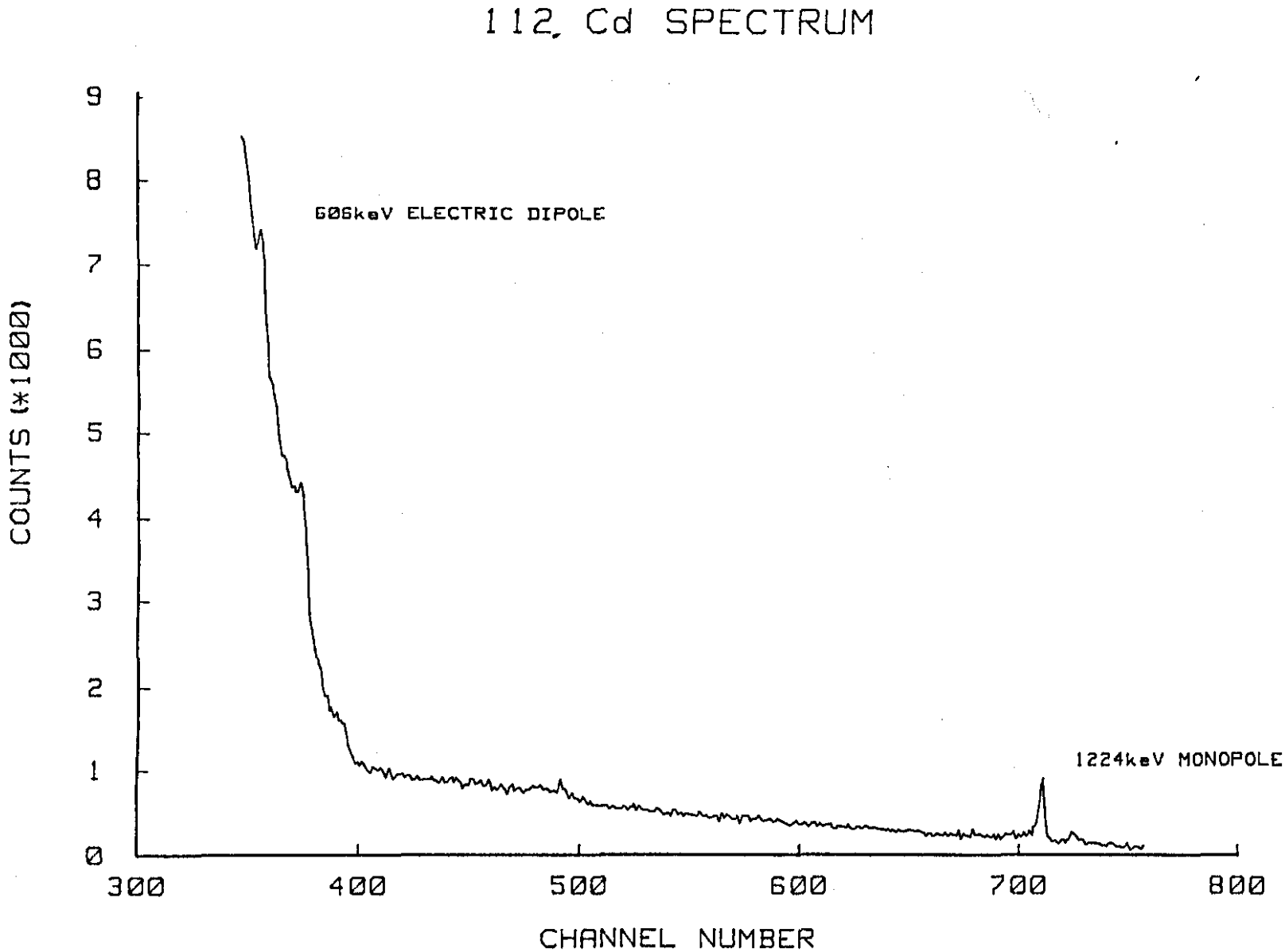

FIGURE 53

FIGURE 53: The recorded ^{112}Cd internal conversion electron spectrum.

FIGURE 54

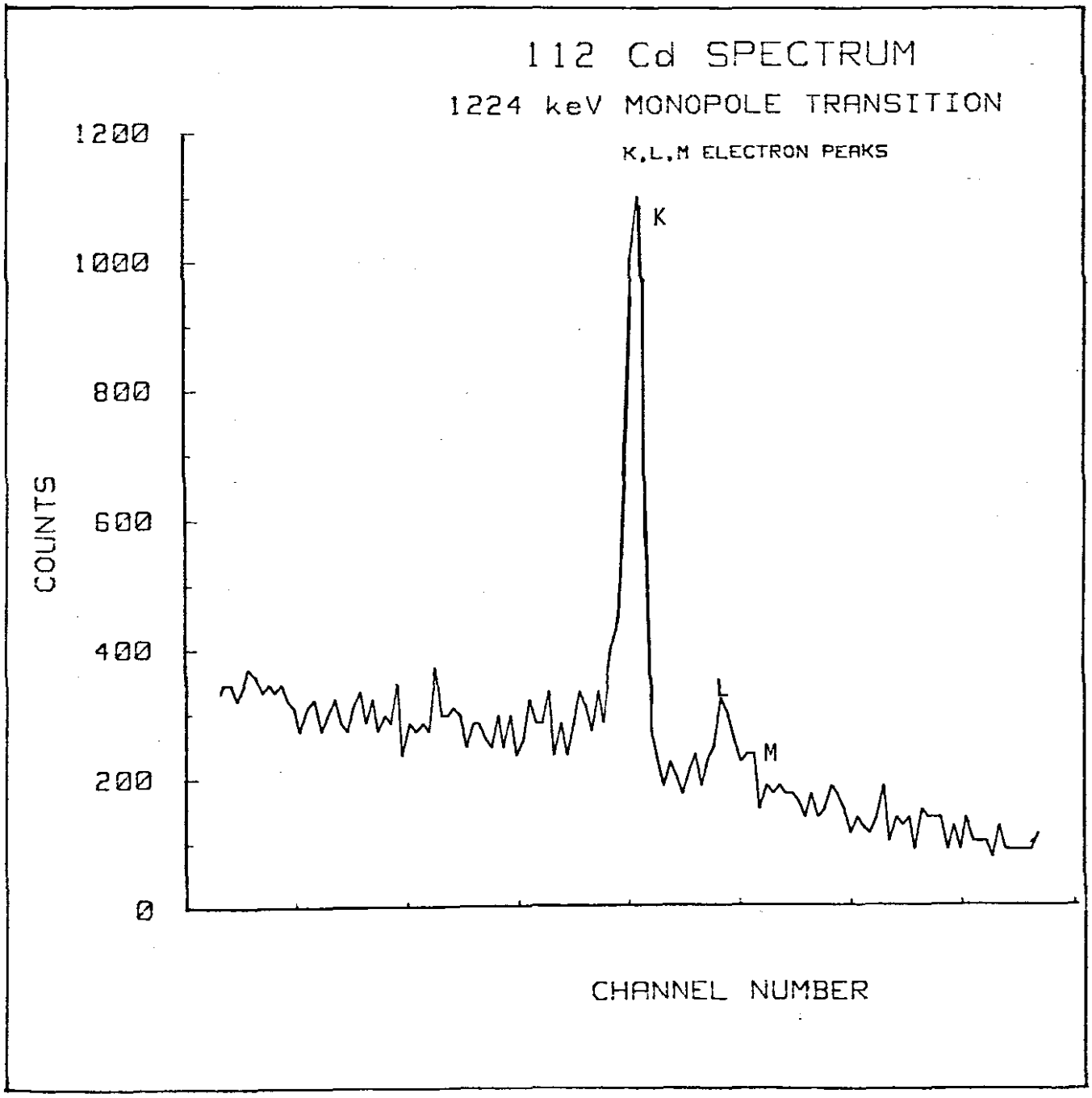

FIGURE 54: The recorded $0_1^+ \rightarrow 0_g^+$ E0 transition in ^{112}Cd.

A Transmission ratios

In order to obtain the ratio

$$q^2 = \frac{T_k(E\ 0)}{T_k(E\ 2)} \qquad \ldots 6.1.1$$

the measured intensities must be corrected for the relative transmission of the spectrometer at the two energies.

$$\text{Hence } q^2 = \frac{T_K(E0)}{T_K(E2)} = \frac{I_K(E0)}{I_K(E2)} \times \frac{t(E_K(E2)}{t(E_K(E0)} \qquad \ldots 6.1.2$$

where $I_K(E0)$ is the measured intensity of the K-shell E0 electrons

$I_K(E2)$ is the measured intensity of the K-shell E2 electrons

and $t(E_K(E0)$ is the transmission in % at $E_K(E0) = (1224 - B_K)$ keV

$t(E_K(E2)$ is the transmission in % at $E_K(E2) = (606 - B_k)$ keV,

and B_K is the binding energy of the K-shell electron.

For ^{112}Cd B_K = 26,711 keV; hence $E_K(E0)$ = 1 197,51 keV and $E_K(E2)$ = 580,025 keV. In the experiment 6C type magnets were used with f = 20 mm and g = 35 mm. The transmission curve for this configuration is presented in figure 55. From the graph the ratio $t(E_k(E2))/t(E_k(E0))$ was determined to be 0,20 ± 0,01.

See figure 55

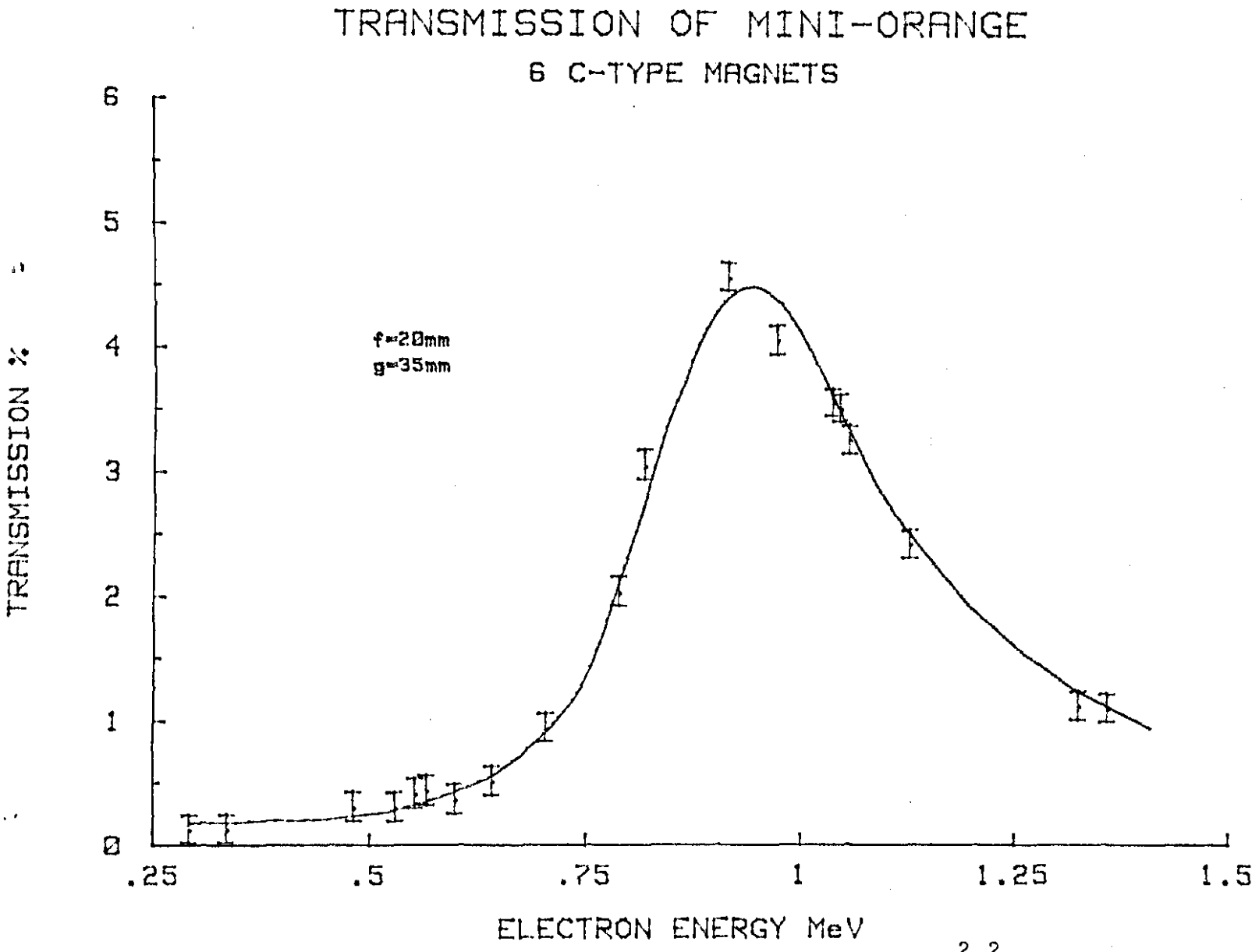

FIGURE 55: The transmission curve. A fit of the type $\frac{cxe^{-d^2x^2}}{(x-a)^2+b^2}$ was used.

FIGURE 55

B Conversion Coefficients

From figure 53 it can be seen that it is difficult to determine the intensity of the K-shell internal conversion electrons for the 606 keV $0_1^+ \rightarrow 2_1^+$ transition, since the peak partly overlaps with the tail of the conversion electron peak for the 617 keV $2_1^+ \rightarrow 0_g^+$ transmition. The intensity of the K-electrons from the 606 keV transition was deduced making use of the known intensity ratio P(617/606) of the 606 and 617 keV gamma lines and from the ratio Q (617/606) of the respective conversion coefficients $\alpha_K(606)$ and $\alpha_K(617)$. For ^{112}In decay the ratio is given as P(617/606) = 5,0/1,19 (NDS 80)

By interpolation of tabulated values of α_K from ref (Hag 68) the values of $\alpha_K(606)$ and $\alpha_K(617)$ were determined.

FIGURE 56

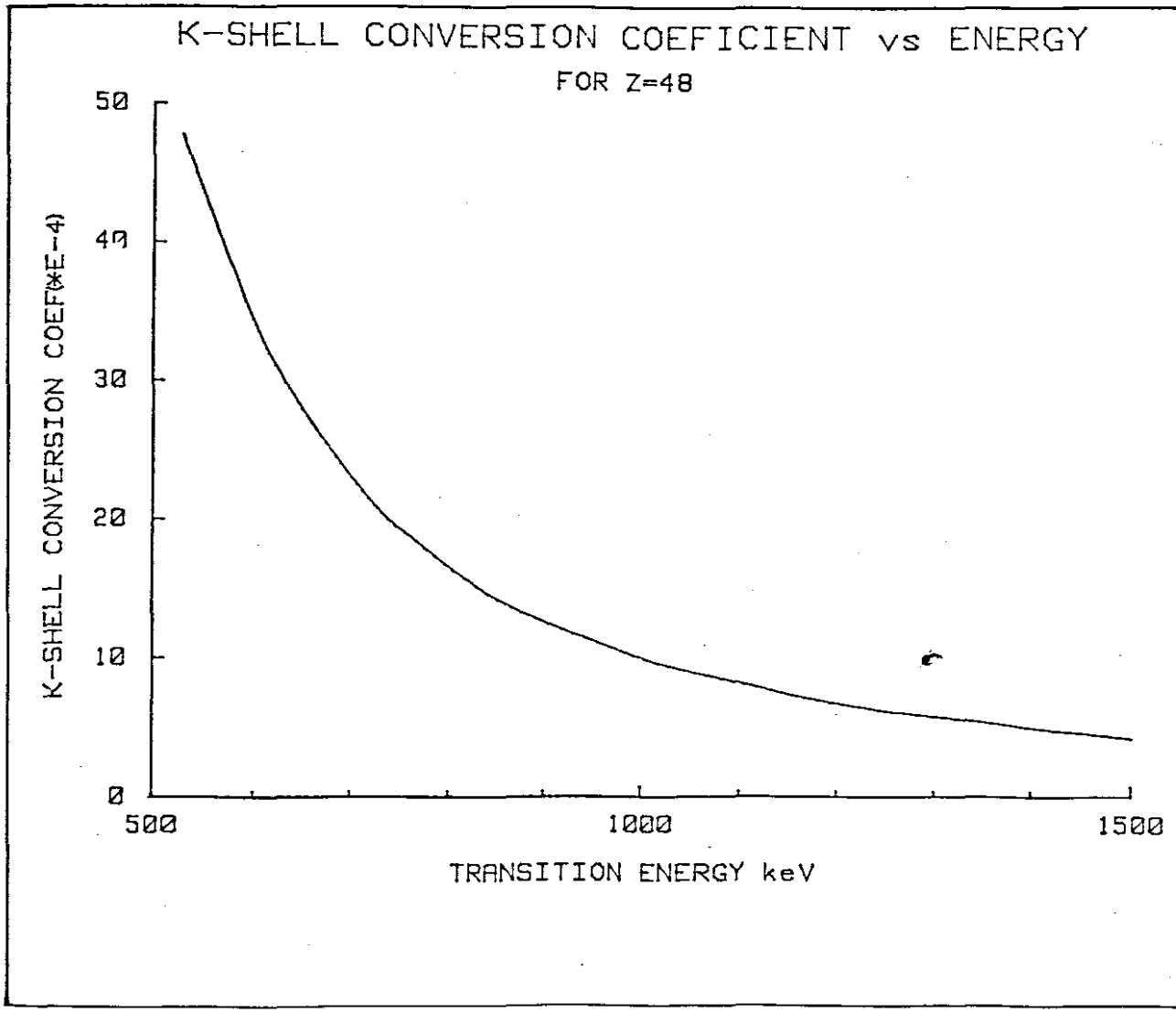

FIGURE 56: The E2 K-shell conversion coefficient vs energy for ^{112}Cd (Z = 48)

From this interpolation the values
$\alpha_K(606)$ = 3,369 x 10^{-3} , and
$\alpha_K(617)$ = 3,217 x 10^{-3} were determined, giving a ratio of Q(617/606) = 0,9549.

For a typical measurement the intensity ratio R(617/606) of the conversion electrons from the 606 keV and 617 keV transitions was then determined to be R(617/606) = 4,01 and the total number of counts in the combined peak to be 7584.

Hence

$$I_K\ (E2, 0_1^+ \rightarrow 2_1^+) = 1514$$

C The E0 transition

For the E0 transition $0_1^+ \rightarrow 0_g^+$ at 1 224 keV, the peak is well defined and the intensity can be determined directly. It was found that in the example given $I_K(E0, 0_1^+ \rightarrow 0_g^+) = 2119$. From eq. 6.2.2 we get the value of q^2.

$$q^2 = \frac{2119}{1514} \times 0{,}20 = 0{,}27 \pm 0{,}05.$$

It should be noted that no correction for different angular distributions have to be made in this particular case, because the transitions involved are the deexcitation of the $j_i^\pi = 0_1^+$ state, and as was pointed out before, such a state can not be orientated.

It was shown in paragraph 3.2.1

$$\text{that } q^2 = \frac{T_K(E0)}{T_\gamma(E2)\,\alpha_K} \qquad 6.1.3$$

From eq's 3.2.7 it follows that:

$$\rho^2(E0) = q^2\ \frac{\alpha_K 1{,}221 \times 10^9 E_\gamma^5\ B(E2, 0^+ \rightarrow 2^+)}{\Omega_K}\ . \qquad 6.1.4$$

D The reduced transition probability B(E2)

The reduced transition probability B(E2) can be obtained by Couloumb excitation experiments (Alb 68). The first excited 0^+ level (0_1^+ in even-even vibrational nuclei, as ^{112}Cd) are excited in double Coulomb excitation with heavy ions. (Jul) In such experiments the reduced upward transition probability $B(E2)\uparrow$ is obtained (Ven 61). It is related to the downward reduced transition probability $B(E2)\downarrow$ by the following relation:

$$B(E2, j_i \to j_f)\downarrow = B(E, 2j_f \to j_i)\uparrow \times g$$

where $g = (2j_f+1)/(2j_i+1)$ ref. (Ble 53)

In this experiment the value for $B(E2, 0_1^+ \to 2_1^+)$ was taken to be 51 $\pm$ 13 Wu. This value is the average obtained from results of several experimental groups. (Jul, Hey 82, Sam 81, Jul 80).

In this case 1 Wu = $B(E2)_W = \frac{(1,2)^4}{4\pi}(\frac{3}{5})^2 A^{4/3}$ in e^2fm^4 units (see eq.2.3.2) Substituting A = 112 one obtains

$$B(E2)_W = 32,1\,[e^2fm^4].$$

Hence $B(E2) = 51 \times B(E2)_W = 1637\ [e^2fm^4]$.

The total transition probability $T_\gamma(E2)$ can thus be calculated using E_γ = 0,606 MeV

giving $T_\gamma(E2) = 1,63 \times 10^{11}\ s^{-1}$

E The Electronic Factor

The electronic factor Ω_K was obtained by interpolation of tabulated values of $A_K(E0)$ from Hager and Seltzer (Hag 69)

$$\Omega_K = 8\pi\alpha k \frac{mc^2}{\hbar} A_K(E0)$$

where α is the spectroscopic factor = 1/137 and k is the transition energy in mc^2 units, and in this case k = 2,389 $[mc^2]$.

FIGURE 57

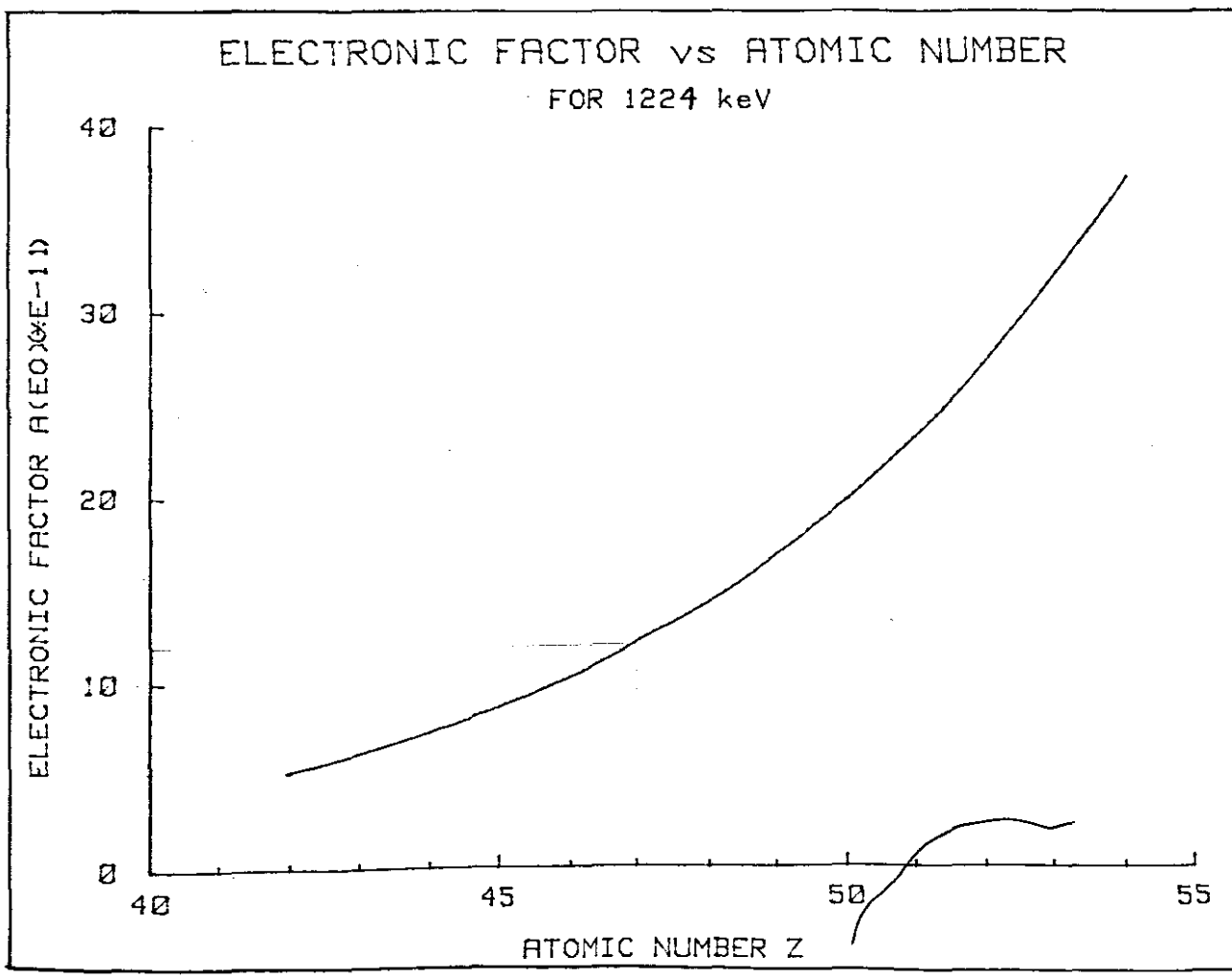

FIGURE 57: The electronic factor $A_K(E0)$ vs the atomic number Z for a 1224,23 keV transition.

The value of A(EO) obtained for the 1224,23 keV transition in ^{112}Cd was $A_K(EO) = 1,424 \times 10^{-11}$. Hence $\omega_K = 4,85 \times 10^9\ s^{-1}$. Tabulated values from Bell et al (Bel 70) were also interpolated and a value $\omega_K = 4,88 \times 10^9 s^{-1}$ was obtained. These values differ from each other by an amount smaller than the error on interpolation. For the calculation the latter value was used, being the more recent value.

FIGURE 58

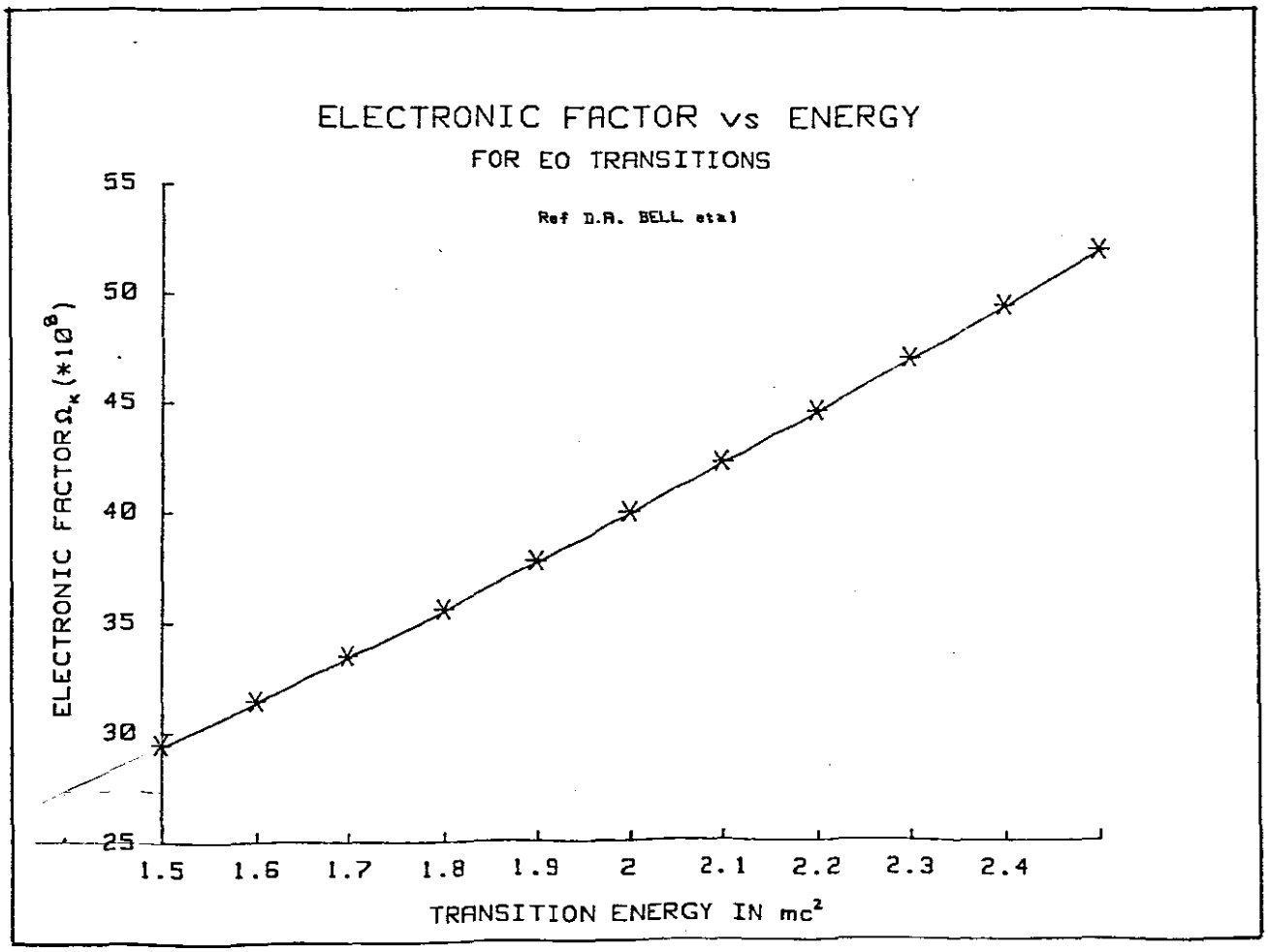

FIGURE 58: The electronic factor ω_K for Z = 48 vs transition energy.

F The factors $\rho^2(E0)$ and X(E0/E2)

Using the above mentioned values a value of $\rho^2(E0) = 30 \pm 9 \times 10^{-3}$ was obtained. This result compares favourably with results quoted elsewhere.

TABLE 11

	This work	Ref. Ohy 80	Ref Jul 80
$\rho^2 \times 10^3$	30(9)	26(5)	37(11)

TABLE 11: The experimentally determined monopole matrix element $\rho^2(E0)$ of this work was compared to the values obtained by other groups. The figures in brackets represent the standard deviation values.

Sometimes it is prefered to quote $T_{\frac{1}{2}}(E0)$, the so-called E0 partial half-life.

$$T_{\frac{1}{2}}(E0) = \frac{\ln 2}{T_e(E0)} = \frac{\ln 2}{\rho^2(E0)\ \Omega_K}$$

Hence in this experiment $T_{\frac{1}{2}}(E0) = 4{,}76 \times 10^{-9}$ s.
A ratio which is also important for comparison with nuclear structure models is

$$X(E0/E2) = \frac{B(E0, j_i \to j_f)}{B(E2, j_i \to j_f)} \qquad \ldots 6.1.8.$$

$$= \frac{q^2 \alpha_K E_\gamma^5}{\Omega_K} \ 2{,}53 \times 10^9 \ A^{\frac{3}{4}}$$

(see eq. 3.2.11)

The value obtained in this experiment was X(E0/E2) = 0,0209. This value compares favourably with other results, as is indicated in Table 12.

TABLE 12

	This work	ref. (Ohy 80)	ref. (Jul 80)	ref. (Gia 79)
X(E0/E2)	0,021(4)	0,033(4)	0,026(5)	0,025(3)

TABLE 12: The ratio X(E0/E2) as obtained in this work compared to the values obtained by other groups.

CHAPTER 7

NUCLEAR MODELS AND LOW LYING STATES IN ^{112}Cd.

7.0 Introduction

A brief summary of some model predictions of monopole matrix elements is presented. These values are compared to the results obtained in this work.

7.1 The Vibrational Phonon Model

In the simple vibrational phonon model for undeformed spherical nuclei, collective excitation can be seen as small oscillations of the surface around the spherical equilibrium shape with the nuclear surface tension as restoring force. Only quadrupole ℓ =2 oscilations are considered since monopole ℓ = 0 oscillations represent compression vibrations which are contrary to the condition that the nuclear volume should be constant, and dipole oscillations ℓ = 1 have high excitation energies ~ 20 MeV and serve no purpose in explaining low-lying energy levels.

This approach leads to a Hamiltonian having the structure of an harmonic oscillator, giving rise to evenly spaced energy levels which differ in energy by $\hbar\omega$, the energy of the quantum of oscillation, the phonon. The no-phonon state is referred to as the vacuum, and can clearly only have angular momentum zero. The one-phonon state has angular momentum $j^{\pi} = 2^{+}$ and the two-phonon states are triply degenerate and can have angular momentum 0^{+}, 2^{+} and 4^{+} explaining the existance of a low lying 0^{+} state. In practice anharmonic forces lift the degeneracies. This model hence only is applicable when the splitting is small compared to $\hbar\omega$. ref. (Sha 74).

7.2 Rotation Vibration Models

For slightly deformed nuclei the rotation-vibration model provides a more general description and incorporates rotations and small amplitude vibrations around the equilibrium shape which is not spherical. In this approach the low lying levels can be grouped into rotational bands built onto different vibrational states. These bands are denoted by:

g (ground-state rotational band) with $j^\pi = 0^+, 2^+, 4^+, \ldots$
β (beta vibrational band) with $j^\pi = 0^+, 2^+, 4^+ \ldots$.
γ (gamma vibrational band) with $j^\pi = 2^+, 3^+, 4^+, \ldots$

(Lan 82)
The names beta and gamma are derived from the two deformation variables β and γ where β gives the nuclear deformation, and γ is the nuclear shape parameter. (Sha 74)

Generally β-vibrations are vibrations in which the nucleus oscillates and changes its deformation around a given equilibrium deformation, retaining axial symmetry, and γ-vibrations, are oscillations in which the nucleus changes from being non-axially symmetric, via an axially symmetric shape, to a non-axially symmetric shape, and back again.

Figure 59 (Sak 72) shows the relationship between the level structures in the phonon and rotational nuclear models. The features of the four lowest excited states of ^{112}Cd ($j^\pi = 2_1^+, 0_1^+, 2_2^+, 4_1^+$) are in qualitative agreement with the predictions of a spherical quadrupole vibrational model, but the occurence of additional $j^\pi = 0^+$ and 2^+ levels at the energy of the two phonon triplet perturbs the simple picture. In addition, if one assumes the vibrational model with spherical shape, the 0^+ state should be identified to the two-phonon state and $\rho(E0)$ for the transition to the zero phonon 0_g^+ state and $X(E0/E2)$ vanishes, which is experimentally disproved.

FIGURE 59

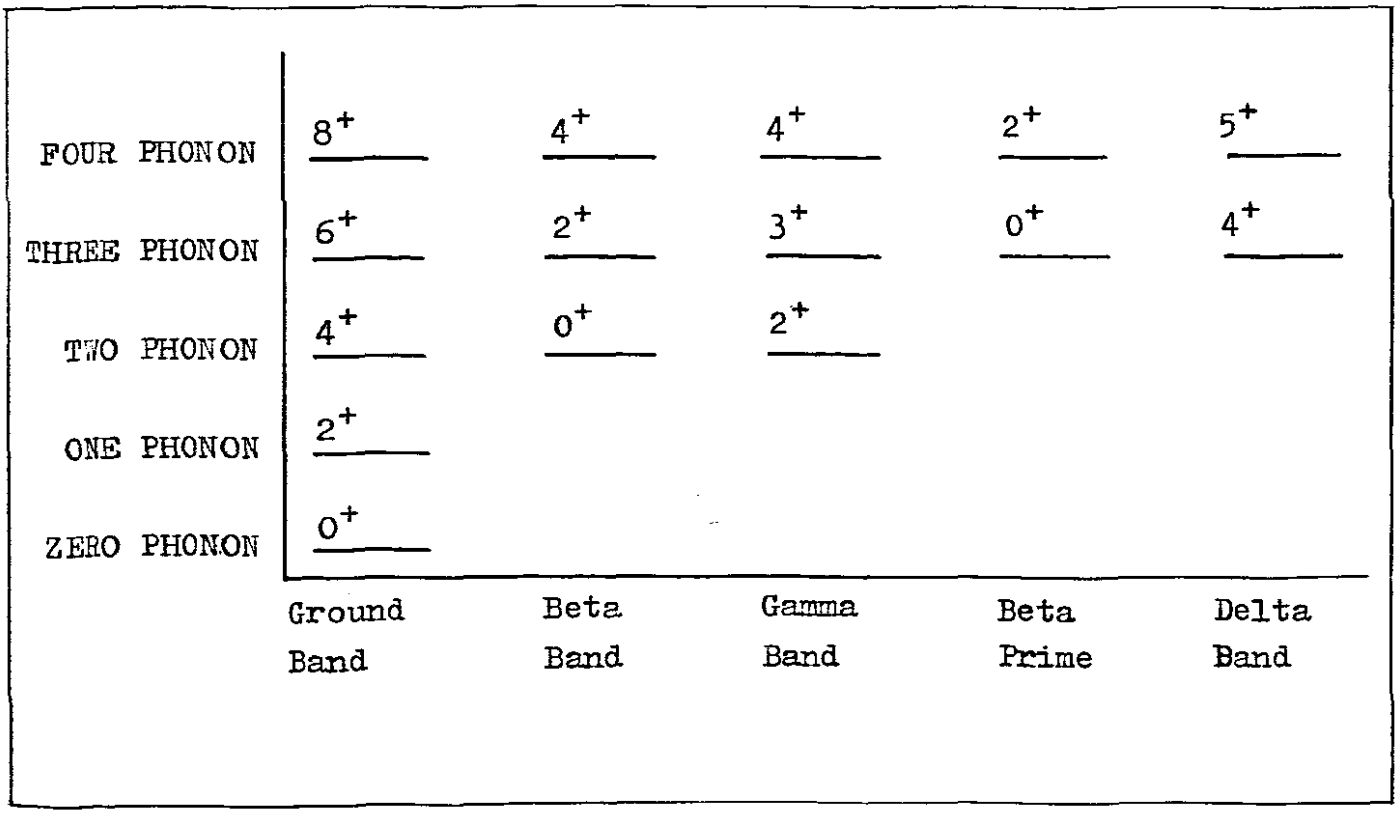

FIGURE 59: The relationship between the level structures in the phonon and rotational nuclear models.

Several attempts have recently been made to explain these features of ^{112}Cd. It was shown (Mey 77) (Ber 73) that the even Cd nuclei possess two minima in their surface potential energy. Hence two stable deformed shapes exist and the 0_2^+ and 2_2^+ states could form the head of an additional rotational band at approximately the two phonon energy.

Takada et al used a theory of mode coupling between the two phonon 0^+ mode and the pairing-vibrational mode to investigate the first excited 0_1^+ state of spherical nuclei like ^{112}Cd. Matrix elements for E0 transitions were also obtained for transitions from the 0_1^+ and 0_2^+ states. The energies of the 0_1^+ and 0_2^+ states are higher than the experimental value due to the fact that three phonon states were omitted from the mixing procedure. (^{112}Cd 0_1^+ = 1,9 MeV and 0_2^+ = 2,6 MeV) (Tak 83)

The E0 transition probability is strongly influenced by the mixing property, because the E0 transition from a pure two-phonon state to the zero-phonon ground state is completely forbidden, and only the pairing-vibrational state contributes to the E0 transition. The E0 matrix element is given by $\rho(E0) = \rho_p + \rho_n$ where ρ_p and ρ_n are the contributions from the proton and neutron pairing-vibrational components of the 0_1^+ state, respectively. A value of $\rho^2(E0) \sim 0{,}09$ is quoted. Using the same theory, values for the matrix elements $\rho(E0)$ for transitions from the 0_2^+ state to the 0_1^+ and 0_g^+ states can be obtained and are given in ref. (Tak 83.)

In a similar model Heyde et al (Hey 82) used particle-hole excitations across the Z = 50 proton closed shell in order to generate shell-model intruder states to explain the low lying energy levels in ^{112}Cd. The quintuplet of states near the two phonon level are explained as a mixture of the normal two-phonon excitation with 2p-2h excitations across the Z = 50 closed proton shell. The energy levels depend on the quadrupole phonon energy, the single particle and single hole energies, and the particle-core and hole-core coupling interactions. In these calculations evidence for a quintuplet of states near 1,5 MeV exists, as can be seen in figure 60.

FIGURE 60

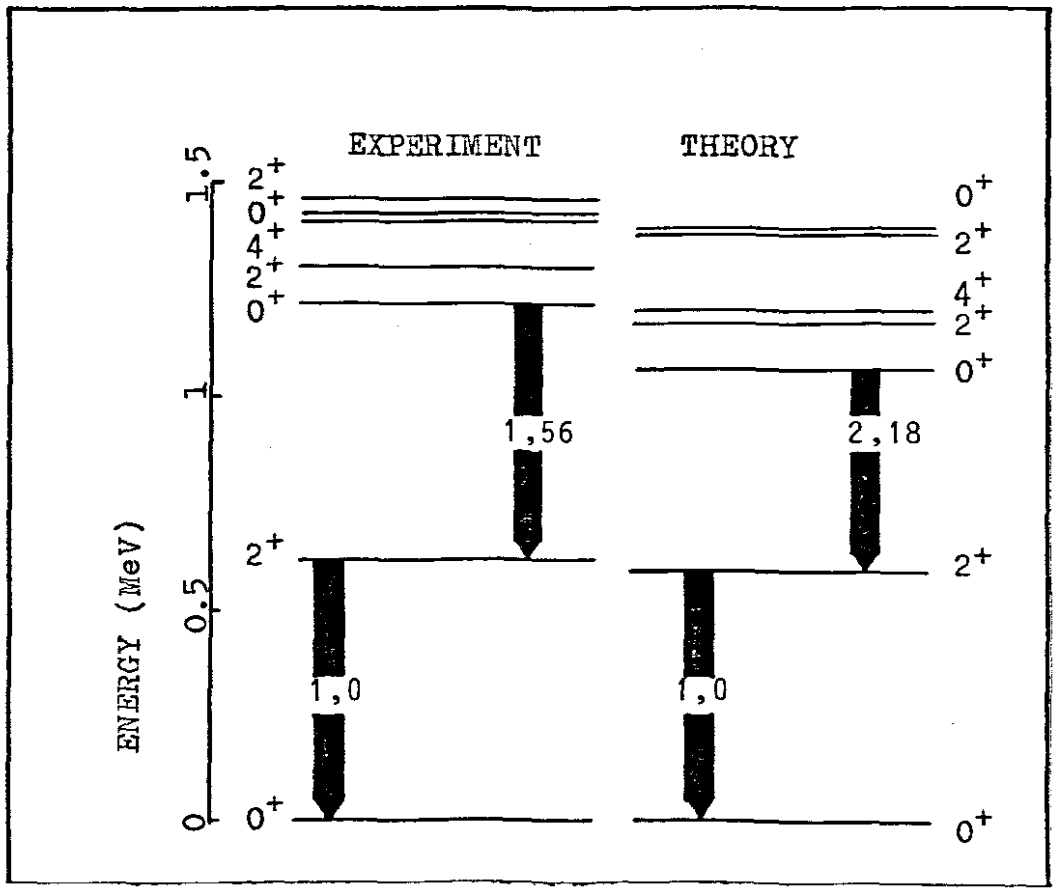

FIGURE 60: Comparison between theoretical (particle-hole model) and experimental energy levels.

Electromagnetic E2 and E0 decay properties can also be obtained using this theory. The B(E2) values are in good agreement with experiment (Hey 82). The theoretical values of ρ^2(E0) are somewhat higher than those of previous experimental data.

TABLE 13

$j_i^{\Pi} \rightarrow j_f^{\Pi}$	$\rho^2(E0) \times 10^3$ (Theory)
$0_1^+ \rightarrow 0_g^+$	77
$0_2^+ \rightarrow 0_g$	4,6
$0_2^+ \rightarrow 0_1^+$	1,1
$2_2^+ \rightarrow 2_1^+$	2
$2_3^+ \rightarrow 2_1^+$	26
$2_3^+ \rightarrow 2_2^+$	3

TABLE 13: Various values of $\rho^2(E0)$ for different transitions in ^{112}Cd. These are theoretical values as presented by ref. (Hey 82.)

7.3 ^{112}Cd and the Interacting Boson Model (IBM)

The IBM is an algebraic description of the properties of nuclei with several particles outside the closed shells. In its simplest form the interacting boson model assumes that the structure of low-lying levels of nuclei is dominated by excitations of the particles outside the major closed shells. Further more, it assumes that the important particle configurations in the low lying levels

of even-even nuclei, are those in which identical particles are paired together in states with total angular momentum L = 0 and L = 2. These pairs are treated as bosons. Proton (neutron) bosons with angular momentum L = 0 are denoted by s_π (s_ν), and proton (neutron) bosons with angular momentum L = 2 are denoted by d_π(d_ν). The number of proton bosons N_π, and the number of neutron bosons N_ν, are counted from the nearest closed shell, and if more than half the shell is full the numbers are taken to be the number of hole pairs. In the simplest form of the IBM, the even-even nucleus is treated as a system of $N = N_\pi + N_\nu$ bosons. (Ari 81). In general the IBM has been a fairly successful model in fitting energy levels as well as transitions probabilities.

A description of even Cadmium isotopes in terms of the simple IBM is given by Morrison and Smith (Mor 80). As stated previously the energies and decay properties of the four lowest excited states ($j_i = 2_1^+, 0_1^+, 2_2^+, 4_1^+$) of ^{112}Cd are known to agree qualitativly with the spherical quadrupole vibrational model. This model however fails to explain the presence of low lying intruder states ($j^\pi = 0_2^+$ and 2_1^+ levels) near the normal two phonon states, forming a quintuplet of states. (Hey 82). Using the IBM with particle-hole excitation across the Z = 50 proton shell, these intruder states can be generated and hence explain the features of the ^{112}Cd even-even nucleus. This quintuplet of states can be explained as a mixing of the normal quadrupole two-phonon excitation with 2p-2h excitations across the Z = 50 closed proton shell.

A neutron-proton (n - p) IBM calculation of the ^{112}Cd nucleus would imply $N_\pi = 1$ proton bosons and $N_\nu = 7$ neutron bosons. (Configuration A). In the presence of proton 2p - 2h excitations, however, two protons are excited across the closed Z = 50 shell. Therefore, three

FIGURE 61

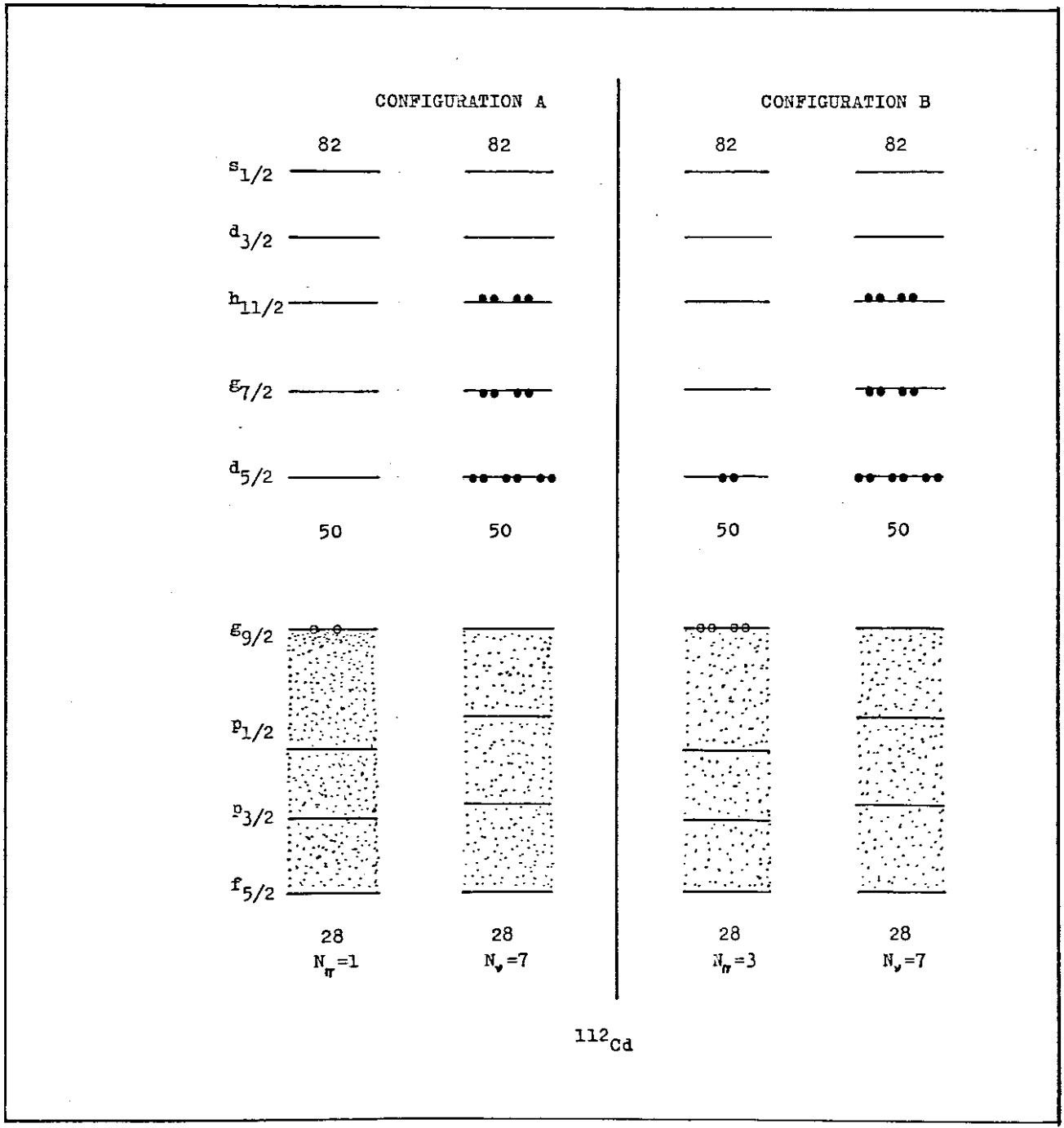

FIGURE 61: A schematic representation of the N_π=1 and the N_π=3 configuration in the n-p IBM configuration mixing calcultions, for ^{112}Cd. The distribution of particles over the available single particle orbitals and the ordering of the levels are drawn, and the major shells at Z = 28, 50, 82 and N = 28, 50, 82 are indicated. (Adapted from Heyde et al (Hey 82)).

active proton bosons can be associated with this particular type of configuration. (Configuration B) The two configurations are shown in fig. 61 (Hey 82).

The mixing of these two configurations is used to explain the nuclear structure as found experimentally. With this approach the presence of the intruder states can be explained. The extra 0^+ and 2^+ levels correspond to the lowest states of the excited configuration. (Sam 81). Energy levels of this model correspond well with experimental data.

FIGURE 62

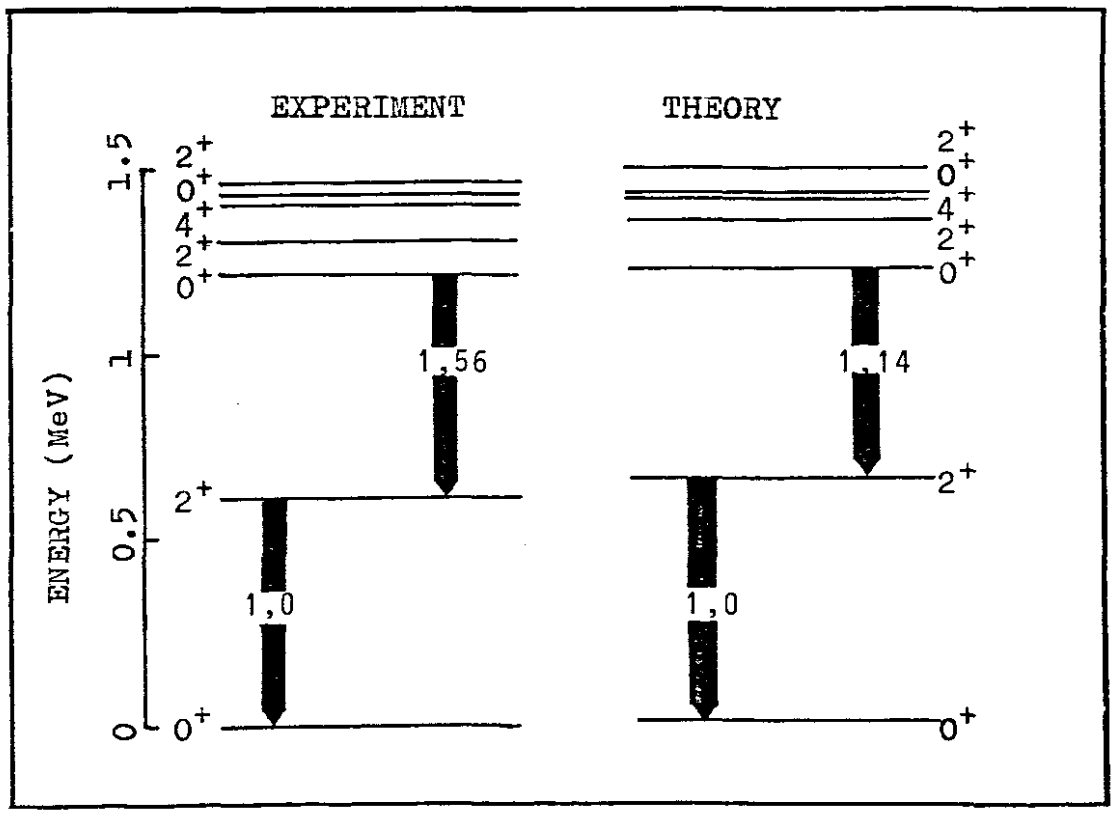

FIGURE 62: Comparison between theoretical (n-p IBM model) and experimental energy levels of ^{112}Cd. The relative B(E2) values are indicated. ref. (Hey 82, Sam 81).

In these calculations the energy for the two-particle two-hole proton excitation across the shell gap at Z = 50 to form the $N_\pi = 3$ configurations is calculated to be 5,45 MeV. Despite this high excitation energy (5,45 MeV) the ground state of this configuration can be seen to be about 1,3 MeV. This is due to much larger binding energy of this configuration (Sam 81). The B(E2) values are also in good agreement with experimental values (Fig. 62) In the IBM mixing calculations ρ(E0) values can also be calculated. However a number of parameters, comparable to the value of experimental ρ(E0) values, have to be used and hence no definite conclusions can be reached about the ρ(E0) values in the IBM approach. (Hey 82)

7.4 Model predictions and experimental results

In table 14 some well known model predictions of ρ^2(E0) and X(E0/E2) values for the transition $0_1^+ \rightarrow 0_g^+$, in ^{112}Cd are presented together with the experimental value, obtained in this work.

TABLE 14

ref	a	b	c	d	e	f	g	h	this work
$\rho^2 x10^3$	77	90	37	57	109				30(9)
$Xx10^3$			35	33	130	36	140	210	21(4)

TABLE 14: Theoretical values for ρ^2(E0) and X(E0/E2) for the $0_1^+ \rightarrow 0_g^+$ transition in ^{112}Cd, together with the experimental values obtained in this work. The references are:

a)	p-h excitation mixing model	Hey 82
b)	mode coupling theory	Tak 83
c)	naive spherical vibrator	Jul 80
d)	Reiner phonon model	Ohy 80
e)	Rasmussen vibrating spheroid	Ohy 80
f)	harmonic oscillator	Gia 79
g)	quasi-vibration model	Gia 79
h)	Daveytov model	Gia 79

From the tabulated values in table 14 it becomes clear that the predicted values of both ρ^2(E0) and X(E0/E2) are considerably higher than the experimentally obtained result which has been shown to agree with other experimental results. Therefore, however succesful the models might be in describing energy levels, gamma transition probabilities and other nuclear properties, none of the quoted models comes close to explaining the nuclear matrix elements.

CHAPTER 8

CONCLUSION

This experimental work has shown that the mini-orange spectrometer can be effectively applied for internal conversion electron spectroscopy. The results obtained for electric monopole matrix elements compared favourably with other results, and has once again indicated the need for a more satisfactory explanation of E0 transition probabilities in terms of nuclear model theory. Although most models provide satisfactory fits of energy levels, transition probabilities and especially E0 transition probabilities which are much more sensitive to the model used, are still poorly reproduced by these models. Systematic investigations of nuclear monopole matrix elements for groups of nuclei can definitely provide most valuable information towards the development of nuclear models.

Alb 69 D Alburger in α, β, γ ray spectroscopy Ed. K Siegbahn (North Holland 1968)

Ald 75 K Alder R M Steffen in The Electromagnetic Interaction in Nucleur Spectroscopy Ed. W D Hamilton (North Holland 75)

Ald 72 A. Aldushchenkov N A Voinova Nuclear Data Tables 11 1972

And 77 R E Anderson et al Nuclear Physics A281 1977

Ari 81 A Arima, F Iachello Annual Review Nuclear and Particle Science 31 1981

Ban 78 I M Band, M B Trazaskovskaya Atomic and Nuclear Data Tables 21 1978

Bel 70 D A Bell et al Canadian Journal of Physics 48 1970

Bel 82 F Bell et al Nuclear Instruments and Methods 194 1982

Ber 69 M J Berger et al Nuclear Instruments and Methods 69 1969

Ber 73 L von Bermus, U Schneider, N Greiner Lettere I1 Nuovo Cimento 6 nr 13 1973

Bel 53 E Bleuler et al Physical Review 90 no 3 464 1953

Bal 79 J M Blatt, V F Weisskopf Theoretical Nuclear Physics (Springer 1979)

Bor 64 L A Borisoglebskii Soviet Physics Uspekhi 6 nr 5 1964

Chu 55 E L Church, J Weneser Physics Review 100 1955

CWe 56 E L Church, J Weneser Physics Review 103 1956

Chu 56 E L Church, J Weneser Physics Review 104 nr 5 1956

Chu 58 E L Church, M E Rose, J Weneser Physics Review 109 1958

Chu 60 E L Church, J Weneser Annual Nuclear Science 10 1960

Dav 66 J P Davidson Nuclear Physics 86 1966

Dra 69 O Dragoun et al Nuclear Data Tables A6 1969

Dra 71 O Dragoun et al Nuclear Data Tables A9 1971

Dra 75 O Dragoun, V Brabev Atomic and Nuclear Data Tables 15 1975

Egi 70 T von Egidy Nuclear Data Tables A7 1970

Fau 83 H R Faust et al Nuclear Instruments and Methods 213 p271 1983

Fas 83 H R Faust et al Nuclear Instruments and Methods p277 1983

Fee 79 S J Feenstra PhD. Rijksuniversiteit Groningen 1979

Fuj 81 M Fujioka et al Zeitschrift für Physik A299 1981

Ger 58 T R Gerholm, B G Petterson Physics Review 110 1958

Gia 79 A Gianatiempo et al Zeitschrift für Physik A290 1979

Gia 82 A Gianatiempo, A Perego, P Sona Zeitschrift für Physik A306 1982

Gib 68 W M Gibson et al in α, β, γ ray Spectroscopy Vol. 1 Ed. K Siegbahn (North Holland 1968)

Gou 66 F S Goulding Nuclear Instruments and Methods 43 nr 1 1966

GPe 82 A Giannatiempo, A Perego, P Sona I1 Nuova Cimento 70 nr 1 1982

Gre 58 T A Green, M E Rose Physics Review 110 nr 1 1958

Gro 68 S R de Groot et al in α, β, γ ray Spectroscopy vol.2 Ed. K Siegbahn (North Holland 1968)

Hag 66 R S Hager, E C Seltzer in Internal Conversion Processes p309 Ed. W D Hamilton (Acad Press 1966)

Hag 68 R S Hager, E C Seltzer Nuclear Data Tables A4 Part 1 1968

Hag 69 R S Hager, E C Seltzer Nuclear Data Tables A6 Part III 1969

Ham 66 J H Hamilton Nuclear Data Tables A1 nr 6 1966

Ham 75 J H Hamilton in The Electromagnetic Interaction In Nuclear Spectroscopy Ed. W D Hamilton (North Holland 1975)

Has 66 S Hagström et al in Internal Conversion Processes Ed W D Hamilton (Acad Press 1966)

Hey 82 K Heyde, P van Isacker, M Woroquien, G Wenes, M Sambataro Physics Review 25 nr 6 1982

Hol 66 J M Hollander Nuclear Instruments and Methods 43 1966

HSe 66 R S Hager, E C Seltzer in Internal Conversion Processes p315 Ed. W D Hamilton (Acad Press 1966)

HSe 68 R S Hager, E C Seltzer Nuclear Data Tables A4 Part II 1968

Ish 71 M Ishii Nuclear Instruments and Methods 93 1971

Ish 75 M Ishii Nuclear Instruments and Methods 127 1971

Jha 66 J H Hamilton in Nuclear Spin and Parity Assignments Ed. N Gove, R Robinson (Acad Press 1966)

Jul		R Julin PhD University of Jyvaskyla Finland
Jul	80	R Julin et al Zeitschrift für Physik A296 1980
Kap	64	J van Klinken et al Nuclear Instruments and Methods 130 1975
Kli	72	J van Klinken, K Wisshak Nuclear Instruments and Methods 98 1972
Kli	75	J van Klinken et al Nuclear Instruments and Methods 130 1975
Kli	78	J van Klinken et al Nuclear Instruments and Methods 151 1978
Kra	73	K Krane, R M Steffen Nuclear Data Tables II 1973
Kra	75	K Krane Atomic and Nuclear Data Tables 16 1975
Kra	77	K Krane Atomic and Nuclear Data Tables 20 1977
Kri	73	D K Kripic Nuclear Data Tables 11 1973
Kum	75	K Kumar in The Electromagnetic Interaction In Nuclear Spectroscopy Ed. W D Hamilton (North Holland 1975)
Kuz	82	P G Kuzhir, G S Shulyakovskii. Izvestiya Akademii Nauk USSR 46 nr 1 1982
Lan	82	J Lange, K Kumar, J H Hamilton Review of Modern Physics 54 1982
Lom	66	R J Lombard in Internal Conversion Processes Ed. W D Hamilton (Acad Press 1966)
Mac	70	J A MacDonald, H D Sharma Nuclear Physics A156 1970
Mat	74	E der Mateosian, A W Sunyar Atomic and Nuclear Data Tables 13 1974
Mey	77	R Meyer, L Peker Zeitschrift für Physik A283 1977
Mor	76	H Morinaga, T Yamazaki In-beam Gamma-ray Spectroscopy (North Holland 1976)
Mor	80	I Morrison, R Smith Nuclear Physics A350 1980
Mos	68	S A Moszkowski in α, β, γ ray Spectroscopy Vol 2 Ed. K Siegbahn (North Holland 1968)
NDA	71	Nuclear Data Sheets 6 nr 1 71
NDS	72	Nuclear Data Sheets B71 1972
NDS	77	Nuclear Data Sheets 22 nr 1 77
NDS	80	Nuclear Data Sheets 29 nr 4 1980
NDS	81	Nuclear Data Sheets 33 nr 1 81
NDT	72	Nuclear Data Tables 11 nr 1, 2 1972

Neu 79 W Neuman Nuclear Instruments and Methods 164 1979

Ohy 72 S Ohya et al Nuclear Instruments and Methods 102 1972

Ohy 80 S Ohya et al Journal of the Physical Society of Japan 48 nr 4 1980

Pas 78 A Passajo et al Nuclear Instruments and Methods 157 1978

Pau 75 H C Pauli et al in The Electromagnetic Interaction in Nuclear Spectroscopy Ed. W D Hamilton (North Holland 1975)

Ros 35 M E Rose, E Uhlenbach Physics Review 48 1938

Ros 49 M E Rose, Physics Review 76 1949

Ros 68 M E Rose in α, β, γ ray Spectroscopy Vol 2 Ed. K Siegbahn (North Holland 1968)

Rös 78 F Rösel et al Atomic and Nuclear Data Tables 21 1978

Sak 72 M Sakai Nuclear Data Tables 10 1972

Sam 81 M Sambataro Nuclear Physics A380 1981

Sch 78 P Schlüter et al Zeitschrift für Physik A286 1978

Sch 79 P Schlüter, G Soff Atomic and Nuclear Data Tables 24 nr 6 1979

Sha 74 A de Schalit, H Feshbach Theoretical Nuclear Physics Vol. 1 (J Wiley 1974)

Sof 81 G Soff et al Zeitschrift für Phyzik A303 1981

Spo 84 B Spoelstra, E Rohwer A Mini-orange Spectrometer for Conversion Electron Studies. Univ. Zululand Series B no 35 1984

Ste 75 R M Steffen, K Adler in the Electromagnetic Interaction In Nuclear Spectroscopy Ed. W D Hamilton (North Holland 1975)

Tai 80 W H Tait Radiation Detection (Butterworths 1980)

Tak 83 K Takada Nuclear Physics A395 1983

Tho 40 R Thomas Physics Review 58 1940

Tru 72 V F Trusov Nuclear Data Tables 10 1972

Ven 61 T Venkova, W Andrejscheff Atomic and Nuclear Data Tables 26 1961

Voi 76 N A Voinova International Nuclear Data Committee Report INDC (CCP-93/N) 1976

Wal 68 M Waldschmidt, S Wittig Nuclear Instruments and Methods Vol 64 1968

Wal 72 G Wallace, G J McCullum, N G Chapman Nuclear Physics A182 1972

War 65 E K Warburton et al in Nuclear Spin and Parity Assignments Ed. N Gove, R Robinson (Acad Press 1965)

Wes 83 L Westerberg Tandem Accelerator Laboratory Uppsala (Private Communication 1983)

Wil 60 D H Wilkenson in Nuclear Spectroscopy Part B Ed. F Ajzenberg-Selowe (Acad Press 1960)

Wil 68 R Wilson in α, β, γ ray Spectroscopy Vol 2 Ed. K Siegbahn (North Holland 1968)

Wil 69 D H Wilkenson Nuclear Physics A133 1969

Wil 70 D H Wilkenson Nuclear Instruments and Methods 82 1970

Yaf 62 L Yaffe Annual Review of Nuclear Science nr 12 1962

Yam 67 T Yamazaki Nuclear Data Tables A3 nr 1 1967